This electronic thesis or dissertation has been downloaded from the King’s Research Portal at https://kclpure.kcl.ac.uk/portal/

Exotic compact objects in numerical relativity

Helfer, Thomas

Awarding institution:
King's College London

The copyright of this thesis rests with the author and no quotation from it or information derived from it may be published without proper acknowledgement.

END USER LICENCE AGREEMENT

Unless another licence is stated on the immediately following page this work is licensed under a Creative Commons Attribution-NonCommercial-NoDerivatives 4.0 International licence. https://creativecommons.org/licenses/by-nc-nd/4.0/

You are free to copy, distribute and transmit the work

Under the following conditions:

- Attribution: You must attribute the work in the manner specified by the author (but not in any way that suggests that they endorse you or your use of the work).
- Non Commercial: You may not use this work for commercial purposes.
- No Derivative Works - You may not alter, transform, or build upon this work.

Any of these conditions can be waived if you receive permission from the author. Your fair dealings and other rights are in no way affected by the above.

Take down policy

If you believe that this document breaches copyright please contact librarypure@kcl.ac.uk providing details, and we will remove access to the work immediately and investigate your claim.

Download date: 09. Jan. 2025

Exotic Compact Objects in Numerical Relativity

Thomas Helfer

Department of Physics
King's College London

This dissertation is submitted for the degree of
Doctor of Philosophy

June 2020

Acknowledgements

I would like to thank Eugene Lim, whose kindness, support and guidance made this journey a fantastic experience.

I would also like to thank the GRChombo team (http://www.grchombo.org/) and the COSMOS team at DAMTP, Cambridge University for their ongoing technical support. I am indebted especially to Katy, who patiently shared her knowledge of GRChombo with me. To Josu and James which were fantastic to work with. Special thanks to Robin, Miren, Amelia, Alex, Jessica, Helvi, Eugene, Katy, Josu for their very useful feedback.

I am very grateful to my family and their understanding and infinite support that was crucial on to be able to complete this journey and especially to my fantastic parents Wolfgang and Barbara who not only have been wonderful parents but also mentors.

Apologies to the TPPC department for the acoustic pollution caused. To all my friends (James, Matt, Giuseppe, Josu, Alex, Ali, Katharina, Stephanie, Jonas, Lena, Miguel, Lary, Yurema, Sree) who helped me to keep my mental health while writing this thesis, and special thanks to the wonderful Jessica.

For the work done in chapter 2, I would like to thank David J.E. Marsh and Malcolm Fairbairn for their help to complete this work. We also would like to thank Ricardo Becerril for the use of his initial condition code for Oscillotons. We acknowledge useful conversations with Simon Rozier, Avery Broderick, Vitor Cardoso, Francisco Guzman, Tommi Markkanen, Joseph Silk, Rohana Wijewardhana, and Luis Urena-Lopez. Numerical simulations were performed on the COSMOS supercomputer, part of the DiRAC HPC, a facility which is funded by STFC and BIS. This work also used the ARCHER UK National Supercomputing Service (http://www.archer.ac.uk) for some simulations.

I am grateful for the work of James Y. Widdicombe in chapter 3, who did most of the hard work. I also acknowledge useful conversations with Mustafa Amin, Malcolm Fairbairn, Matthew McCullough, Jens Niemeyer and Helvi Witek. Numerical simulations were performed on the COSMOS supercomputer, funded by DIRAC/BIS and on BSC Marenostrum IV via PRACE grant Tier-0 PPFPWG, by the Supercomputing Centre of Galicia

and La Palma Astrophysics Centre via BSC/RES grants AECT-2017-2-0011 and AECT-2017-3-0009 and on SurfSara Cartesius under Tier-1 PRACE grant DECI-14 14DECI0017.

In chapter 4, I am thankful for the help of our collaborators Mustafa Amin and Marcos A.G. Garcia. I acknowledge useful conversations with Katy Clough, Vitor Cardoso, James Widdicombe, William East, Scott Hughes and Matt Johnson. Numerical simulations were performed on the COSMOS supercomputer, funded by DIRAC/BIS, on BSC Marenostrum IV via PRACE grant Tier-0 PPFPWG, by the Supercomputing Centre of Galicia and La Palma Astrophysics Centre via BSC/RES grants AECT-2017-2-0011 and AECT-2017-3-0009 and on SurfSara Cartesius under Tier-1 PRACE grant FI-2017-1-0042.

Regarding the work done in chapter 5, I acknowledge useful conversations with José Juan Blanco-Pillado, Katy Clough, Ed Copeland, William East, Mark Hindmarsh, Paul Shellard, James Widdicombe and Helvi Witek. Special thanks to Federica Albertini, Gregorio Carullo and Alastair Wickens. Numerical simulations were performed on the COSMOS supercomputer and the Cambridge CSD3 HPC, funded by DIRAC3/BIS, on BSC Marenostrum IV via PRACE grant Tier-0 PPFPWG, by the Supercomputing Centre of Galicia and La Palma Astrophysics Centre via BSC/RES grants AECT-2017-2-0011 and AECT-2017-3-0009 and on SurfSara Cartesius under Tier-1 PRACE grant DECI-14 14DECI0017.

Some simulation results were analyzed using the visualization toolkit YT [1]. Matplotlib [2] was used to generate the plots seen throughout the paper, and Numpy [3] was used for the statistical analysis.

Abstract

Einstein's equations of General Relativity were first published in 1915 and are until this day the most accurate understanding of gravity. Although first attempts at using computers to solve them were made in the 1960s [4], only recently has Numerical Relativity (NR) produced mature tools. These new tools came to existence not only due to the recent development of robust numerical techniques but also due to the exponential growth of computational power. A crucial event for NR was the first measurement of two Black holes inspiraling and merging by the LIGO/Virgo collaboration [5] for which numerical simulations played a significant role. This was a technically challenging system to model that required numerical simulations [6–8], and to date, NR is the only tool that can accurately solve it.

In this thesis, we study compact objects using Numerical Relativity. In particular, we use NR to investigate the nature and the different possible ways of detecting two strongly gravitating objects: cosmic strings and Boson stars. A better understanding of these objects is essential as they might produce gravitational waves that allow them to be measured by current and future gravitational wave detectors.

An introduction to the different types of Boson stars, with different field-content, different charge or rotating stars, and an overview of the current literature regarding the challenges of measuring and modelling Boson stars is provided on chapter 1. A small introduction to cosmic strings is provided in chapter 5.

Chapter 2 focus on one type of Boson stars, which are made from a single real scalar (i.e. oscillatons) and investigate how changing the potential to the one of an axion can affect its stability. Changing the potential is essential to elucidate if Bosonic stars might be made from dark matter. Our results show that under certain condition the star can collapse into a Black hole or disperse completely.

We study the formation of oscillatons in chapter 3, we simulate sinusoidal initial data and determine whether they collapse to stars. We find that depending on the mass of the perturbation, we can either form Black holes or stable Boson stars. We use this information to create a population of Black holes and Axion stars, binaries of which could be potentially detected by LIGO/Virgo detectors.

Chapter 4 explores oscillatons head-on merger. The end product of such mergers can be either a stable, but very perturbed oscillaton or a Black hole. We find that in both cases, the signal is different from a Black hole merger, even if cases where the final result was a Black hole, thus making them a potentially easily differentiable source.

On the other hand, in chapter 5, we study the physics and the gravitational waves produced by Abelian-Higgs cosmic strings. These strings are topological defects that might have formed in the very early universe and can be visualised as long filaments, which move similarly to long rubber bands in zero gravity. Interestingly, they were already predicted by grand unified theories (GUTs), which unifies weak, strong, electromagnetic and gravitational forces. As shown by [9], due to their motion, they might produce gravitational waves, we discuss these findings in this chapter, simulate a collapsing string and extract the gravitational waves emitted by it.

Many new gravitation wave detectors are in the pipeline to be finished in the next few decades. These new detectors will drastically change our ability to probe the universe, allowing us to state more complex questions, and certainly lead to new discoveries of the wonders of our universe. I hope that in this thesis, I set out the path to allow the discovery of two such objects, cosmic strings and oscillatons. There is further work to be done, not only improving on the simulations of oscillatons or cosmic strings but also further developing theories that can then be tested using these future detectors.

Table of contents

List of figures **xi**

List of tables **xxiii**

1 Introduction **3**

1.1 Taxonomy of Boson stars in General Relativity 3

1.1.1 Constructing U(1) Scalar stars 4

1.1.2 Rotating Boson stars 18

1.2 Detecting Boson stars 21

1.2.1 Gravitational Waves from Binaries with Boson stars 21

1.3 Boson stars as Supermassive Black holes 25

2 Black hole formation from Axion stars **29**

2.1 Introduction 30

2.2 Simulating Axion Stars 32

2.2.1 The axion potential 33

2.2.2 Perturbative Analysis of Axion Stars Solutions 35

2.2.3 Initial Conditions 38

2.2.4 Three phases of Axion stars 39

2.2.5 “Scalar Wigs” 43

2.3 Observational Consequences 44

2.3.1 BH – Axion star mass relation 44

2.3.2 Axion stars as seeds of SMBHs? 45

2.3.3 BHs from axion miniclusters? 46

2.3.4 Quantum Effects and Axion Emission 46

2.4 Conclusions 47

3 Formation of Relativistic Axion Stars 55

3.1 Introduction . . . 55
3.2 Gravitational Waves from ECOs . . . 56
3.3 Axion Star Formation . . . 59
  3.3.1 Initial Conditions . . . 59
  3.3.2 Numerical Simulations . . . 62
  3.3.3 Axion Star Formation and Evolution . . . 64
  3.3.4 Black hole Formation . . . 65
  3.3.5 Dispersion Regime . . . 65
3.4 Axion Stars and Gravitational Waves . . . 65
  3.4.1 Cosmological Formation of Axion Stars . . . 68
  3.4.2 Peak Statistics . . . 69
3.5 Discussion . . . 70

4 Gravitational Wave Emission from Collisions of Compact Scalar Solitons 75

4.1 Introduction and Results . . . 76
4.2 Initial Set-Up of Solitons . . . 77
4.3 Gravitational Waves from Collisions . . . 79
  4.3.1 Subcritical Case $\mathcal{C} \lesssim 0.04$ . . . 79
  4.3.2 Critical Case $0.04 \lesssim \mathcal{C} \lesssim 0.14$ . . . 80
  4.3.3 Degenerate Case $\mathcal{C} > 0.14$ . . . 81
4.4 Discussion and Future Directions . . . 81

5 Cosmic String Loop Collapse in Full General Relativity 85

5.1 Introduction . . . 85
5.2 Abelian Higgs with Gravity . . . 87
5.3 Results . . . 88
5.4 Gravitational Waves from Black hole formation . . . 90
5.5 Discussion and detection prospects . . . 92

6 Conclusions 95

6.1 Summary . . . 95
6.2 Future work . . . 96

References 97

Appendix A Black hole formation from Axion stars 111
- A.1 Notes on Axions 111
  - A.1.1 Non-relativistic Axion stars and oscillotons 111
  - A.1.2 Relativistic Axion stars and oscillotons 112
  - A.1.3 Cosmological initial conditions and symmetry breaking 114
- A.2 GRChombo 116
  - A.2.1 Numerical implementation 116
  - A.2.2 Gauge choice 118
  - A.2.3 Evolution equations 118
- A.3 Specific Numerical Details 120
  - A.3.1 Initial Conditions, Convergence and Stability 120
  - A.3.2 Complex PQ field versus real axion field 124

Appendix B Formation of Relativistic Axion Stars 129
- B.1 Two Pass Connected Component Labelling 129
  - B.1.1 Constructing Initial data 130
  - B.1.2 AMR Condition 131
  - B.1.3 Convergence and Stability 134
  - B.1.4 Axion Star Location 135

Appendix C Gravitational Wave Emission from Collisions of Compact Scalar Solitons 137
- C.1 Numerical Methodology 137
  - C.1.1 Constructing Initial Data 137
  - C.1.2 Numerical Methodology and Convergence Tests 141
- C.2 Self-Interactions 143

Appendix D Cosmic String Loop Collapse in Full General Relativity 145
- D.1 Numerical Methodology 145
  - D.1.1 Evolution Equations 145
  - D.1.2 Initial Data 149
  - D.1.3 Numerical Extraction of Signal 150
  - D.1.4 Numerics and Convergence Tests 152
- D.2 Abelian Higgs Code Test 153
- D.3 Comparison with Nambu-Goto 155

List of figures

1.1 **Mass for self-interacting potential :** Where $\sigma_c = (4\pi)^{1/2}\phi_0$ with several different values for the rescaled self-interaction $\Lambda = \lambda M_{\text{Pl}}^2/(4\pi m^2) = 0, 1, 30, 100, 200, 300$ for the potential $V(\phi) = m^2|\phi|^2 + \frac{1}{2}\lambda|\phi|^4$. The maximum mass and radius increases with larger attractive self-interactions. Figure from [10]. 7

1.2 **Charged Boson star solutions :** The mass and size becomes larger with increasing charge. However, there is a maximum charge $e_{crit} = 0.707$ for which the electromagnetic repulsion overpowers gravity. The addional line shows where the maxima are located. Figure from [11]. 12

1.3 **Proca Star Solutions Space :** Both the Noether charge Q and ADM mass against the frequency ω of the Proca star. Similar to Boson stars, points on the left to the maximum are unstable. Figure from [12]. 14

1.4 **Oscillatons Solutions :** The solutions for all modes $\hat{\phi}_j(r)$, $\hat{C}_j(r)$, $\hat{A}_j(r)$ of a maximally massive oscilloton ($\phi_0(0) = 0.46$) and with $r_{max} = 23.2\ m^{-1}$. We find that approximately every higher mode is suppressed by one order of magnitude, thus showing very fast convergence in j. Asymtotically in r, the solutions converge to the Schwarzschild spacetime, where we match with $M = 0.605\ \text{M}_{pl}^2/m$, the measured ADM mass. 16

1.5 **Overview of $m^2\phi^2$ Oscillatons :** The figure on the left shows the defining parameter $\hat{\phi}_0$ vs the ADM mass M_{ADM} of the soliton. We can see that the most stable solution can reach a maximum mass of $M = 0.605 M_{\text{Pl}}^2/m$. The right plot depicts $\hat{\phi}_0(0)$ against the compactness $\mathcal{C}$. We see that we can reach a maximum stable compactness of $\mathcal{C} \sim 0.14$ 17

1.6 **Illustration of Rotating Boson star:** Energy isosurfaces for a scalar configuration with $k = 2$. Figure from [13]. 19

1.7 **Solutions of rotational mini-boson stars** with rotating quantum numbers $k = 1,..,4$. Solutions left of the marked points are unstable due to the appearance of ergoregions. Figure from [13]. 20

1.8 **Tidal deformability [14] :** Tidal deformations for massive self-interacting Boson stars. A large lower bound of $\Lambda \geq 280$ allows the distiction between Boson stars and other compact object (i.e. Neutron stars or Black holes). . 22

1.9 **Comparison between Kerr BH and Boson star :** Simulated raytraced pictures at 230 GHz from electron synchrotron emission of the accrection disc which was obtained by GRMHD simulations. Comparison between the picture of a spinning kerr Black hole and a non-spinning mini-boson star [15]. 27

2.1 **The Axion star stability diagram**. The stability diagram is parameterized by the axion decay constant, f_a, and the initial condition M_{ADM} (which we set using the initial field velocity, Π, at the centre). Solid lines mark the approximate boundaries between three regions of the Axion star parameter space: quasi-stability (R1), collapse to a BH (R2), and dispersal (R3). We postulate the existence of a "triple point" between these regions. The dashed line marks the region below which axion mass is effectively negligible. Simulated Axion stars are marked as circles; other symbols mark points explored in more detail in Section 2.2. Below the triple point, for $f_a \ll M_{pl}$, under an increase in mass, dispersal of the star via winding of the axion field occurs before collapse to a BH. Above the triple point, stable Axion stars can collapse to BHs by acquiring mass e.g. by accretion. 30

2.2 **Initial Conditions.** We show our initial conditions, where ϕ is zero everywhere and the conjugate momentum of the field Π contains all the information about the solution. This solution for Π is correct for any value of f_a in the full cosine potential, since $V(\phi = 0) = 0$ for all f_a and the Hamiltonian constraint is satisfied. Therefore, we can use these $\Pi(t_i)$ profiles, which we parameterize according to their ADM mass using Fig. A.1, to define our one-parameter family of initial conditions for Axion stars. The ADM mass is measured in units of M_{pl}^2/m_a. 39

2.3 **Stable Axion stars.** $(M_{\rm ADM}, f_a) = (2.86, 0.92)$, R1 star in Fig. 2.1. *Left panel*: The evolution of the central field value, $\phi(r=0)$, over time of a stable Axion star, compared to that of an oscillaton (i.e. pure $m_a^2\phi^2$). Stability is shown over many periods of oscillation. The existence of two frequencies in this solution can be understood qualitatively from the perturbative analysis in Section 2.2.2. *Right panel*: comparison of the potential for an $m_a^2\phi^2$ oscillaton (dashed) and the cosine Axion star (solid). The two marked points correspond to times in the evolution of the Axion star shown in the left panel. 40

2.4 **Black hole formation near the triple point.** $(M_{\rm ADM}, f_a) = (2.51, 0.35)$, R2 square in Fig. 2.1. The central field value is shown evolving over time in the top left panel, with the color gradient on the line used to indicate times in the other panels. The top right panel shows the radial profile of the lapse, α, on different time slices. In the bottom panel, several points are marked to show the movement of the central field value on the potential. Over time, the field amplitude slowly grows and leaves the $m^2\phi^2$ regime, even though initially it provides a good approximation to the axion potential. Shortly after the field goes over the "potential hill", the Axion star collapses to form a BH. BH formation is indicated by the value of α at the centre approaching zero. The yellow bar indicates the position of the apparent horizon shortly after it forms. Note that local proper time τ is used rather than simulation time t, to remove gauge effects due to the strongly varying lapse. 49

2.5 **Black hole formation near the dispersal region.** $(M_{\rm ADM}, f_a) = (2.63, 0.055)$, R2 star in Fig. 2.1. The parameter shown is the conformal factor of the metric, χ (for a definition see Appendix A.3). The first panel shows the initial data, and subsequent panels show the evolution. The initial state is spatially extended, with low curvature. As collapse proceeds, the Axion star becomes smaller, and some scalar radiation is emitted in waves. The final BH has an apparent horizon that is very small compared to the initial Axion star size. Some of the axion field remains outside the BH, and gravitationally bound to it, which we discuss in Section 2.2.5. 50

2.6 **Dispersion of Axion stars.** $(M_{\text{ADM}}, f_a) = (2.40, 0.14)$, R3 star in Fig. 2.1. The parameter shown is the conformal factor of the metric, χ (for a definition and relation to the Newtonian potential see Appendix A.3). Note that the colour scale for the conformal factor, χ is not the same as in Fig. 2.5, since in the dispersing case the variation in χ is much smaller, corresponding to less spatial curvature. The first panel shows the initial data. The second shows some initial collapse. Collapse then slows, which can be seen by the central peak getting broader and smaller in amplitude from the third to the fourth panel. As the dispersal continues, we notice matter shells being ejected. The evolution of $\chi(0)$ over a longer time scale is shown in Fig. 2.7. 51

2.7 **Dispersion of Axion stars.** $(M_{\text{ADM}}, f_a) = (2.40, 0.14)$, R3 star in Fig. 2.1. The parameter shown is the conformal factor of the metric, χ, which can be related to the Newtonian Potential in the weak gravity case (for a definition see Appendix A.3). Several points are marked to show the movement of the field on the field potential. The field quickly leaves the stable Axion star regime and the amplitude grows. Eventually the field goes "over the top" in the cosine potential: equivalent to the field winding in the complex plane. The amplitude then slowly decays by ejecting matter shells (see panel 4 of Fig. 2.6). The interplay between gradient energy and nonlinear interaction causes a very intricate evolution. 52

2.8 **"Scalar wig".** $(M_{\text{ADM}}, f_a) = (2.63, 0.055)$, R2 star in Fig. 2.1. Evolution of the scalar field outside the horizon, beginning at the point in time when the apparent horizon appears. The scalar field seems to fall slowly into the black hole, however, the configuration seems to be long-lived, i.e. stable for many oscillations. 53

3.1 **LIGO frequency band for Axion stars.** The frequency is given by the ISCO frequency, Eq. (3.6). The compactness $\mathcal{C}(M)$ is for non-interacting oscillatons, which is a good description of stable Axion stars. Assigning a luminosity distance to binaries, the minimum compactness is found from the results of Ref. [16]. Axion stars detectable by LIGO must have $\mathcal{C} \gtrsim 0.02$ and axion mass $m_a \approx 10^{-10}$ eV. 57

3.2 Using 3.10 we calculate the total box mass, M, of our initial conditions for a box size of $\tilde{L} = 16 m_a^{-1}$ and $f_a = 0.5 M_{pl}$, as well as the contributions to M of the gradient term, $\frac{1}{2}(\partial_i \phi)^2$, and the potential term, $V(\phi)$. For the f_a simulated it can be seen that our initial mass is dominated by contributions from the potential term. 60

3.3 **These plots are a summary of all numerical simulations performed**. Black circles indicate that blackholes where formed from the initial conditions and yellow circles indicate that Axion stars were formed. We emphasise that the y-axis labels the *initial total mass* of the simulation initial conditions, not the final mass of the formed objects. No dispersion cases were obtained, and the reason for this is outlined in 3.3.5. The results presented here mirror that of [17, 18], so when discussing the likely structure formation we will use the “phase diagram" constructed there. 63

3.4 **Evolution of the mass-radius relation of all simulations whose end state was identified as an Axion star.** The reference line in the plots is the mass radius relation for an unexcited Axion star, and the points on top indicate the evolution of the observed star forming. The evolution in time of the mass-radius relation is indicated by the colour of the point, with the darkest points being the earliest in the evolution and the lightest points being the end of the evolution. Additionally the start point of the evolution is indicated by an ‘S’. The mass radius relation fluctuates significantly over time, varying in a decaying way around the unexcited star value. This process is attributed to the formed stars having radial perturbative modes. Outliers on these graphs are due to the Axion star finder, outlined in B.1.4 66

3.5 **Variation of the Axion star radius over time for spherically symmetric initial data [17, 19]** . For $f_a = 5.0 M_{pl}$ the radial variation is negligible for both masses shown. When lowering f_a to $0.5 M_{pl}$ it can be seen that the more massive Axion star collapses to a blackhole, however for the less massive Axion star a radial variation with a period of $300 m_a^{-1}$ develops. The radial variation shown here has a longer period compared to the most massive case for $\tilde{L} = 16$, and shorter compared to $\tilde{L} = 64$. 67

3.6 **A toy model realisation of the axion density field** that can be filtered to locate candidate compact Axion stars. 69

3.7 Top panel: Peaks of the toy model density field are assigned masses as Axion stars and Black holes according to the location on the phase diagram with $f_a = 0.5\ M_{pl}$. Bottom panel: Using Eq. 3.6 and the $\mathcal{C}(M)$ relation for Axion stars, we calculate the gravitational wave frequencies for Axion star and BH equal mass binary mergers. 71

3.8 Peaks of the toy model density as Fig. 3.7 with $f_a = 0.5\ M_{pl}$ (upper panel) and $f_a = 0.1\ M_{pl}$ (lower panel). Note that as f_a dips below the triple point [17], a dispersal gap appears between the formation of Black holes and Axion stars. 72

4.1 Fraction of initial rest mass energy of the two oscillatons (E_{tot}) radiated into gravitational waves (E_{gw}) as a function of the initial compactness ($\mathcal{C}$) of each oscillaton. In the subcritical case, oscillatons collide to form a new stable but aspherical, excited oscillaton. In the critical regime, oscillatons collide to yield a black-hole after/during the collision. In the degenerate case, individual oscillatons collapse to black-holes before the collision. Note that in the critical regime (and possibly in the subcritical regime also), the emitted fraction in gravitational waves can exceed that of corresponding mass black-holes (0.06% dashed line). 77

4.2 **Relationship between the mass M and the compactness $\mathcal{C}$ of the oscillaton**. Note that for $\mathcal{C} \gtrsim 0.14$ ($M \approx 0.605 M_{\text{Pl}}^2/m$) oscillatons become unstable under perturbations (grayed area). 78

4.3 **The panel shows the numerically evaluated gravitational wave waveforms** (the dominant quadrupole mode: $l = 2$, $m = 0$ is shown) for typical subcritical ($\mathcal{C} = 0.03$), critical ($\mathcal{C} = 0.10$) and degenerate ($\mathcal{C} = 0.15$) collisions. For comparison, the waveform for the corresponding mass black-hole collision is also shown in black. Note that in the sub-critical case (left panel), the resulting excited oscillaton continues to emit gravitational waves. In the critical case (middle panel), the waveform is qualitatively similar to a BH-BH merger, but importantly, the post-merger QNM amplitude is greater for the oscillaton merger as they are less "rigid". Since there is some mass loss during the merger, the final mass is less than that of the equivalent BH-BH merger, leading to a slightly shorter QNM period (as observed). Finally, the degenerate case is almost indistinguishable from a BH-BH collision (right panel). The vertical dashed line indicates time of BH formation during the merger in the critical case, and pre-merger in the degenerate case. Note that $r\Psi_4 \sim r\ddot{h}$, and $t = 0$ is associated with the time when the objects are $\approx 60m^{-1}$ apart. Movie links for the time evolution of the gravitational wave signal and the energy density ρ are available for the subcritical, critical and degenerate mergers [20–22]. 79

4.4 **Numerically evaluated gravitational wave waveform for a typical subcritical ($\mathcal{C} = 0.03$) collision**, demonstrating bursts of repeating gravitational waveforms. Inset shows the "$+$" pattern of oscillations of the density of the perturbed final state. 82

5.1 **GW for a BH formed from circular cosmic string loop collapse:** We plot the real part of the dominant $l = 2$ $m = 0$ mode of $r\Psi_4$ over time. The loop has tension $G\mu = 1.6 \times 10^{-2}$ and an initial radius $R = 100\, M_{\rm Pl}^{-1}$. The grey shaded area of the plot are mixed with stray GWs that arise as artifacts of the initial data. The x-axis $t_{\rm ret} = t - r_{\rm ext}$ is the retarded time where $r_{\rm ext}$ is the extraction radius. 87

5.2 **Overview of simulations :** The loop can either form a BH or unwind and radiate all its mass. The analytical expression derived from the hoop conjecture accurately predicts the outcome. Movie links for the evolution over time of the collapse are available for the dispersion [23] and Black hole [24] cases. 89

5.3 **Critical collapse**: We plot the logarithm of the mass of the Black hole vs the logarithm of the difference between the initial and the theoretical(star)/observed(cross) critical radius for $G\mu = 1.6 \times 10^{-2}$. As we argued in the text, our simulation showed that the actual $R_*^{\rm ob} > R_*^{\rm th}$, resulting in a critical index within $0.17 < \gamma < 0.39$, where the error is due to the uncertainty in determining numerically $R_*^{\rm th} < R_* < R_*^{\rm ob}$. Note that we only use the first 7 points to compute the critical index for $R \leq 0.05 R_*$ as the critical relation is only expected to hold perturbatively. 91

A.1 **Criticality of oscillotons.** We show the oscilloton ADM mass, $M_{\rm ADM}$, versus $\phi_{1,m}(0)$, the value of the first component in the Fourier expansion of the field profile at the centre. There is a critical value $\phi_{1,m} = 0.48 M_{pl}$ where the mass relation turns over, and oscillotons become unstable. This defines $M_{\rm crit.,osc.}$, the oscilloton critical mass. Blue points show the oscilloton initial conditions used to map the $M_{\rm ADM}(\phi_1)$ relationship. Green points show those values of $M_{\rm ADM}$ for which we actually simulate dynamical Axion stars. As we show above, Axion stars show non-trivial behaviour and collapse for $M_{\rm ADM} < M_{\rm crit.,osc.}$. 115

A.2 **FMR Covergence test.** We tested the convergence of the code in an FMR setup, in three runs with finest mesh spacings of $h_1 = 0.125$, $h_2 = 0.0625$ and $h_1 = 0.03125$. The results are shown in the figure, which demonstrates that the code has ≈ 3.5th order convergence. There is some loss of the expected 4th order, but this is partly due to interpolation errors when comparing solutions (since we use a cell centred grid, the cell centre at each additional refinement level is $\Delta x/2$ from that of the level below). 123

A.3 **Relative Hamiltonian constraint violation, L2 norm** $(M_{\rm ADM}, f_a) = (0.85, 0.25)$. The L2 norm $||f||_2 = \sqrt{\frac{1}{V}\int_V f^2 dV}$ of the relative Hamiltonian constraint violation (as defined in Eqn. (A.30)) for a case of Black hole formation. We excise the interior of the Black hole apparent horizon after it forms. Because the definition of the relative density does not make sense anymore after Black hole formation, we continue to use the value from shortly before the apparent horizon appears. We used a short relaxation routine for χ initially, in addition to the numerical solution, to improve the initial constraint violation. 124

A.4 **Relative Hamiltonian constraint violation for initial conditions, radial profile** $(M_{\mathrm{ADM}}, f_a) = (0.85, 0.25)$. Initial relative Hamiltonian constraint violation, as defined in Eqn. (A.30). The zero radius marks the center of Axion star. The momentum constraint is identically zero initially, since K_{ij} = 0 and $S^i = 0$, so no plot is provided for this. 125

A.5 **Absolute Momentum constraint violation.** $(M_{\mathrm{ADM}}, f_a) = (0.85, 0.25)$. The L2 norm ($||f||_2 = \sqrt{\frac{1}{V}\int_V f^2 dV}$) of the absolute momentum constraint violation for a case of Black hole formation. Even though the initial data is not time-symmetric ($\Pi \neq 0$), K_{ij} and S^i are zero everywhere, therefore the momentum-constraint is trivially satisfied initially. 126

A.6 **Apparent horizon and ADM mass versus time** Evolution of the $(M_{\mathrm{ADM}}, f_a) = (2.63, 0.055)$, R2 star in Fig. 2.1. Evolution of the Black hole apparent horizon mass and ADM mass over time. The blue shaded area indicates the potential error due to resolution when measuring the radius of the AH. The AH mass increases as more matter is accreted, as expected, and stabilises at a relatively constant value, indicating that it is not significantly affected at later times by reflections. The ADM mass remains relatively constant. The later perturbations are caused by scalar fields propagating through the boundary which we use to measure it. These may be in part due to reflections from the boundary, but appear to remain well bounded and do not grow. 127

A.7 **Radial field stability.**Time evolution of the full complex field for different values of λ_φ for $f_a = \sqrt{8\pi}\sqrt{2}$, for which the evolution is oscilloton like. The panel on the left shows the radial modes $|\varphi|$, and the one on the right shows the difference between complex and real field evolution. Values in the left panel of ± 100 % would indicate that the radial mode is unbounded, that is, that it can go "over the top" of the central point. However, it can be seen that its values are extremely well bounded, justifying the use of the real potential as equivalent to that of the full complex one. The plots cover one period of the angular oscillation, which contains multiple periods in the radial amplitude. 128

B.1 The plot shows the L^2 norm Eq. B.11 of the Hamiltonian constraint violation over time for a simulation that forms an Axion star, with an initial total mass of $M = 1.34\, M_\odot\, 10^{-10}\mathrm{eV}\; m_a^{-1}$, $f_a = 5.0\, M_{pl}$ and $\tilde{L} = 16\; m_a^{-1}$. The spikes in the plot are due to the regridding in the simulation and are rapidly damped. 132

B.2 Convergence test for ϕ_{center} showing a convergence between 3rd and 4th order. The convergence test is done with a fixed grid with three different resolutions of 0.25 m_a^{-1}, 0.125 m_a^{-1} and 0.0625 m_a^{-1}. Our evolution scheme is 4th order and the variation in the convergence is due to ϕ passing through 0 during the evolution. 133

C.1 The Hamiltonian constraint violation of the OS-OS initial data before relaxation for $\mathcal{C} = 0.13$ along the axis of the two OS. By choosing $h_{ij} = \gamma_{ij}|_{2x_0}$ the relative Hamiltonian constraint violation (Eq. C.1.1) is reduced by a order of magnitude from 2.6 % to 0.3 %. An additional relaxation routine in χ is implemented after this improvement is applied. 138

C.2 The volume element $\det\gamma$ of the OS-OS initial data before relaxation for $\phi_{m,0}(0) = 0.44$, $\mathcal{C} = 0.13$ on a line in the x direction which goes through the center of both OS. In this example, we have positioned the stars at distance $\pm 15\ m^{-1}$ as opposed to $\pm 30\ m^{-1}$ to illustrate our point. Note that the values are closer to the single OS solution when the metric values are conserved in the center of the OS. 139

C.3 The plot shows the central density of OS with $\mathcal{C} = 0.10$ at a distance $60m^{-1}$ from its counterpart. The high frequency oscillation with wavelength $\lambda \approx 2\pi m^{-1}$ is the natural breathing of the oscillaton while the low frequency mode is caused by the radial mode. Applying the choice $h_{ij} = \gamma_{ij}|_{2x_0}$ removes this radial mode. Animations depicting the evolution of the central density with and without radial modes are available [25, 26] 140

C.4 The plot shows the L^2 norm (Eq. B.11) of the Hamiltonian constraint violation over time, with excision of the black-hole interior (which forms around $t = 700$). The green region shows the relaxation time 141

C.5 Convergence test for the $l = 2$, $m = 0$ mode of $r\Psi_4$, showing convergence between 2nd and 3rd order. The convergence test is done with three different coarsest resolutions of $4m^{-1}$, $2m^{-2}$ and $1m^{-1}$, 6 levels of 2 : 1 refinement, with corresponding finest resolutions of $0.0625m^{-1}$, $(0.0625/2)m^{-1}$ and $(0.0625/4)m^{-1}$. Our evolution scheme is 4th order, and the lowered accuracy is due to the large amount of re-gridding required to track the motion of the oscillaton through to final state. 142

D.1 **Gauss constraint for static string:** We run the same simulation for am infinite static string with $G\mu = 1.6 \times 10^{-2}$ ($\eta = 0.05 M_{\rm Pl}$) with and without damping. We find that the damping stabilises the linear growth in violation. 145

D.2 L^2 **norm of constraints:** Loop with $G\mu = 1.6 \times 10^{-2}$ and $R = 100\ M_{\rm Pl}^{-1}$ remains stable throughout evolution, even after Black hole formation. The initial Hamiltonian constraint is smaller than it can be maintained by the evolution scheme. The momentum constraints violation are negligible throughout. 148

D.3 **Initial relative violation**: Slice through initial data for loop from center through string with $G\mu = 1.6 \times 10^{-2}$ and initial radius $R = 100\ M_{\rm Pl}^{-1}$. The shaded region indicates where the string is located. We find that there is an error of at most 0.3%. 150

D.4 **Toroidal coordinates** encode the symmetry of our cosmic string loops. They are used to generate the initial field configuration, where R defines the radius of the loop. 151

D.5 **Convergence in** $r\Psi_4$ between low, mid and high resolutions giving an overall 2nd-3rd order convergence. The x-axis $t_{\rm ret} = t - r_{\rm ext}$ is the retarded time where $r_{\rm ext}$ is the extraction radius. 152

D.6 **Radial profile of** α **and** f for an infinite static string with gravity in the critical coupling limit ($e = 1$, $\lambda = 2$) and $\eta = 0.05\ M_{\rm Pl}$ ($G\mu = 1.6 \times 10^{-2}$). 153

D.7 **Comparison with Nambu-Goto** for loop with $G\mu = 1.6 \times 10^{-2}$ and initial radius $R = 100\ M_{\rm Pl}^{-1}$ shows agreement. 154

List of tables

1.1 **Overview boundary conditions :** Imposing regularity of the metric gives us the conditions for $r = 0$ and asymptotic flatness the conditions for $r \to \infty$. A free choice is marked as $\times$. 5

1.3 **Summary of various Boson stars models.** We denote the characteristic potential V of each model, its maximum stable mass, the rotational parameter k of solutions that have been constructed and the relevant references. The maximum stable mass for rotating cases was defined at the true maximum mass or the point where an ergoregion appears. 10

1.4 **Overview of boundary conditions :** Imposing regularity of the metric gives us the conditions for $r = 0$ and asymtotic flatness the conditions for $r \to \infty$. A free choice is marked as $\times$. 17

.

Chapter 1

Introduction

Boson stars are unlike the stars we typically consider, in that the particles that make them up are not of fermionic but of bosonic nature. Due to the ability of bosonic particles to share the same quantum state, we can describe them as a single macroscopic wavefunction. Their behaviour is comparable to a wave in a potential, which is generated by the gravitational mass of the boson. The equations describing these states are simple enough to be solved without approximations, unlike Neutron stars. They were first studied in the late 1960s [27–29] and have been the focus of many review articles [30–36]. To accurately describe the most compact solutions where gravity becomes extreme, we leave the regime where Newton's gravity accurately describes most stars, and we need General Relativity. To be able to solve these accurately, we use Numerical Relativity to simulate the evolution over time accurately. With the first measurement of a Black hole binary by the LIGO/Virgo collaboration [5], the recent breakthrough Event Horizon Telescope [37, 38] and BlackHoleCam [39], there is a new window for probing for their existence and thus probing for such exotic objects. While the first part of this chapter will introduce the reader to their taxonomy, the second part of this chapter, will focus on the prospects and challenges of measuring and modelling of Boson stars.

1.1 Taxonomy of Boson stars in General Relativity

The exact properties of the Boson star are strongly dependent on the properties of the bosonic particle. We will discuss how different particle content can influence properties stability or compactness; we discuss real, complex and vector configurations, different potentials and different charges.

We focus on angular momentum, where the behaviour compared to Neutron stars or Black holes differs fundamentally. We also discuss how to generate the solutions from the equations, where we initially focus complex scalar fields, since they are easy and a good proxy for real scalar fields, which are discussed in great detail in later chapters.

1.1.1 Constructing U(1) Scalar stars

We consider a complex scalar field ϕ, which is minimally coupled to gravity with the action[1]

$$S = \int d^4x\sqrt{-g}\left[\frac{R}{16\pi G} - \frac{1}{2}\left(\partial_\alpha\phi^*\partial^\alpha\phi + V(|\phi|)\right)\right] . \tag{1.1}$$

where g is the determinant of the metric and R is the Ricci scalar. Furthermore, the stability of the Boson star is supported by the conserved charge coming from the U(1) symmetry

$$Q = \int d^3x\, corb j^0\sqrt{-g} \ , \tag{1.2}$$

where the Noether current is defined as

$$j^\mu = \frac{i}{2}g^{\mu\nu}\left(\phi^*\partial_\nu\phi - \phi\partial_\nu\phi^*\right) . \tag{1.3}$$

The stress-energy tensor for scalar fields is given by

$$T_{\mu\nu} = \frac{1}{2}\left(\partial_\mu\phi^*\partial_\nu\phi + \partial_\mu\phi\partial_\nu\phi^*\right) - \frac{1}{2}g_{\mu\nu}\left(\partial_\alpha\phi^*\partial^\alpha\phi + V(|\phi|)\right) . \tag{1.4}$$

We decompose the 4-dimensional spacetime into space and time using the ADM formalism. A more formal way to describe this is as a decomposition of the 4-dimensional spacetime into many spacelike hypersurfaces. We define n^μ as the normal vector of these surfaces and

$$\gamma_{\mu\nu} = g_{\mu\nu} + n_\mu n_\nu \ , \tag{1.5}$$

the projection of the 4-dimensional metric on them. We thus use them to project

$$\rho = T_{\mu\nu}n^\mu n^\nu \quad , \quad S_i = T_{\mu\nu}\gamma_i^\mu n^\nu \quad , \quad S_{ij} = T_{\mu\nu}\gamma_i^\mu\gamma_j^\nu \quad , \tag{1.6}$$

---

[1] We use the $-+++$ convention for the metric, and set $= c = 1$. Our Planck mass $M_{\mathrm{Pl}} = 1/\sqrt{G}$.

variable	$r \to 0$	$r \to \infty$
$a(r)$	1	×
$\alpha(r)$	×	×
$\phi_0(r)$	×	0
$\partial_r \phi_0(r)$	0	0

Table 1.1 **Overview boundary conditions :** Imposing regularity of the metric gives us the conditions for $r = 0$ and asymptotic flatness the conditions for $r \to \infty$. A free choice is marked as ×.

where ρ is an energy-density, S^i the energy-momentum flux and S_{ij} the spatial stress. A solution can be found by imposing the harmonic ansatz for the field

$$\phi(r,t) = \phi_0(r)e^{i\omega t} , \tag{1.7}$$

and for the metric

$$ds^2 = -\alpha(r)^2 dt^2 + a(r)^2 dr^2 + r^2(d\theta^2 + \sin^2(\theta) d\varphi^2) . \tag{1.8}$$

Plugging in the ansatz to the Einstein equations together with the Klein-Gordon equations we find the following equations

$$\begin{aligned} \partial_r a &= -\frac{a}{2r}(a^2-1) + 4\pi r a^3 \rho \\ \partial_r \alpha &= \frac{\alpha}{2r}(a^2-1) + 4\pi r \alpha a^2 S^r_r \\ \partial_r^2 \phi_0 &= -\left(1 + a^2 + 4\pi r^2 a^2 (S^r_r - \rho)\right) \frac{\phi}{r} - \left(\frac{\omega^2}{\alpha^2} - \frac{dV}{d|\phi|^2}\right) a^2 \phi_0 , \end{aligned} \tag{1.9}$$

where we impose both asymptotic flatness and the metric to be regular at $r = 0$. This gives the boundary conditions in Table 1.1. To solve this system with boundary conditions at different points, a “shooting” method can be used. This involves tuning values at $r = 0$ until the boundary conditions towards $r = \infty$ are fulfilled. There is one free choice for the boundary $\phi(0)$ and thus the solutions span a one-dimensional family. We can calculate the ADM mass M of the Boson star using the fact that asymptotically the solutions approach the Schwarzschild solution

$$M = \lim_{r\to\infty} \left[\frac{r}{2} \left(1 - \frac{1}{a^2} \right) \right] . \tag{1.10}$$

The properties of the resulting Boson star are strongly dependent on the potential $V(\phi)$, which we will explore in the next sections.

The ansatz $\phi(t,r) = e^{i\omega t}\phi_0(r)$ implies that the phase difference between real and imaginary part is equal to $\pi/2$, and that their respective amplitudes are identical. See however [40, 41], which highlights the existence of more general solutions with different phase differences and different amplitudes.

Stability

To determine perturbative stability of the solutions obtained in the previous section, we consider small radial perturbations of non-rotating spherical Boson stars [42, 43]. Their equation of motion form an eigenvalue equation, where the smallest eigenvalue determines the stability: If the eigenvalue is negative, small perturbations will grow exponentially, which we refer as to be on the unstable branch. If it is positive, the solution is on a stable branch. Since Boson stars are determined by one parameter $\phi_0(0)$ we find the stability flips at

$$\frac{dM}{d\phi_0(0)} = 0 \,, \tag{1.11}$$

where M is the ADM mass of the Boson Star. In Table 1.3, we list the maximum masses for different models. When considering full non-linear perturbations, a similar picture arises. Non-linear stability has been tested numerically [44–47], which confirmed the stability condition in eqn.(1.11) from linear perturbations. Boson stars on the unstable branch can radiate scalar fields (sometimes referred to as gravitational cooling) until they reach a stable star, collapse into a Black hole or disperse completely.

Physical properties of Boson stars

In this section, we show the effect of different potentials on the physical properties of the star. We define the compactness

$$\mathcal{C} = \frac{GM}{R} \,, \tag{1.12}$$

where R is the radius [2] and M is the mass of the Boson star. This is a good measure of how relativistic a star is, with larger values of compactness implying increasingly relativistic stars. Additionally, being more compact reduces the time-scales involved in binary mergers, which helps to reduce the cost of simulations. However, the definition of R can vary depending on where we choose the cutoff, since the solution extends to infinity, thus making the compactness more of an approximate than an exact measure.

---

[2] Since Boson Star do not have a clear boundary and extend to infinity, one has to choose a cutoff.

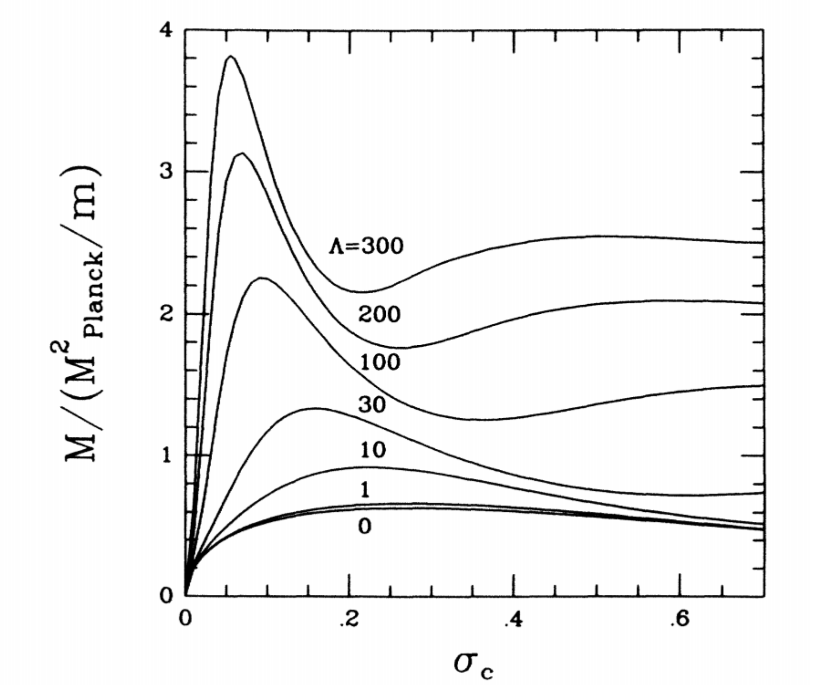

Fig. 1.1 **Mass for self-interacting potential :** Where $\sigma_c = (4\pi)^{1/2}\phi_0$ with several different values for the rescaled self-interaction $\Lambda = \lambda M_{\text{Pl}}^2/(4\pi m^2) = 0, 1, 30, 100, 200, 300$ for the potential $V(\phi) = m^2|\phi|^2 + \frac{1}{2}\lambda|\phi|^4$. The maximum mass and radius increases with larger attractive self-interactions. Figure from [10].

The simplest choice of potential is

$$V = m^2|\phi|^2 \,, \tag{1.13}$$

for which the corresponding Boson star is commonly referred to as a mini-boson star. By solving the eqn. (1.9) we find the most massive solution has $M_{max} = 0.633\ M_{\text{Pl}}^2/m$. One finds that the maximum stable compactness for this potential is $\mathcal{C} = 0.08$.
However when adding an attractive quartic self-interaction [10]

$$V(\phi) = m^2|\phi|^2 + \frac{1}{2}\lambda|\phi|^4 \,, \tag{1.14}$$

one finds that with increasing λ the star can be made arbitrarily massive. For large $\Lambda = \lambda M_{\rm Pl}^2/(4\pi m^2)$ the maximum mass can be expressed as

$$M_{max} \simeq 0.22\, \Lambda^{1/2} \frac{M_{\rm Pl}^2}{m} \qquad \Lambda \gg 1, \tag{1.15}$$

which was found numerically and is not valid for small Λ. However, the increase of compactness is only a factor of ~ 2 at most [48]. More interesingly [49, 50]

$$V(\phi) = m^2|\phi|^2 \left(1 - \frac{|\phi|^2}{\sigma_0^2}\right)^2 \tag{1.16}$$

produces extremely compact stars. The maximum compactness in this case is $C_{max} = 0.35$ which gives rise to a *photon sphere*[3]. Light from inside that region can still escape, but it becomes increasingly more difficult the further behind the photon sphere. This also implies that there is an *innermost stable circular orbit* [4], after which there are no stable circular orbits within, which plays an important role in the accretion of matter. A larger set of potentials has been investigated [51]

$$\begin{aligned} U &= Am^2 \left(\sin\left(\frac{\pi}{2}\left(\beta\sqrt{|\phi|^2} - 1\right)\right) + 1\right) \\ U &= Am^2 \left(\cosh\left(\beta\sqrt{|\phi|^2}\right) - 1\right) \\ U &= Am^2 \left(e^{\beta^2|\phi|^2} - 1\right) \end{aligned} \tag{1.17}$$

where A is chosen to be such that locally the potential is $\approx m^2|\phi|^2 + \mathcal{O}(|\phi|^3)$. The maximum masses for $\beta = 1$ can be found in Table 1.3.

The harmonic ansatz makes an implicit assumption that the phase-difference between real and imaginary parts tends to be exactly $\pi/2$, with equal amplitudes for both real and imaginary parts of the scalar field. The full family of solutions is therefore likely to be much bigger [40, 41] than the one-parameter family of solutions discussed.

---

[3] which is an imagined surface on which null-geodesics can orbit (which only exists for compactness $C > 1/3$ in Schwarzschild coordinates)

[4] ISCO, which only exists for compactness $C > 1/6$ in Schwarzschild coordinates

model name	**potential** V	**k**	**max. stable mass**	**reference**
Complex scalar field				
mini-boson	$m^2\lvert\phi\rvert^2$	0	$0.633M_{\rm Pl}^2/m$	[28, 27, 29]
		1	$1.315M_{\rm Pl}^2/m$	[13, 52]
		2	$2.216M_{\rm Pl}^2/m$	[13]
		3	$3.206M_{\rm Pl}^2/m$	[13]
		4	$4.790M_{\rm Pl}^2/m$	[13]
self interacting	$m^2\lvert\phi\rvert^2+\frac{1}{2}\lambda\lvert\phi\rvert^4$	0	$0.22\ \Lambda^{1/2}M_{\rm Pl}^2/m$	[10]
			with $\Lambda=\lambda\frac{M_{\rm Pl}^2}{4\pi m^2}\gg 1$	[10]
		1	$3.14M_{\rm Pl}^2/m$	[13]
		2	$3.48M_{\rm Pl}^2/m$, $\Lambda=200$	[13]
		3	$4.08M_{\rm Pl}^2/m$, $\Lambda=200$	[13]
		4	$5.59M_{\rm Pl}^2/m$, $\Lambda=200$	[13]
solitonic	$m^2\lvert\phi\rvert^2\left(1-\frac{\lvert\phi\rvert^2}{\sigma_0^2}\right)^2$	0	$0.0198\ M_{\rm Pl}^4/(m\sigma_0^2)$	[49, 50]
Sine-Gordon	$Am^2\left[\sin\left(\frac{\pi}{2}\right.\right.$			[51]
	$\left.\left.\left(\sqrt{\lvert\phi\rvert^2}-1\right)\right)+1\right]$	0	$0.620\ M_{\rm Pl}^2/m$	[51]
Cosh-Gordon	$Am^2\left[\right.$			[51]
	$\left.\cosh\left(\sqrt{\lvert\phi\rvert^2}\right)-1\right]$	0	$0.638\ M_{\rm Pl}^2/m$	[51]
Liouville	$Am^2\left(e^{\lvert\phi\rvert^2}-1\right)$	0	$0.666\ M_{\rm Pl}^2/m$	[51]
Charged Complex scalar field (with charge e)				
mini-boson	$m^2\phi^2$	0	$\approx\frac{0.44}{\sqrt{e_{crit}-e}}M_{\rm Pl}^2/m$	[11, 53]
self interacting	$m^2\lvert\phi\rvert^2+\frac{1}{2}\lambda\lvert\phi\rvert^4$	0	$\approx\frac{0.226}{\sqrt{e_{crit}-e}}\lambda^{1/2}M_{\rm Pl}^2/m$	[11, 53]
Real scalar field				
Oscilloton	$\frac{1}{2}m^2\phi^2$	0	$0.605M_{\rm Pl}^2/m$	[54–56]
self interacting	$\frac{1}{2}m^2\phi^2+\frac{1}{4}\lambda\phi^4$	0	$0.694M_{\rm Pl}^2/m$, $\Lambda=1$	[57]
			with $\Lambda=\lambda\frac{M_{\rm Pl}^2}{8\pi m^2}\gg 1$	[57]
		0	$0.770M_{\rm Pl}^2/m$, $\Lambda=2$	[57]
		0	$0.854M_{\rm Pl}^2/m$, $\Lambda=3$	[57]
T-models	$V_0\tanh^2(\phi/\Lambda)$	0	$\gtrsim 0.44\ M_{\rm Pl}^2/m$, $\Lambda=\frac{0.14}{\sqrt{8\pi}}$	[58]
		0	$\gtrsim 0.41\ M_{\rm Pl}^2/m$, $\Lambda=\frac{0.17}{\sqrt{8\pi}}$	[58]
		0	$\gtrsim 0.41\ M_{\rm Pl}^2/m$, $\Lambda=\frac{0.2}{\sqrt{8\pi}}$	[58]

model name	potential V	k	max. stable mass	reference
Real scalar field				
E-models	$V_0\left(1-e^{-\phi/\Lambda}\right)$	0	$\gtrsim 0.41\, M_{\rm Pl}^2/m$, $\Lambda=\frac{1}{\sqrt{8\pi}}$	[58]
		0	$\gtrsim 0.46\, M_{\rm Pl}^2/m$, $\Lambda=\frac{2}{\sqrt{8\pi}}$	[58]
KKLT	see [58]	0	$\gtrsim 0.33\, M_{\rm Pl}^2/m$, $\lvert W_0\rvert=10^{-2}$	[58]
Axions	$m^2 f^2\,[1-\cos(\phi/f_a)]$	0	(see Fig. 2.1)	[17]
Complex vector				
Proca	$\frac{1}{2}m^2 A_\mu A^{*\mu}$	0	$1.058 M_{\rm Pl}^2/m$	[12]
		1	$1.568 M_{\rm Pl}^2/m$	[12]
		2	$2.377 M_{\rm Pl}^2/m$	[12]
		3	$3.247 M_{\rm Pl}^2/m$	[12]
self-interacting	$\frac{1}{2}m^2 A_\mu A^{*\mu}$ $-\frac{1}{4}\lambda(A_\mu A^{*\mu})^2$	0	$0.0057\times$ $\ln\left(\frac{\lambda M_{\rm Pl}^2}{m^2}\right)\sqrt{\lambda}\frac{M_{\rm Pl}^3}{m^2}$	[59] [59]
higher-order	$\frac{1}{2}m^2 A_\mu A^{*\mu}$ $-\frac{1}{2}(A_\mu A^{*\mu})^2$ $+\frac{1}{3}(A_\mu A^{*\mu})^3$	0	$1.04 M_{\rm Pl}^2/m$	[60]
Charged Complex vector				
Proca	$\frac{1}{2}m^2 A_\mu A^{*\mu}$	0	$1.56 M_{\rm Pl}^2/m$, $e=0.5$	[60]
higher-order	$\frac{1}{2}m^2 A_\mu A^{*\mu}$ $-\frac{1}{2}(A_\mu A^{*\mu})^2$ $+\frac{1}{3}(A_\mu A^{*\mu})^3$	0	$1.52 M_{\rm Pl}^2/m$, $e=0.5$	[60]
Real vector				
massive	$\frac{1}{2}m^2 A_\mu A^{\mu}$	0	$1.074 M_{\rm Pl}^2/m$	[61]
ℓ Boson star				
mini-boson	$m^2\lvert\phi\rvert^2$	0	$0.633 M_{\rm Pl}^2/m$	[62, 28, 27, 29]
		1	$1.18 M_{\rm Pl}^2/m$	[62]
		2	$1.72 M_{\rm Pl}^2/m$	[62]
		3	$2.25 M_{\rm Pl}^2/m$	[62]
		4	$2.78 M_{\rm Pl}^2/m$	[62]

Table 1.3 **Summary of various Boson stars models.** We denote the characteristic potential V of each model, its maximum stable mass, the rotational parameter k of solutions that have been constructed and the relevant references. The maximum stable mass for rotating cases was defined at the true maximum mass or the point where an ergoregion appears.

Charged Boson stars

Charged Boson stars were first introduced by [11] and later in [53]. We define the gauged action

$$S = \int d^4x\sqrt{-g}\left[\frac{R}{16\pi G} + (D_\mu\phi)^*(D^\mu\phi) + \frac{1}{4}F_{\mu\nu}F^{\mu\nu} + V(\phi)\right] , \tag{1.18}$$

with $D_\mu = \partial_\mu + ieA_\mu$, $F_{\mu\nu} = \partial_\mu A_\nu - \partial_\nu A_\mu$ and A_μ the gauge field. For charge values of the dimensionless charge $\tilde{e}^2 = e^2 M_{\text{Pl}}^2/8\pi m^2 > e_{crit}^2 = 1/2$ (see fig 1.2) there are no physical solutions of the system. This is due to the electrical repulsion overpowering the gravitational attraction. We can define the Noether charge

$$N = \int d^3x\, j^0\sqrt{-g} , \tag{1.19}$$

where j^μ is the Noether current corresponding to the action. The overall charge $Q = eN$ then manifests in the asymptotic behaviour of the Boson star

$$g_{rr} = \left(1 - \frac{2M}{r} + \frac{Q^2}{4\pi r^2}\right)^{-1} \quad r \gg M . \tag{1.20}$$

In [11] these solutions were studied using the potential

$$V(\phi) = \frac{1}{2}m^2|\phi|^2 + \frac{1}{4}\lambda|\phi|^4 . \tag{1.21}$$

where the scaling in eqn.(1.15) for large Λ is still valid, one finds that with increasing electrical charge the star becomes more massive

$$M \approx \frac{0.44}{\sqrt{e_{crit} - e}}\,\frac{M_{\text{Pl}}^2}{m}. \tag{1.22}$$

However, the behaviour of the radius is similar

$$R \approx \frac{1.5}{\sqrt{e_{crit} - e}}\,\frac{1}{m} . \tag{1.23}$$

The stability under small radial perturbations has been studied in [63], where they showed that for central densities $\rho < \rho_{crit}$ the Boson star is stable, were ρ_{crit} is the density of the most massive star.

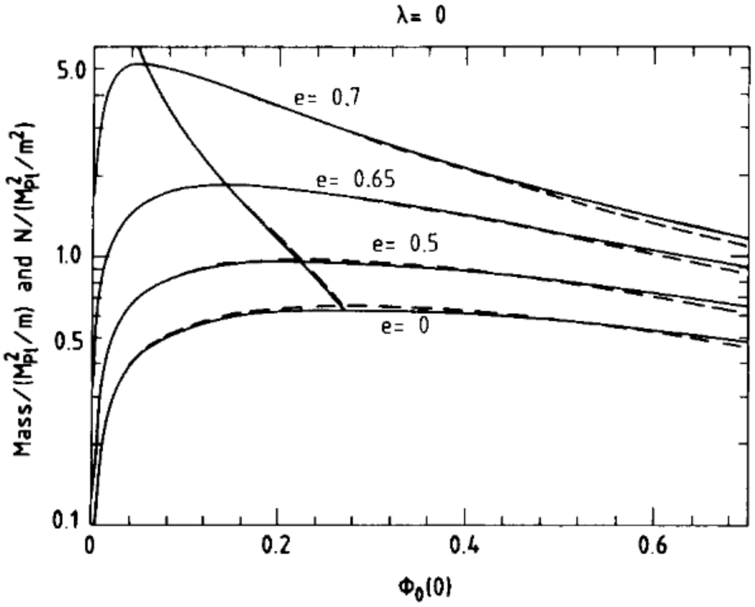

Fig. 1.2 **Charged Boson star solutions :** The mass and size becomes larger with increasing charge. However, there is a maximum charge $e_{crit} = 0.707$ for which the electromagnetic repulsion overpowers gravity. The addional line shows where the maxima are located. Figure from [11].

Vector stars

We consider a complex vector field A_μ, which is minimally coupled [12, 64] to gravity with the action

$$S = \int d^4x\sqrt{-g}\left[\frac{R}{16\pi G} - \frac{1}{4}F_{\mu\nu}F^{*\mu\nu} - V(A_\mu A^{*\mu})\right] , \tag{1.24}$$

due to the extra mass term

$$V(A_\mu A^{*\mu}) = \frac{1}{2}m^2 A_\mu A^{*\mu} \tag{1.25}$$

we lose the gauge choice and the Proca condition

$$\nabla_\mu A^\mu = 0 \tag{1.26}$$

becomes a requirement. The harmonic ansatz for the vector field is

$$\begin{aligned} A^0 &= f(r)e^{i\omega t} \\ A^r &= ig(r)e^{i\omega t} . \end{aligned} \tag{1.27}$$

As in the scalar field case there is a U(1) symmetry which gives rise to a conserved Noether charge

$$Q = \int_V d^3x j^0 \sqrt{-g} \tag{1.28}$$

with the Noether current

$$j^\alpha = \frac{i}{2}\left(F^{*\alpha\beta}A_\beta - F^{\alpha\beta}A^*_\beta\right) . \tag{1.29}$$

The maximum mass of such objects has been found to be $M = 1.058 M_{\text{Pl}}^2/m$ (see Fig. 1.3) thus making it twice as massive as an scalar Boson star. The stability was studied non-linearly in [65] with very similar results to scalar Boson stars, where it flips at the maximum mass.

A study of self-interacing vector Boson stars

$$V(A_\mu A^{*\mu}) = \frac{1}{2}m^2 A_\mu A^{*\mu} - \frac{1}{4}\lambda (A_\mu A^{*\mu})^2 \tag{1.30}$$

has been performed in [59]. The scaling found for values interpolated between $20 \geq \frac{\lambda}{8\pi} \geq 50$

$$M_{max} \approx \left(1.383 - 0.005099\,\frac{\sqrt{\lambda}M_{\text{Pl}}}{m} + \left(-0.03967 + 0.005675\frac{\sqrt{\lambda}M_{\text{Pl}}}{m}\right)\ln\left(\frac{\lambda M_{\text{Pl}}^2}{m^2}\right)\right)\frac{M_{\text{Pl}}^2}{m} \tag{1.31}$$

where the asymptotic behaviour

$$M_{max} \approx 0.005675\ \ln\left(\frac{\lambda M_{\text{Pl}}^2}{m^2}\right)\ \sqrt{\lambda}\frac{M_{\text{Pl}}^3}{m^2} \tag{1.32}$$

deviates strongly from the self interacting scalar Boson stars case, which behaves as $M_{max} \approx \sqrt{\lambda}M_{\text{Pl}}^2/m$.

The formation of Proca stars was studied in [66], where similarly to scalar Boson stars indication for more general solutions of Boson Stars were found, deviating from the harmonic solutions. Furthermore, solutions for asymptotic anti-de Sitter spacetime have been studied [64] as well as charged Proca stars [60].

Real Scalar Solitons

In this section, we consider real scalar field solitons [54–56]. We lose the U(1) symmetry, and therefore the Noether charge that was crucial for the stability. Thus the solutions found are only quasi-stable on very long time-scales. Similarly, one can find solutions for real vector fields [61].

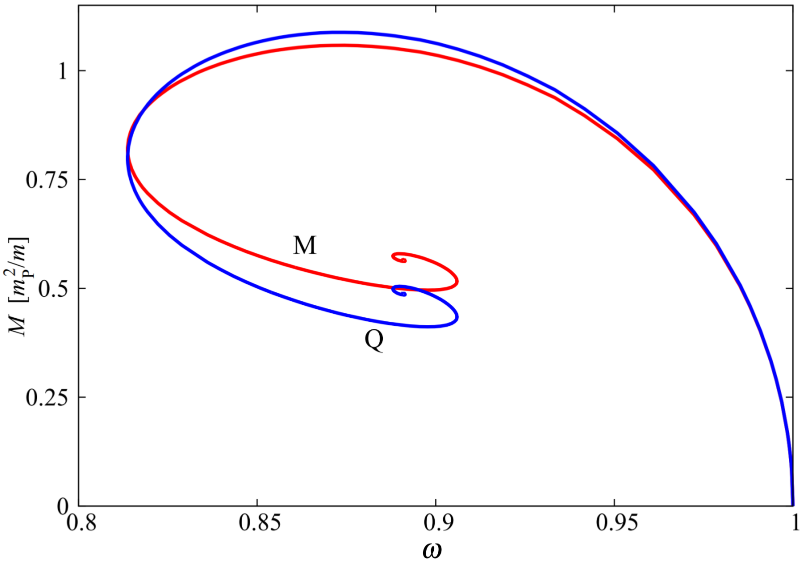

Fig. 1.3 **Proca Star Solutions Space :** Both the Noether charge Q and ADM mass against the frequency ω of the Proca star. Similar to Boson stars, points on the left to the maximum are unstable. Figure from [12].

We consider a free, massive, real scalar field, which is minimally coupled to gravity with the action

$$S = \int d^4x\sqrt{-g}\left[\frac{R}{16\pi G} - \frac{1}{2}\partial_\mu\phi\partial^\mu\phi - V(\phi)\right], \tag{1.33}$$

In this section, we focus on Boson stars referred to as Oscillatons, which have the following potential

$$V(\phi) = \frac{1}{2}m^2\phi^2 \,. \tag{1.34}$$

To obtain the radial profiles we use the ansatz for a spherically symmetric line element:

$$ds^2 = -\alpha^2 dt^2 + a^2 dr^2 + r^2(d\theta^2 + \sin^2(\theta)d\varphi^2), \tag{1.35}$$

with rescaled variables

$$\begin{aligned} r &\rightarrow \frac{r}{m}\,, \\ \phi &\rightarrow \frac{\phi}{\sqrt{8\pi G}}\,. \end{aligned} \tag{1.36}$$

We define the quantities $A = a^2$, $C = \frac{a^2}{\alpha^2}$. We can rewrite the Einstein-Klein-Gordon equation as

$$\begin{aligned}
A^{(0,1)}(t,r) &= \frac{1}{2}rA(t,r)\phi^{(1,0)}(t,r)^2C(t,r) + \frac{1}{2}rA(t,r)\phi^{(0,1)}(t,r)^2 + \frac{1}{2}rA(t,r)^2\phi(t,r)^2 \\
&\quad - \frac{A(t,r)^2}{r} + \frac{A(t,r)}{r} , \\
C^{(0,1)}(t,r) &= rA(t,r)\phi(t,r)^2C(t,r) - \frac{2A(t,r)C(t,r)}{r} + \frac{2C(t,r)}{r} \\
\phi^{(0,2)}(t,r) &= \frac{1}{2}rA(t,r)\phi^{(0,1)}(t,r)\phi(t,r)^2 \\
&\quad - \frac{A(t,r)\phi^{(0,1)}(t,r)}{r} + A(t,r)\phi(t,r) + \frac{1}{2}C^{(1,0)}(t,r)\phi^{(1,0)}(t,r) , \\
&\quad - \frac{\phi^{(0,1)}(t,r)}{r} + \phi^{(2,0)}(t,r)C(t,r) .
\end{aligned} \tag{1.37}$$

where the superscripts refer to derivatives with respect to time t and radial coordinate r, respectively. We rewrite the variables in Fourier space

$$\begin{aligned}
\phi(t,r) &= \sum_{j=1}^{j_{max}} \hat{\phi}_j(r)\cos(j\omega t) , \\
A(t,r) &= \sum_{j=0}^{j_{max}} \hat{A}_j(r)\cos(j\omega t) , \\
C(t,r) &= \sum_{j=0}^{j_{max}} \hat{C}_j(r)\cos(j\omega t) ,
\end{aligned} \tag{1.38}$$

where j_{max} is the maximum order in the Fourier expansion to which the solution is approximated. Additionally, we scale the time

$$t \to \frac{t}{\omega} . \tag{1.39}$$

To solve these equations it is best to calculate the right-hand side (RHS) as a series of convolutions $(\hat{f} * \hat{g})_j$ using the Fourier-transformed equations. We simplify eq. (1.37) in a format which only contains multiplication. As for Boson stars we require asymptotic flatness and regularity at $r = 0$ which gives the condition in Table 1.4. We employ a shooting method to solve for the boundary conditions in Table 1.4. These profiles for ϕ in $m^2\phi^2$ theory are

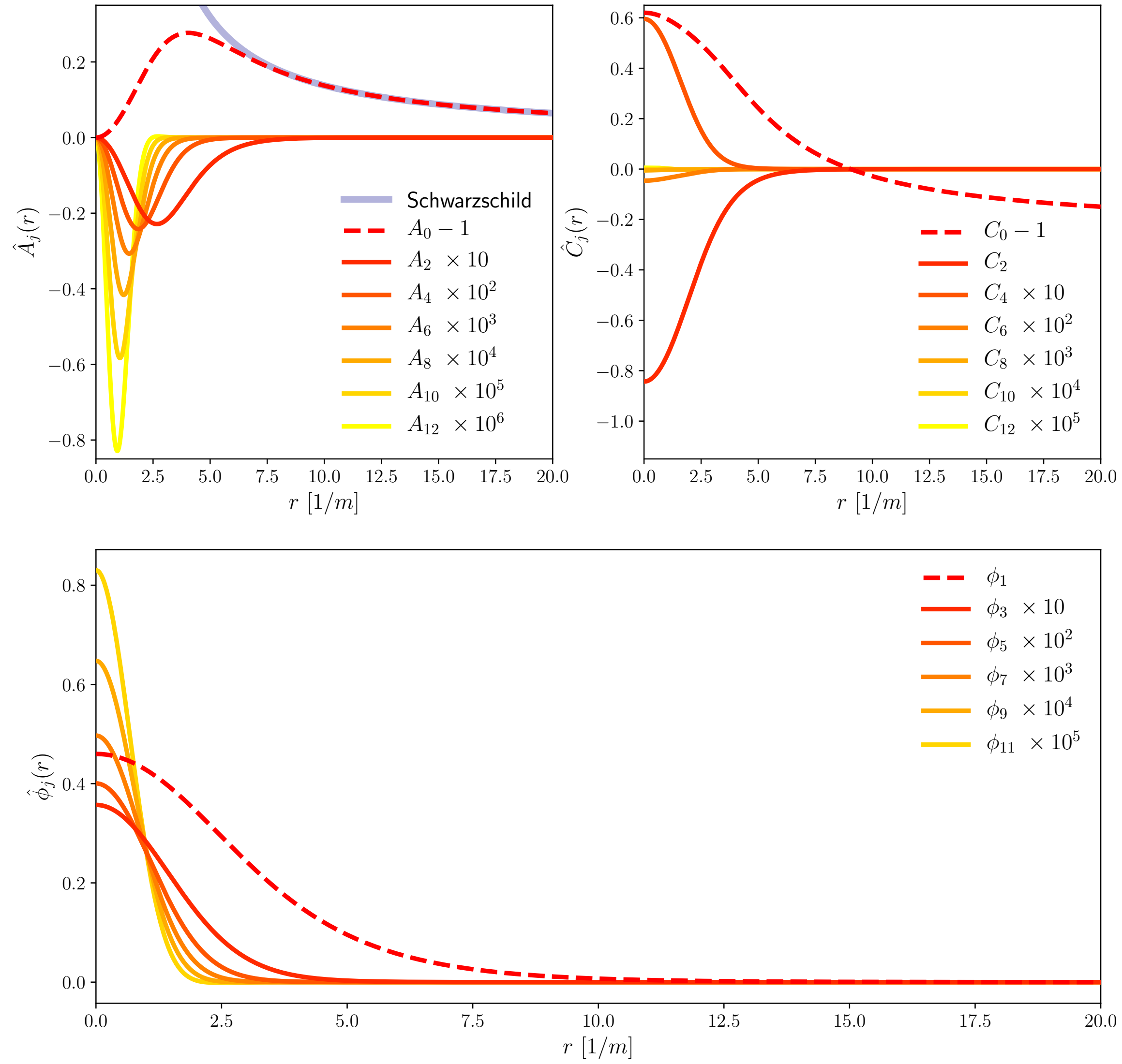

Fig. 1.4 **Oscillatons Solutions :** The solutions for all modes $\hat{\phi}_j(r)$, $\hat{C}_j(r)$, $\hat{A}_j(r)$ of a maximally massive oscilloton ($\phi_0(0) = 0.46$) and with $r_{max} = 23.2\ m^{-1}$. We find that approximately every higher mode is suppressed by one order of magnitude, thus showing very fast convergence in j. Asymtotically in r, the solutions converge to the Schwarzschild spacetime, where we match with $M = 0.605\ \mathrm{M}_{pl}^2/m$, the measured ADM mass.

described in e.g. Refs. [55, 67, 56]. They are a one-parameter family, for which a larger ADM mass leads to a smaller radius and a higher central field value.

Furthermore, we note that unlike complex Boson stars, the metric is not static, but oscillates. The amplitude of this oscillation vanishes towards infinity as the solutions approach the Schwarzschild metric. When solving for the ADM mass (see Fig. 1.5) we find,

variable	mode	$r \to 0$	$r \to \infty$
$\hat{A}_j(r)$	$j = 0$	1	×
$\hat{A}_j(r)$	$j > 0$	0	0
$\hat{C}_j(r)$	$j = 0$	×	×
$\hat{C}_j(r)$	$j > 0$	×	0
$\hat{\phi}_j(r)$	$\forall j$	×	0
$\partial_r \hat{\phi}_j(r)$	$\forall j$	0	0

Table 1.4 **Overview of boundary conditions :** Imposing regularity of the metric gives us the conditions for $r = 0$ and asymtotic flatness the conditions for $r \to \infty$. A free choice is marked as ×.

similar to the complex scalar case in section 1.1.1, a stable (S) and a unstable (U) branch, which is separated by the maxima $\frac{dM}{d\phi_0(0)} = 0$. Stability has been tested in [55] with non-linear radial perturbations. Small perturbations in the S-branch will settle again into configurations in the S-branch. Small perturbations in the U-branch will radiate and also settle into the S-branch. Large enough perturbations will collapse both U and S branch solutions into Black holes.

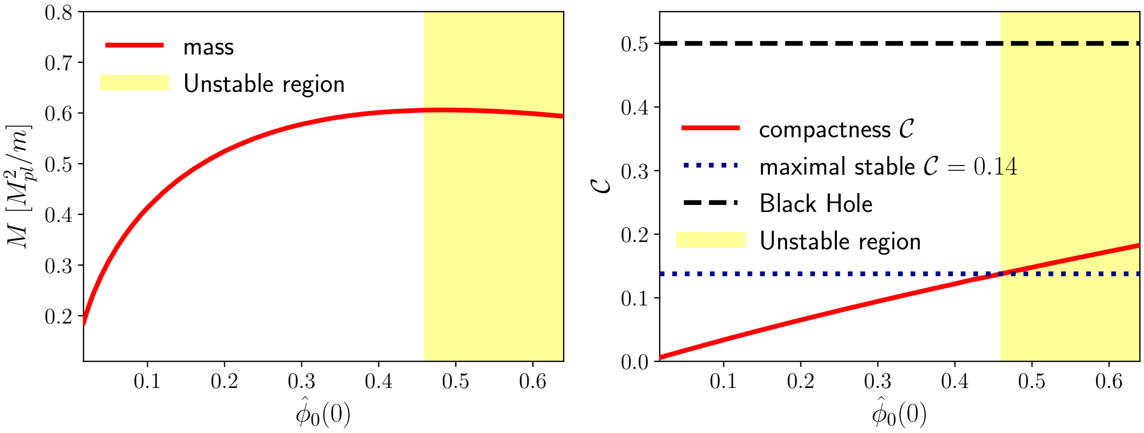

Fig. 1.5 **Overview of $m^2\phi^2$ Oscillatons :** The figure on the left shows the defining parameter $\hat{\phi}_0$ vs the ADM mass M_{ADM} of the soliton. We can see that the most stable solution can reach a maximum mass of $M = 0.605 M_{\text{Pl}}^2/m$. The right plot depicts $\hat{\phi}_0(0)$ against the compactness $\mathcal{C}$. We see that we can reach a maximum stable compactness of $\mathcal{C} \sim 0.14$.

Beyond $m^2\phi^2$

Previous sections focused on solitons with a $V(\phi) = \frac{1}{2}m^2\phi^2$ potential, yet there are many other physically motivated potentials that we summarise in Table 1.3. Similar to complex scalar fields [57] solutions for a self-interacting potential

$$V = \frac{1}{2}m^2\phi^2 + \frac{1}{4}\lambda\phi^4 \ . \tag{1.40}$$

have been constructed. In [57], the solutions for $\Lambda = \lambda/(8\pi Gm^2) = 1,2,3$ were generated. Considering the similarities between complex scalar Boson stars with a massive potential and Oscillatons (real scalar field Boson stars with a massive potential), the question of whether this still holds for other potentials as well. For future work, it would be interesting to study whether the scaling for complex Boson stars from eq. (1.15) could be reproduced for real scalar fields. As the self-interaction Λ increases, higher order modes $j > 0$ (see eq. (1.38) or Fig. 2.1) become more relevant , which indicates different behaviour.

In this thesis (see chapter 2), we study the effective axion potential $m^2 f^2 \left[1-\cos(\phi/f_a)\right]$ [17]. A wide study of potentials was performed by [58]. These are not found by making a periodic ansatz as before, rather by inserting the solutions for a $m^2\phi^2$ potential and evolve them until the solutions settle down to a stable state. There are some caveats, e.g. the radial profiles are significantly harder to generate and likely, the resulting star is not in its ground state. However, this implicitly shows stability against large perturbations.

1.1.2 Rotating Boson stars

In this section, we will consider Boson stars with angular momentum. This is of importance since we are discussing merging binary systems in the next sections, which contain a large amount of orbital angular momentum that will go partly to the resulting Boson star or Black hole. Thus knowledge of rotating states is crucial to understand binary systems.

In [68], it was shown that there are no arbitrarily slowly rotating Boson stars. However counterintuitively, it turns out they can rotate rapidly, due to their rotation being quantised. Thus there is a gap in angular momentum between a non-rotating star and the first spinning state. The relativistic solutions [13, 69, 52] use the scalar-field ansatz

$$\phi(t,r,\theta,\varphi) = e^{i(\omega t - k\varphi)}\phi(r,\theta) \ , \tag{1.41}$$

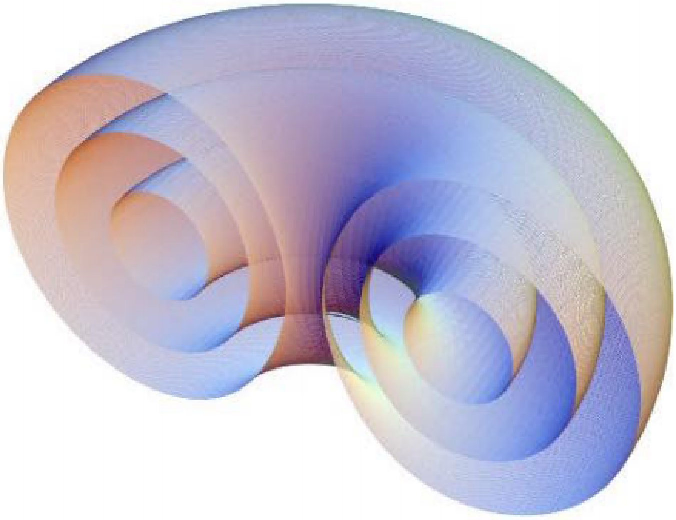

Fig. 1.6 **Illustration of Rotating Boson star:** Energy isosurfaces for a scalar configuration with $k = 2$. Figure from [13].

and the metric ansatz

$$ds^2 = -\alpha^2 dt^2 + A\ (dr^2 + r^2 d\theta^2) + B\ r^2 \sin(\theta)^2 (d\varphi + \beta^\varphi dt)^2\ . \tag{1.42}$$

The angular momentum is given by

$$J = kQ\ , \tag{1.43}$$

where Q is the Noether charge of the Boson star and k an integer. Due to regularity we have $\phi(t, 0, \varphi, \theta) = 0$, which causes the solutions to be torus-shaped as illustrated in Fig. 1.6.

It has been shown in [70] that scalar field configurations with an ergoregion [5] and with no horizon are unstable. For scalar and vector Boson stars with a massive potential (see Fig. 1.7) it has been shown that an ergoregion forms for some configurations[13, 12], thus making these unstable. This changes when self-interactions are introduced, in which case no solution with ergoregion has been found [13].

The first spinning solutions were obtained by [69], which confined itself to the weakly relativistic regime with values of $k = 1, 10, 500$. Subsequently, relativistic solutions were obtained [52] for $k = 1$. There was disagreement on these results in [71] with $k = 1, 2$, which could not reproduce the same maximum masses and described regularity issues in

---

[5] i.e. a spacetime where the killing vector ∂_t becomes spacelike

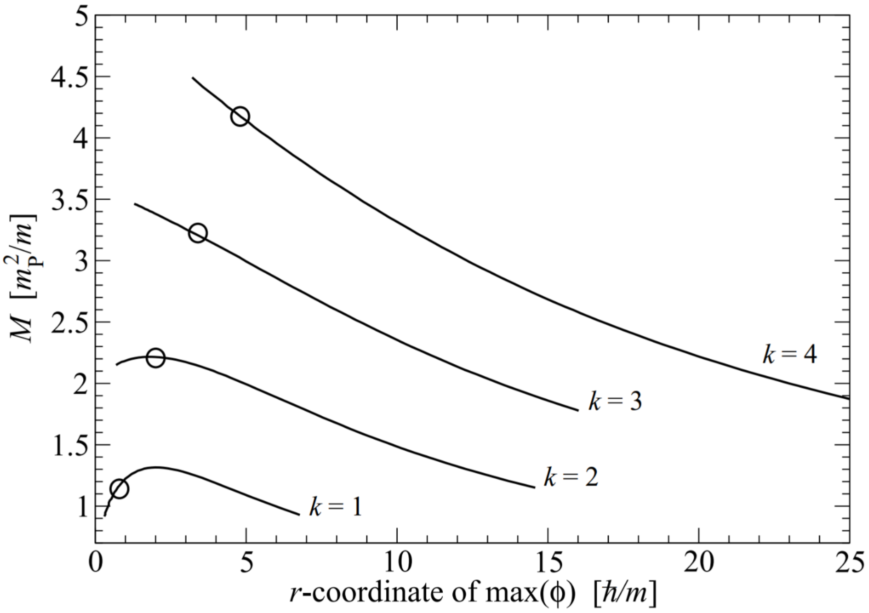

Fig. 1.7 **Solutions of rotational mini-boson stars** with rotating quantum numbers $k = 1,..,4$. Solutions left of the marked points are unstable due to the appearance of ergoregions. Figure from [13].

his solutions. This was then resolved by [13], which reproduced the results [52] and obtain stable relativistic solution for $k = 1,2,3,4$ (using the publicly available KADATH[6] library). Non-relativistic spinning solutions have been studied in [72] and [73].

Rotating solutions of Boson stars are difficult to obtain, because the scalar fields need to break spherical symmetry to acquire angular momentum. However, there exist special spinning solutions which reduce the equation of motion to a one-dimensional problem [62] by using and increasing the number of fields N. These can be obtained using the ansatz

$$\phi_{km} = \phi_k(t,r)Y^{km}(\varphi,\theta) \ , \tag{1.44}$$

where $Y^{km}(\varphi,\theta)$ is a spherical harmonic, with $k = (N-1)/2$, and N is the number of fields. For larger k, the compactness increases significantly, from $\mathcal{C} = 0.08$ for $k = 0$ (which gives the normal massive Boson stars) to $\mathcal{C} = 0.14$ for $k = 4$.

The work of [74] studied the stability of scalar and vector solutions. Using the fully non-linear evolution, they found that after some time the stars would develop instabilities, causing the separation into two Boson stars or collapse into a Black hole. Furthermore, solutions with non-minimal couplings have been studied [75], as well as Proca stars [12], charged Boson stars [76], Dirac stars [77], and multistate rotating stars [78].

---

[6] see https://kadath.obspm.fr/

1.2 Detecting Boson stars

1.2.1 Gravitational Waves from Binaries with Boson stars

The recent detection of Gravitational Waves from Black hole (BH) binaries [5] by the LIGO/Virgo collaboration marked the start of a new era of observations. In the next two sections, we explore the possibility of detecting or constraining the existence of Boson star binaries by their emission of gravitational waves.

Before merger - Tidal deformations

Firstly, we focus on the gravitational wave signal emitted before merger [14]. The tidal deformability of non-spinning Boson stars has been the subject of several studies [79, 14, 80]. We parametrise the gravitational wave signal emitted by the binary as

$$\tilde{h}(f) = \mathcal{A}(f)e^{i\psi(f)} \,, \tag{1.45}$$

where $\tilde{h}(f)$ is the strain and f the orbital frequency. The Boson star distinguishes itself by the energy transfer from orbital energy into deformation energy, which causes the system to inspiral faster. There might be further sources of energy-loss, for example scalar radiation, which requires more detailed studies. This has been studied for Black hole binaries with scalar wigs in scalar Gauss-Bonnet gravity [81]. We use the stationary-phase approximation

$$\frac{d^2\psi}{d\Omega^2} = 2\frac{(dE/d\Omega)}{\dot{E}_{GW}} \tag{1.46}$$

where $\dot{E}_{GW}$ is the energy flux of GWs and $\Omega = \pi f$ the orbital frequency. One can find the solutions to the previous equation

$$\psi = \frac{3}{128\,(\pi\mathcal{M}f)^{5/2}}\left(1 + \ldots + (\alpha_{tidal} + \ldots)x^5 + \ldots\right) \tag{1.47}$$

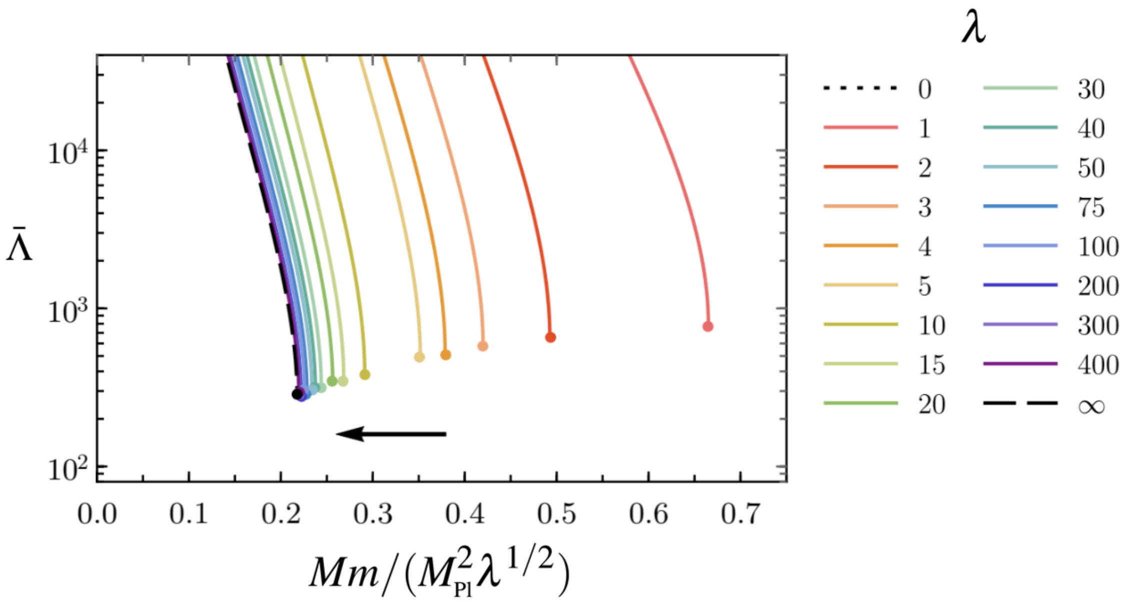

Fig. 1.8 **Tidal deformability [14] :** Tidal deformations for massive self-interacting Boson stars. A large lower bound of $\Lambda \geq 280$ allows the distiction between Boson stars and other compact object (i.e. Neutron stars or Black holes).

where $M = M_1 + M_2$ and $M_{1,2}$ are the masses corresponding to the compact objects in the binary, $x = (\pi M f)^{2/3}$, $\nu = M_1 M_2/M^2$, $\mathcal{M} = \nu^{3/5} M$ and

$$\alpha_{tidal} = -\frac{39}{2}\tilde{\Lambda}\,, \tag{1.48}$$

with the weighted tidal deformation

$$\tilde{\Lambda} = \frac{16}{13}\left(\left(1+12\frac{M_2}{M_1}\frac{M_1^5}{(M_1+M_2)^5}\right)\bar{\Lambda}_1 + \left(1+12\frac{M_1}{M_2}\frac{M_2^5}{(M_1+M_2)^5}\right)\bar{\Lambda}_2\right)\,, \tag{1.49}$$

where $\bar{\Lambda}_i$ are the individual deformability parameters. They can be best understood by looking at the metric far away from the Boson star in the local frame

$$g_{tt} = -1 + \frac{2\,M}{r} + \frac{3\mathcal{Q}_{ij}}{r^3}\left(n^i n^j - \frac{1}{3}\delta^{ij}\right) - \mathcal{E}_{ij}x^i x^j + \mathcal{O}(r^3)\,, \tag{1.50}$$

where x^i are the coordinates, $n^i = x^i/r$ the normal vector, $\mathcal{E}_{ij}$ is the external force and $\mathcal{Q}_{ij}$ the quadrupol induced by it. The tidal deformability $\bar{\lambda}$ is defined by the relation

$$\mathcal{Q}_{ij} = -\bar{\lambda}\mathcal{E}_{ij} \; . \tag{1.51}$$

We can define the dimensionless quantity

$$\bar{\Lambda} = \bar{\lambda}/M^5 \; , \tag{1.52}$$

which was calculated in [14] for a massive potential with self-interactions (see Fig. 1.8)

$$V(\phi) = \frac{1}{2}m^2|\phi|^2 + \frac{1}{4}\lambda|\phi|^4 \; , \tag{1.53}$$

as well as for solitonic stars

$$V(\phi) = m^2|\phi|^2 \left(1 - \frac{|\phi|^2}{\sigma_0^2}\right)^2 \; . \tag{1.54}$$

Furthermore, [14] found that for Boson stars with self-interactions a lower bound on the deformability of $\bar{\Lambda} \geq 280$, which is much larger then the one for Neutron stars ($\bar{\Lambda} \geq 10$) and for Black holes ($\bar{\Lambda} = 0$). This gap in deformability permits a clear distinction between self-interacting Boson stars and NS/BH.

This distinction becomes more difficult for solitonic Boson stars, since they have $\bar{\Lambda} \geq 1.3$, making it hard to distinguish them from NS/BH with just one measurement. However, combining measurements may allow us to make this distinction, as discussed in [14].

There is the possibility that self-interacting Boson stars can be distinguished from NS/BH with Advanced LIGO and Virgo, though 3G detectors have better chances.

Merger

The previous section focused on the inspiral part of the signal, though at merger the full non-linearity of the matter and Einstein equations will be dominant, thus potentially making it much easier to distinguish Boson stars from NS/BH. However, to adequately model the system and its gravitational wave output, numerical methods are needed. In [82], the first merger of Boson stars was simulated and subsequently followed by [83, 71, 84, 85]. For real scalar fields, [86] performed the first study, with Proca stars studied in [87]. The merger of Boson stars with different scalar sectors and of mixed fermion-boson stars have been studied in [88, 89], respectively. In chapter 4, we will discuss the head-on mergers as discussed in [19].

In most of the mentioned papers [84, 89, 83, 71, 84, 82, 86], the initial data is obtained by linearly superposing two separate single object solutions

$$g_{\mu\nu} = g^1_{\mu\nu} + g^2_{\mu\nu} - \eta_{\mu\nu} \ , \tag{1.55}$$

where $\eta_{\mu\nu}$ is the Minkowski metric and $g^i_{\mu\nu}$ is the metric of a single Boson star. This operation creates a spacetime inconsistent with general relativity and creates Hamiltonian and Momentum constraint violations. We also found that this initial data can create radial modes which have significant effects on the dynamics, as well as giving unphysical gravitational wave signals. In this thesis, we present a simple solution to these problems for the case of head-on mergers, which is described in detail in Appendix C.1.1. This eliminates any excitations that we could measure for the mergers studied.

In contrast to the parameters defining a binary Black hole, Boson stars have additional parameters, like their relative phase or their rotation. For complex stars, due to the sign of rotation in field-space

$$\phi = \phi_1 e^{i\omega t} + \phi_2 e^{-i\omega t} \ , \tag{1.56}$$

the two stars have a Noether charge with opposite signs and, hence, a zero net charge. This indicates that in the final state all matter is dispersed, which has been confirmed in simulations [84]. This discussion only applies to complex fields, since real scalar fields do not have a sign of rotation.

Furthermore, the phase-difference δ between the two stars

$$\phi = \phi_1 e^{i\omega t} + \phi_2 e^{i\omega t + i\delta} \ , \tag{1.57}$$

is crucial for an equal mass merger. For $\delta = \pi/2$ the stars cannot merge due to the resulting mirror-symmetry

$$\phi(x,y,z,t) = -\phi(-x,y,z,t) \tag{1.58}$$

and a repulsive force causes them to bounce off each other. This extreme repulsiveness is constrained to the values close to $\delta = \pi/2$: for small values deviating from it, they simply merge [90].

Surprisingly, in [84, 87] none of the simulated binaries formed a rotating Boson star state as described in the previous section; all cases that did not form Black holes seem to converge to a non-rotating state.

Recent work by [91–93] studied the merger of an Axion star with a Black hole or NS. The recent discovery of the first Neutron star merger [94] which has been observed using both electromagnetic and gravitational wave detectors, started the age of multi-messenger astronomy. There are indications that an AS-NS event might be able to mimic a BNS or NSBH merger [92] in certain situations.

post-merger

Later in this thesis, we study the merger of two Oscillatons, which results in another stable Oscilloton for light enough cases. The resulting remnant is highly excited and continuously radiates gravitational waves in a periodic pattern. Due to their relatively large amplitude, they could be a potentially interesting feature for detections. Both of these mergers did not contain any angular momentum, which might change the radiation profile significantly.

1.3 Boson stars as Supermassive Black holes

Unlike Neutrons stars, which due to the Chandrasekhar limit have a maximum mass of $\sim 3\,\mathrm{M}_{\odot}$, ultralight scalar fields could form stable objects with masses comparable to supermassive Black holes (SMBH). This raises the question of whether the assumed Black hole in the centre of the galaxy M87 could potentially be a Boson star. This hypothesis can be tested thanks to the recent efforts of the Event Horizon Telescope [37, 38] and BlackHoleCam [39], which measures millimetre synchrotron radiation from the accretion disc using very-long-baseline interferometry (VLBI) methods. Furthermore, Boson stars are a toy model for any other horizon-free compact objects without hard surfaces.

To understand what a Boson star would look like one has to model the accretion disk in the background spacetime of the Boson star, and then calculate the light rays in reverse through the spacetime and recreate the picture. [15] undertook such a complete study, producing the images in Fig. 1.9. The general-relativistic ideal-magnetohydrodynamic GRMHD simulations showed the formation of a torus in the interior of the Boson star. Due to the angular momentum contained in the plasma, there is very little material in the centre of the scalar Boson star, which reproduces the crescent-like feature seen for Kerr Black holes. This Boson star would not be able to be a Black hole mimicker, because the size of the hole would be too small for the expected mass.

In another study [95], where rotating mini-boson stars where considered, there exist configurations ($k = 1$, $\omega = 0.77$) for which the resulting image is harder to distinguish than in the non-rotating case. However, the accretion disc in the study [95] was not obtained using dynamical evolution, but constructed a priori and kept static.

Another limitation is that these studies only consider a static spacetime. Many Boson stars (e.g. Oscillatons) also introduce a time-dependence of the metric, which might give a transient signal.

In [95, 15, 96], only massive potentials $V(\phi) = \frac{1}{2}m^2|\phi|^2$ were considered, which is only one of potentials studied in literature (see Table 1.3). A larger study of potentials would be needed to provide conclusive information whether Boson stars can be distinguished from SMBH using VLBI methods.

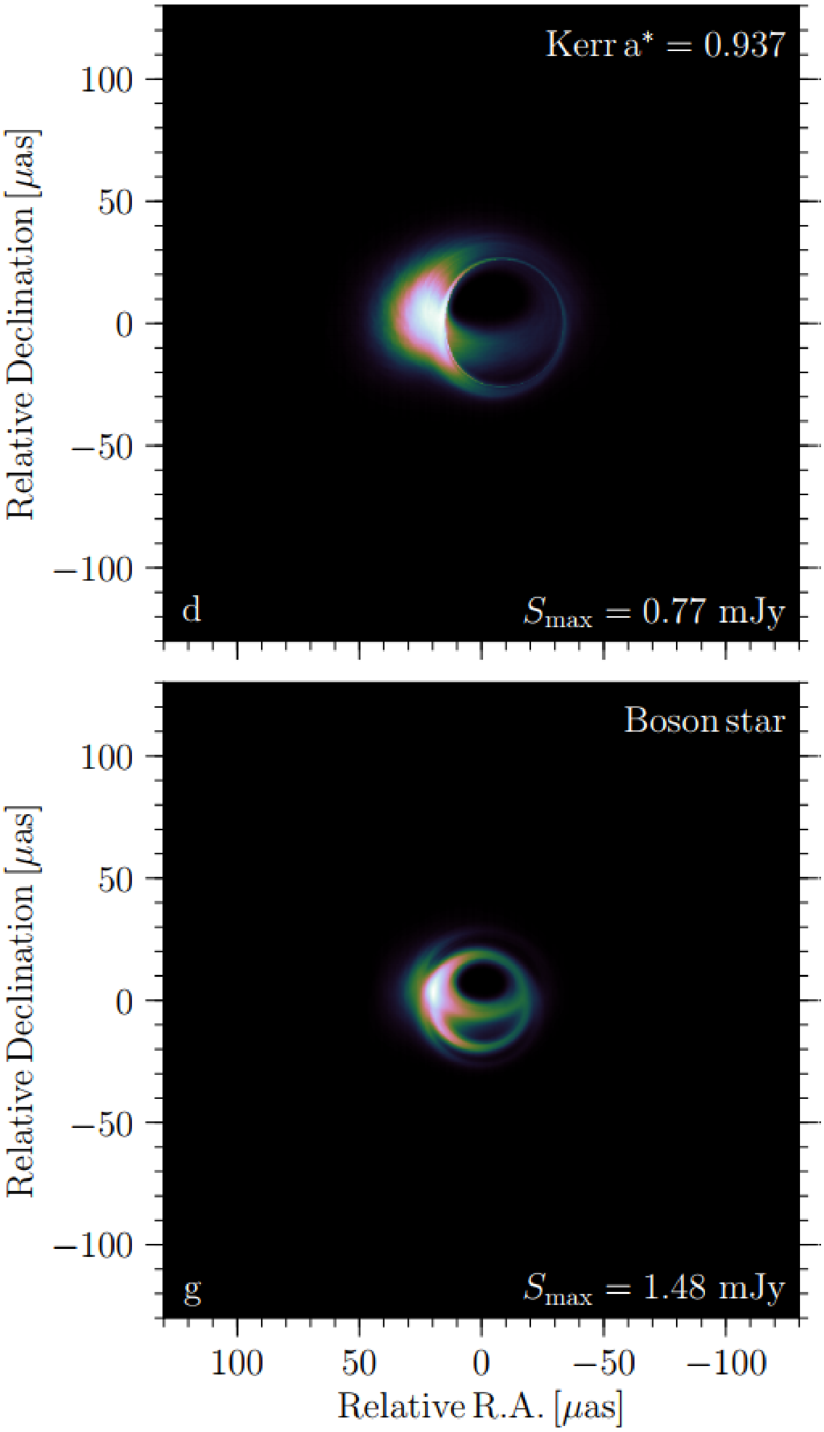

Fig. 1.9 **Comparison between Kerr BH and Boson star :** Simulated raytraced pictures at 230 GHz from electron synchrotron emission of the accrection disc which was obtained by GRMHD simulations. Comparison between the picture of a spinning kerr Black hole and a non-spinning mini-boson star [15].

Chapter 2

Black hole formation from Axion stars

The work presented in this chapter is derived from the paper “Black hole formation from Axion stars” [17], published in the Journal of Cosmology and Astroparticle Physics (JCAP).

The classical equations of motion for an axion with potential $V(\phi) = m_a^2 f_a^2 [1 - \cos(\phi/f_a)]$ possess quasi-stable, localized, oscillating solutions, which we refer to as “Axion stars”. We study, for the first time, collapse of Axion stars numerically using the full non-linear Einstein equations of general relativity and the full non-perturbative cosine potential. We map regions on an “Axion star stability diagram", parameterized by the initial ADM mass, $M_{\rm ADM}$, and axion decay constant, f_a. We identify three regions of the parameter space: *i)* long-lived oscillating Axion star solutions, with a base frequency, m_a, modulated by self-interactions, *ii)* collapse to a BH and *iii)* complete dispersal due to gravitational cooling and interactions. We locate the boundaries of these three regions and an approximate “triple point" $(M_{\rm TP}, f_{\rm TP}) \sim (2.4 M_{pl}^2/m_a, 0.3 M_{pl})$. For f_a below the triple point BH formation proceeds during winding (in the complex $U(1)$ picture) of the axion field near the dispersal phase. This could prevent astrophysical BH formation from Axion stars with $f_a \ll M_{pl}$. For larger $f_a \gtrsim f_{\rm TP}$, BH formation occurs through the stable branch and we estimate the mass ratio of the BH to the stable state at the phase boundary to be $\mathcal{O}(1)$ within numerical uncertainty. We discuss the observational relevance of our findings for Axion stars as BH seeds, which are supermassive in the case of ultralight axions. For the QCD axion, the typical BH mass formed from Axion star collapse is $M_{\rm BH} \sim 3.4 (f_a/0.6 M_{pl})^{1.2} M_\odot$.

2.1 Introduction

The influence of dark matter (DM) can be seen over a vast range of astrophysical scales [97], from super clusters of galaxies with $M \sim 10^{15} M_{\odot}$ (e.g. Ref. [98]), down to the disruption of tidal streams, and contribution to reionization, by substructures with $M \sim 10^{6} M_{\odot}$ (e.g. Ref. [99, 100]), yet the particle nature of DM remains unknown. Theories of DM span an even vaster range of scales, from primordial black holes (BHs), with mass as large as $M_{\rm BH} \sim 10^{2} M_{\odot} \sim 10^{32}$ kg (e.g. Ref. [101]), down to ultra-light axions, with $m_a \sim 10^{-22}$ eV $\sim 10^{-60}$ kg (e.g. Ref. [102]). In the absence of direct detection of DM in the laboratory, the frontiers of our knowledge are pushed back by the gravitational interactions of DM, and its influence on astrophysics.

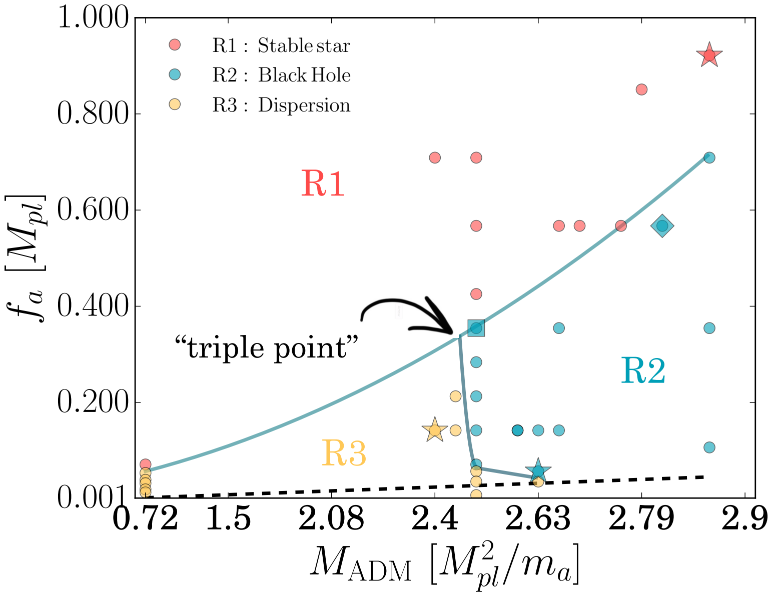

Fig. 2.1 **The Axion star stability diagram**. The stability diagram is parameterized by the axion decay constant, f_a, and the initial condition $M_{\rm ADM}$ (which we set using the initial field velocity, Π, at the centre). Solid lines mark the approximate boundaries between three regions of the Axion star parameter space: quasi-stability (R1), collapse to a BH (R2), and dispersal (R3). We postulate the existence of a "triple point" between these regions. The dashed line marks the region below which axion mass is effectively negligible. Simulated Axion stars are marked as circles; other symbols mark points explored in more detail in Section 2.2. Below the triple point, for $f_a \ll M_{pl}$, under an increase in mass, dispersal of the star via winding of the axion field occurs before collapse to a BH. Above the triple point, stable Axion stars can collapse to BHs by acquiring mass e.g. by accretion.

DM composed of axions (or other scalar fields) can be created non-thermally in the early Universe via the vacuum realignment mechanism. The DM consists of a classical field undergoing coherent oscillations about a quadratic potential minimum [103–106]. Such a model differs from standard cold DM below the scalar field Jeans scale [107]. Below the Jeans scale, DM perturbations are pressure supported by the field gradient energy. In the non-linear regime, the gradient energy supports quasi-stable localised solutions [108–110]. We will refer to these solutions generally as "Axion stars". [1] Axion stars are closely related to the well-known Boson star soliton solutions for a complex field with a conserved global $U(1)$ symmetry [34]. In the present work, we study the gravitational collapse of Axion stars to BHs.

In models of axion DM, Axion stars are expected to be the smallest possible DM structures. Axion stars can form astrophysically either from hierarchical structure formation inside dark matter haloes [111], or are seeded at early times from the large field fluctuations induced by the symmetry breaking leading to axion production [112]. Axion stars can range in mass from $\mathcal{O}(10^{-12}M_{\odot})$ for the QCD axion (e.g. Refs. [113–115]), up to $\mathcal{O}(10^{6}M_{\odot})$ in the cores of DM haloes formed of ultra-light axion-like particles (e.g. Refs. [111, 116, 117, 90, 118–126]).

The strength of the axion self interactions is governed by the "axion decay constant", f_a. It is known that in the $m^2\phi^2$ approximation, which represents the limit $\phi/f_a \ll 1$, Axion stars possess a critical mass [108] beyond which they are unstable: they migrate to the stable branch under perturbations that decrease the total mass, or collapse to BHs under perturbations that increase the total mass [55]. Criticality occurs when $\phi(r=0) \approx 0.48M_{pl}$, where $M_{pl} = 1/\sqrt{8\pi G_N} \approx 2.4 \times 10^{18}$GeV is the reduced Planck mass. The expectation from high-energy physics is that generically $f_a < M_{pl}$.[2] Therefore, Axion stars may exist far from the $m^2\phi^2$ region of the potential, and their stability may be affected by the periodicity and anharmonicity of the axion potential.

As we will discuss, the initial central field velocity of the Axion star, $\Pi(r=0)$, specifies its ADM mass, M_{ADM}, and thus collapse is ultimately determined by the star's mass. In this work we investigate the Axion star solution space parameterized by (M_{ADM}, f_a). For each value of f_a, we scan a range of initial values of ADM mass to identify regions on an "Axion star stability diagram".

---

[1] In the case of a pure $m^2\phi^2$ scalar potential these solutions are known as "oscillatons". In the case of axion DM, they go under various names depending on the mechanism of formation: axion miniclusters, axion drops, solitons etc.

[2] See e.g. Refs. [127–133]. This subject and the related "weak gravity conjecture" are hotly debated at present with relation to axion inflation.

We explore this stability diagram numerically, solving the full non-linear Einstein equations of general relativity (GR) using the numerical GR code GRCHOMBO [134], see Appendix A.2. Numerical GR permits us to evolve regimes in which strong gravity effects play a role without linear approximations. The development of stable numerical formulations (such as BSSN [135, 136], which we use here) and of “moving puncture" gauge conditions (see [8, 6]), have been critical for recent advances in the field. The use of these techniques allows us to stably evolve spacetimes up to and beyond collapse to a BH. The resulting Axion star stability diagram is shown in Fig. 2.1.

We discuss our simulations and main results in Section 2.2. Possible astrophysical consequences of our results are discussed in Section 2.3, and we conclude in Section 2.4. The appendices contain some technical details of the code and simulations, and a brief introduction to axion cosmology and the more familiar non-relativistic Axion stars.

Some movies of simulations from this work can be accessed via the GRCHOMBO website http://www.grchombo.org/.

2.2 Simulating Axion Stars

We simulate Axion stars in numerical GR using GRCHOMBO [134]. Details of our numerical scheme can be found in Appendix A.2 and Appendix A.3. Numerical relativity solves GR as an initial value problem. We simulate points on the two-dimensional axion stability diagram defined by the axion decay constant, f_a (the axion mass is absorbed in the choice of units for length and time), and a one-parameter family of initial conditions specified by the initial ADM mass, M_{ADM}. We begin by defining the problem under consideration and giving the axion potential, with additional details relegated to Appendix A.1. Next we consider an approximation to axion stars that allows for a perturbative stability analysis. We then describe our initial conditions. Next we present our main results concerning the phase diagram, Fig. 2.1. We end with a brief discussion of an interesting transient phenomenon: the “scalar wig”.

Throughout, we simulate axion stars as a solution to the *classical* equations of motion. The semi-classical approximation to Einstein’s equations is

$$G_{\mu\nu} = 8\pi G_N \langle T_{\mu\nu}\rangle_Q \,, \tag{2.1}$$

where $\langle T_{\mu\nu}\rangle_Q$ is the expectation value of the axion energy momentum tensor in some state $|Q\rangle$. Solving the classical equations of motion corresponds to setting $|Q\rangle = |\phi\rangle$. The state

$|\phi\rangle$ is defined such that the expectation value of the field operator (and its correlators) obeys the classical equations of motion, i.e. $\Box\phi_{cl} = 0$ with $\phi_{cl} \equiv \langle\phi|\hat{\phi}|\phi\rangle$. Given explicitly in terms of creation operators $|\phi\rangle$ is (see e.g. Ref. [137]):

$$|\phi\rangle = \mathcal{A}\exp\left[\int \frac{d^3k}{(2\pi^3)}\tilde{\phi}(\vec{k})\hat{a}_k^\dagger\right]|0\rangle\,, \tag{2.2}$$

where $\mathcal{A}$ is a normalization factor.

Our choice of state $|Q\rangle = |\phi\rangle$ is quite different from the state used in e.g. Refs. [108, 138] who take $|Q\rangle = |N,1,0,0\rangle$, i.e. a state of definite particle number N in the ground state in spherical symmetry with principal quantum numbers $n = 1, \ell = m = 0$. The expectation value of $T_{\mu\nu}$ in such a state is time independent, and is not suitable for our purposes of studying dynamics. In the relativistic regime, the real scalar axion field has no conserved particle number, although there is an effective conserved particle number in the non-relativistic limit (see Appendix A.1.1). The state $|\phi\rangle$ represents the thermalized condensate of axions created either by the smoothing of fluctations by inflation in the misalignment mechanism, or by late-time Bose-Einstein condensation due to self interactions [102, 137]. We discuss quantum corrections to our treatment briefly in Section 2.4, but leave a systematic treatment to a future work.

2.2.1 The axion potential

Axions are pseudo-Goldstone bosons of spontaneously broken global $U(1)$ "Peccei-Quinn" (PQ) symmetries [139]. The complex PQ-field, φ, has the potential

$$V(\varphi) = \lambda_\varphi\left(|\varphi|^2 - \frac{f_a^2}{2}\right)^2\,. \tag{2.3}$$

The $U(1)_{\rm PQ}$ symmetry is broken at a scale f_a, which in string theory is expected to be in the range 10^{12} GeV $\lesssim f_a \lesssim M_{pl}$ [140, 128],[3] and for the QCD axion is bounded experimentally to $f_a \gtrsim 10^9$ GeV [142]. After symmetry breaking, writing the PQ field as $\varphi = (\rho/\sqrt{2})e^{i\phi/f_a}$, the radial field ρ acquires a vacuum expectation value such that: $\langle\varphi\rangle = (f_a/\sqrt{2})e^{i\phi/f_a}$. The angular degree of freedom, the axion ϕ, is the Goldstone boson of the broken symmetry.

As a Goldstone boson, the axion enjoys a shift symmetry, i.e. the action contains only terms in $\partial_\mu\phi$ and there is a symmetry under $\phi \to \phi + c$ for any real number c. In general, this shift symmetry is anomalous, and is broken to a discrete symmetry, $\phi \to \phi + 2\pi n$ for some integer n. In the case of QCD this occurs thanks to the chiral anomaly if there are quarks charged under the chiral $U(1)_{\rm PQ}$ symmetry. In a general model, quantum gravity effects are expected to break all continuous global symmetries.[4] In practice in string theory, this occurs due to the presence of instantons and other non-perturbative effects [128].

---

[3] This ignores alignment [141, 131] and assumes soft SUSY masses are above about 1 TeV.

The breaking of the axion shift symmetry selects a particular direction in the field space $\varphi = \varphi_1 + i\varphi_2$. In the potential we can write this as:

$$V(\varphi) = \lambda_\varphi \left(|\varphi|^2 - \frac{f_a^2}{2}\right)^2 + \varepsilon\varphi_1 \,, \tag{2.4}$$

for some parameter ε of mass dimension three, which is "small" in the sense that $\varepsilon/f_a^3 \ll 1$. In some limits, as we will discuss in the following, we can ignore the radial mode and consider simply a periodic potential for the axion:[5]

$$V(\phi) = \Lambda_a^4 \left[1 - \cos\left(\frac{\phi}{f_a}\right)\right] \equiv m_a^2 f_a^2 \left[1 - \cos\left(\frac{\phi}{f_a}\right)\right] , \tag{2.5}$$

and we find that $\varepsilon = \sqrt{2}m_a^2 f_a$. The minimum of the potential at $\phi = 0$ (and not the local curvature of the potential) defines the "axion mass",[6] $m_a = \Lambda_a^2/f_a$. Since non-perturbative effects generally switch on at scales far below the fundamental scale, while we expect f_a to be of order the fundamental scale, axions are naturally extremely light via the seesaw mechanism as long as the shift symmetry breaking is small: $\varepsilon/f_a^3 = \sqrt{2}(m_a/f_a)^2 \ll 1$. The axion is also hierarchically lighter than the radial field, ρ.

Due to the hierarchy of scales between the axion mass and the radial mode, in this work we simulate the axion field as real valued in the cosine potential. A discussion of simulations using the full complex PQ field, versus the real-valued axion field, is contained in Appendix A.3.2, where we also discuss the stability of the radial mode.

Given that we are modelling the periodic potential and allowing the field to go over the maximum at $\phi = \pi f_a$, it is possible to imagine situations where two adjacent regions in space have the same field value in the corresponding full $U(1)$ potential – with each 2π traversed in the periodic potential corresponding to a winding of the $U(1)$ vacuum manifold. This can lead to the formation of closed global strings – our fixed boundary conditions with $\phi = 0$ imply that the total winding number must be conserved and since our initial configuration has zero winding number, only closed strings can form.

---

[4] This is thanks to the BH no-hair theorems [143], the existence of wormholes [144, 145], and the exchange of Planck-scale BHs in gravitational scattering. In the standard model, for example, this allows for violation of Baryon number suppressed by powers of M_{pl} [146]. For discussion relating to the QCD axion, see e.g. Ref. [147].

[5] The cosine potential is the canonical, and simplest, axion potential. Note, however, that for the QCD axion there are corrections to the chiral Lagrangian that steepen the potential slightly away from the $\phi = 0$ (e.g. Ref. [148]).

[6] Of course, the local curvature defines the instantaneous mass, and all the dynamics. The definition here is just a useful parameterization that we use to choose units.

Energetically, as long as ϕ can traverse more than 2π (which indeed happens in our simulations) such closed strings can form. Nevertheless, the spherical symmetry of our initial conditions (and hence of the subsequent evolution) means that topologically it will be unlikely that closed strings (which are topologically tori) can form. It would be interesting to imagine situations where this is not the case, where loops of string could be produced in objects with less symmetric initial conditions such as that of two colliding Axion stars.

In addition to strings, the axion potential can support the presence of domain walls.[7] The many "minima" of the axion potential $V(\phi) = \Lambda_a^4[1 - \cos(\phi/f_a)]$ correspond to a single minimum in the complex broken $U(1)$ potential. In the periodic potential picture, domain walls form when neighbouring regions fall into different minima – in the $U(1)$ picture these domain walls corresponds to the twisting of the argument of the complex field φ (which carries energy since the $U(1)$ symmetry is broken). In the simple model when there is only a single minimum in the $U(1)$ potential, the formation of a domain wall is a necessary but insufficient condition for the formation of a closed string.

In variants of the axion model (in particular the DFSZ axion in QCD) anomaly factors lead to more than one distinct minimum within the $U(1)$ vacuum manifold. In this case, domain walls can form even if the argument of φ twists less than 2π. We leave consideration of such cases to a future work. As long as the radial mode is stable and the boundary conditions fixed, all considerations of domain walls and strings are captured by the evolution of the real field in the cosine potential. Operationally, to interpret the results in terms of the full $U(1)$ potential, one simply applies the appropriate surjective map from $\mathbb{R}^1$ to S^1.

2.2.2 Perturbative Analysis of Axion Stars Solutions

In this section, we investigate the stability of the Axion stars in the relativistic, but weak gravity, regime with small self-interactions.[8] Our goal is to show that the presence of higher order terms in the potential generates a long wavelength modulation of the oscillaton. As we will see below, since we will be working on the super long wavelength limit, this is not a full stability analysis (which we will undertake in a separate work). For a stability analysis of Boson stars in the limit with no higher order terms in the potential, see [149].

---

[7] Again the fixed boundary conditions imply that the global solitonic charge of the domain walls must be conserved, and hence equal to zero at all times.

[8] The non-relativistic limit including gravity but with no self-interactions is discussed briefly in Appendix A.1.1.

In the limit of small angles, we can expand the potential Eq. (2.5) in orders of (ϕ/f_a) as follows

$$\begin{aligned} V(\phi) &= m_a^2 f_a^2 \left[1 - \cos\left(\frac{\phi}{f_a}\right)\right] \\ &= \frac{1}{2} m_a^2 \phi^2 - \frac{1}{4!} \frac{m_a^2 \phi^4}{f_a^2} + \dots \end{aligned} \tag{2.6}$$

with the subsequent equation of motion for the scalar field

$$\Box\phi - m_a^2 \phi + \frac{1}{6} \frac{m_a^2 \phi^3}{f_a^2} = 0 \,. \tag{2.7}$$

Consider the perturbative expansion

$$\phi = \bar{\phi} + \delta\phi \tag{2.8}$$

and inserting this back into Eq.(2.7) we obtain the zeroth order equation of motion

$$\Box\bar{\phi} - m_a^2 \bar{\phi} + \frac{1}{6} \frac{m_a^2 \bar{\phi}^3}{f_a^2} = 0 \,. \tag{2.9}$$

In spherically symmetric coordinates, we can expand the d'Alembertian as follows

$$\Box\bar{\phi} = -\ddot{\bar{\phi}} + \frac{2}{r}\frac{\partial\bar{\phi}}{\partial r} + \frac{\partial^2 \bar{\phi}}{\partial r^2} + \text{gravity terms} \,. \tag{2.10}$$

Consider the motion of the field at the origin $r = 0$, and write $\bar{\phi}(r = 0) = \bar{\phi}_0$. Regularity at the origin imposes the condition $\partial\bar{\phi}_0/\partial r = 0$. Furthermore, consider the limit where gravity is subdominant, i.e. where $M_{\mathrm{ADM}} \lesssim \mathcal{O}(0.1)$, so we can ignore the gravity terms. Finally, the gradient term

$$\frac{\partial^2 \bar{\phi}}{\partial r^2} \sim k^2 \bar{\phi} \,, \tag{2.11}$$

where k^{-1} is roughly the characteristic size of the Axion star. For a generic Axion star, $k \ll \omega$ where ω is the characteristic frequency of the axion, and hence we also neglect this term at low orders [150, 151].

After making all these assumptions, the partial differential equation Eq. (2.9) is reduced into an ordinary differential equation

$$\ddot{\bar{\phi}}_0 + m_a^2 \bar{\phi}_0 \left(1 - \frac{1}{6}\frac{\bar{\phi}_0^2}{f_a^2}\right) = 0\,. \tag{2.12}$$

In the small angle limit, $f_a^2 \gg (1/6)|\bar{\phi}_0|^2$, so $\bar{\phi}_0$ has an oscillatory solution

$$\bar{\phi}_0(t) = A\cos\omega_1 t\,, \tag{2.13}$$

where $\omega_1 \approx m_a\sqrt{1-(1/6)(A/f_a)^2} \approx m_a$. At second order in $1/f_a^2$, we obtain the Mathieu equation for $\delta\phi$

$$\frac{d^2}{d\tau^2}\delta\phi + (a - 2q\cos 2\tau)\delta\phi = 0\,, \tag{2.14}$$

where we have rescaled time $\tau = t/\omega_1$ and

$$a = \frac{m_a^2}{\omega_1^2}\left(1 - \frac{1}{4}\left(\frac{A}{f_a}\right)^2\right)\ ,\ q = \frac{m_a^2}{8\omega_1^2}\left(\frac{A}{f_a}\right)^2\,. \tag{2.15}$$

In the small angle approximation, $A/f_a \ll 1$, an approximate solution is

$$\delta\phi \propto \cos\omega_2 t\ ,\ \omega_2 = \omega_1\sqrt{a} \lessapprox \omega_1\,. \tag{2.16}$$

The last inequality on the frequencies implies that the total solution, $\bar{\phi} + \delta\phi$, at $r = 0$:

$$\phi(t, r=0) \approx C_m \cos\left(\frac{\omega_1+\omega_2}{2}t\right)\cos\left(\frac{\omega_1-\omega_2}{2}t\right)\,, \tag{2.17}$$

(where C_m is a constant), is a modulation of the short wavelength frequency $(\omega_1+\omega_2)/2 \approx \omega_1$ with a long wavelength $(\omega_1-\omega_2)/2$ frequency. We observe such a modulation in our numerical solutions (Section 2.2.4).

Note that since we have dropped the gradient terms in this analysis – and hence consider only the long wavelength limit of the true solution, it would be treacherous to analyze this result further using a Floquet type stability analysis [152, 153]. We leave a more detailed analysis to a future work.

2.2.3 Initial Conditions

In this section we construct initial conditions for our Axion star. These are based on the solutions for oscillatons in an $m^2\phi^2$ potential, for which the full solutions in space and time are known (that is, they have been obtained semi-analytically, see Refs. [55, 67, 56]). Since the axion potential is more complex, the oscillaton profiles for the field and metric components will not, in general, satisfy our axion constraint equations. The exception is the time instant at which $\phi(r)$ is zero everywhere, since $V(\phi = 0) = 0$ in either the $m^2\phi^2$ or cosine potential. Thus, since the Hamiltonian constraint will contain the same value of ρ, the same field and metric profiles will be a solution in either case. It is this instantaneous solution which is chosen as the initial condition for our Axion star.

Since we choose initial conditions for which $\phi(r)$ is zero everywhere on the initial hypersurface, all information is contained in the profile for the field velocity $\Pi = \dot{\phi}/\alpha$ (where α is the lapse function in the ADM decomposition of GR, see Appendix A.2). Whilst the field data is not time symmetric (the field profile is moving "up"), the momentum constraint is still trivially satisfied by setting the extrinsic curvature $K_{ij} = 0$ due to the fact that the momentum density S^i is instantaneously zero. The Hamiltonian constraint is then solved using a Fourier method, which is described in Appendix A.1.2.

Since we assume that the initial radial profile for $\Pi(r)$ is that of an oscillaton, we can define a one parameter family by the initial value of $\Pi(r = 0)$. The ADM masses of the the profiles are fixed by $\Pi(r = 0)$, and so M_{ADM} can be used as an alternative (and perhaps more intuitive) variable for our initial conditions on the stability diagram. Thus, for a given value of f_a, the initial conditions of our Axion stars are then specified entirely by the value of M_{ADM}, giving our two dimensional solution space.

Although $\phi = 0$ everywhere on the initial hypersurface for our solutions, we refer to them as "Axion stars" because of their formal construction from the compact quasi-stable solutions in the $m^2\phi^2$ theory.

The radial profiles of $\Pi(t = t_i)$ are illustrated in Fig. 2.2. The solutions with larger M_{ADM} have larger central field velocity, and are more compact radially. The larger field velocity implies that the axion field will travel further up the potential, and will feel more of the effect of the self-interactions. Note that the radii of these stars are bigger than their Schwarzchild radii so any collapse into a Black hole is purely driven by its dynamics.

Our chosen one-parameter family of initial conditions does not, of course, cover the most general possible initial conditions for an Axion star in spherical symmetry – in theory one could choose to evolve any perturbation in the field, with any radial spread and velocity profile. There are no restrictions in the code requiring specific initial conditions, except that

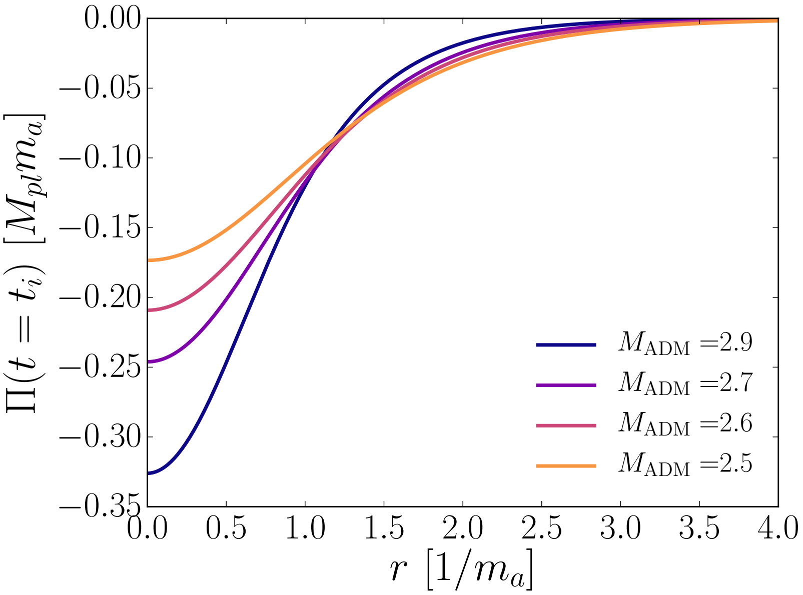

Fig. 2.2 **Initial Conditions.** We show our initial conditions, where ϕ is zero everywhere and the conjugate momentum of the field Π contains all the information about the solution. This solution for Π is correct for any value of f_a in the full cosine potential, since $V(\phi = 0) = 0$ for all f_a and the Hamiltonian constraint is satisfied. Therefore, we can use these $\Pi(t_i)$ profiles, which we parameterize according to their ADM mass using Fig. A.1, to define our one-parameter family of initial conditions for Axion stars. The ADM mass is measured in units of M_{pl}^2/m_a.

they must satisfy the Hamiltonian and Momentum constraints of GR. However, our initial conditions provide a useful reduction of the solution space of Axion stars for this study. We also consider them well motivated astrophysically by their relation to the non-relativistic Axion stars expected to form in DM halos.

2.2.4 Three phases of Axion stars

Having calculated the initial conditions, we evolved a range of models parameterized by (M_{ADM}, f_a), as shown in Fig. 2.1. The solution space is divided into three regions:

- **Region 1 (stable)**: Where the maximum axion angle $\phi/f_a \lesssim 0.1\pi$, we find quasi-stable solutions for which the lifetime is much longer than the individual oscillations of the field profile. These solutions differ from the $m^2\phi^2$ model by small modulations and are true Axion stars (see Fig. 2.3).

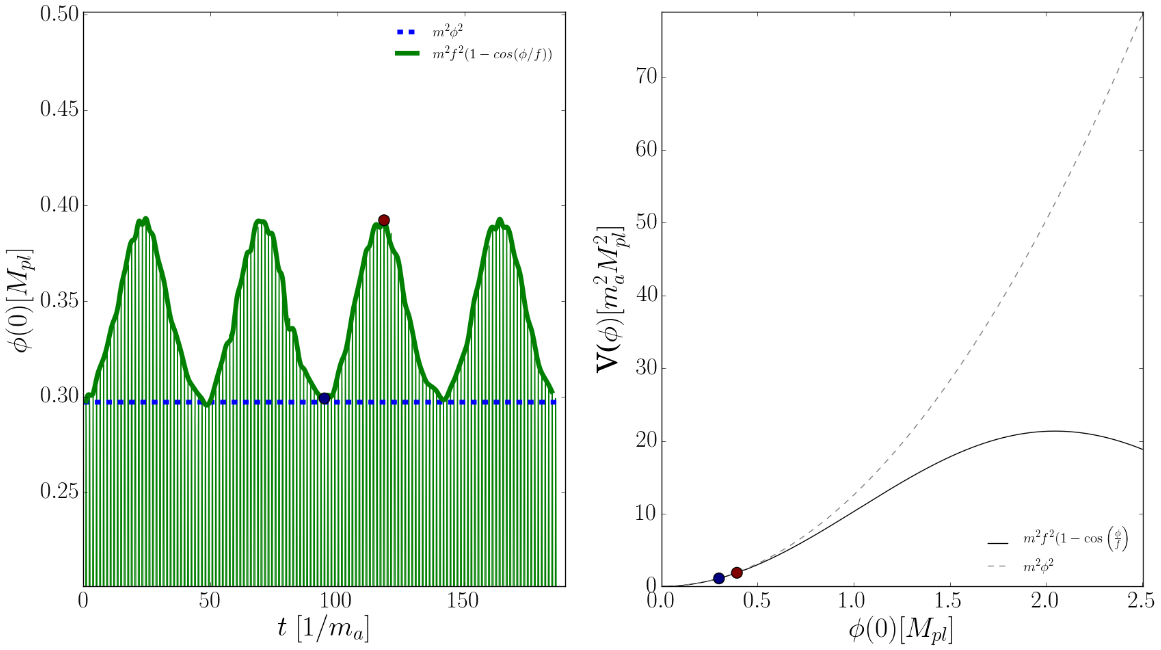

Fig. 2.3 **Stable Axion stars.** $(M_{\rm ADM}, f_a) = (2.86, 0.92)$, R1 star in Fig. 2.1. *Left panel*: The evolution of the central field value, $\phi(r=0)$, over time of a stable Axion star, compared to that of an oscillaton (i.e. pure $m_a^2\phi^2$). Stability is shown over many periods of oscillation. The existence of two frequencies in this solution can be understood qualitatively from the perturbative analysis in Section 2.2.2. *Right panel*: comparison of the potential for an $m_a^2\phi^2$ oscillaton (dashed) and the cosine Axion star (solid). The two marked points correspond to times in the evolution of the Axion star shown in the left panel.

- **Region 2 (unstable)**: Where the initial ADM mass is sufficiently large, we find collapse to black holes (see Figs. 2.4 and 2.5) even though the stars' radii are greater than their respective Schwarzchild radii.
- **Region 3 (unstable)**: Where f_a is small (large self-interactions) and the initial field velocity is sufficiently large, we see dispersal of the Axion star caused by scalar radiation (see Figs. 2.6 and 2.7).

There are various competing physical factors which determine the evolution of the Axion stars in each part of the solution space. Gravity, in the form of the total Axion star mass, tends to lead to collapse. An opposing factor is the gradient pressure, which tends to support the star against collapse (the familiar axion Jeans scale in linear theory). Thus if the profile of the Axion star grows narrower, or if the field makes excursions over a large distance in field space, this tends to make the field “bounce back" to a flatter configuration.

The interplay between gravity and gradient energy results in the interesting quasi-stable Axion star configurations of Region 1, with a boundary separating it from the unstable Regions 2 and 3. This division of the solution space into stable and unstable regions can be understood qualitatively by extending the calculations in Section 2.2.2 to a more advanced stability analysis. However, we found that an adequate quantitative understanding (e.g. predicting the slope of the boundary between stability and inability) cannot be achieved by such methods. The endpoint of the instability: collapse in Region 2, or dispersal in Region 3, is determined by dynamics. These three fates have also been observed in different cases (see Ref. [45]).

In the case of stable Axion stars in Region 1, they remain in phase, i.e. the angular velocity of the ϕ field remains coherent. This, combined with the fixed boundary at infinity, necessitates that the traverse of ϕ is larger in the center of the star than at its periphery – a behaviour which is also exhibited by flat space oscillons in a periodic potential [154]. Intuitively, one can understand the tendency for the Axion stars to stay in phase by noting that any deviation creating an off phase configuration radially will result in an increase in the total gradient energy. Hence, roughly speaking, one can say that the in-phase configuration is a “low energy configuration” (i.e. excess energy will be radiated away quickly).

A closer look at the evolution of the central axion field value in a Region 1 stable Axion star is shown in Fig. 2.3. The evolution shows two distinct frequencies: a high frequency close to that of the $m^2\phi^2$ theory, and a low, modulating frequency. This behaviour can be understood qualitatively in terms of the perturbative analysis in Section 2.2.2, though we were not able to quantitatively reproduce the exact frequency ratio via this simplified calculation. In addition to the dynamics of the central point, conservation of energy implies that this “breathing” must be accompanied by corresponding modulation of the characteristic size of the Axion star, which we also observe in our numerical simulations . While this observation of modulating, stable Axion star solutions in full numerical GR is a new result of the present work, this effect is also first alluded to in Ref. [154] in simulations without gravitational backreaction.

In the unstable region of the solution space, Region 2, BH formation occurs. This is demonstrated in Figs. 2.4 and 2.5, for BH formation near the “triple point” and near the dispersal region respectively.

Fig. 2.4 shows the central field evolution over time, the radial profile of the metric lapse, α, at various time slices, and the journey of the field over the potential. At this point, BH formation is occurring near the boundary between the stable and unstable regions. The instability is monotonic, in the sense that the amplitude of the central field value oscillations always grows over time. In the so-called “moving puncture gauge” which we employ in our simulations [155], the lapse is driven to zero in regions of high curvature, hence a good indication of BH formation is that the central value of the lapse approaches zero. In this simulation, the field amplitude grows significantly, reaching the top of the potential “hill" before collapse. It thus feels the full anharmonicity of the potential. This shows that BH formation from Axion stars, even near the stable region, involves the full cosine potential and self-interactions.

A qualitative picture of BH formation near the dispersing region is shown in the contour plots of Fig. 2.5, which show the conformal metric factor, χ (as defined and described in Appendix A.3). Large gradients in χ indicate strongly curved space, and a collapse to zero at some point is usually indicative of a BH having formed. We use a horizon finder to locate the approximate trapped surface of the ensuing black hole (see Fig. 2.5), from which we can obtain a lower bound on the final BH mass. In the case of BH formation near the dispersing region, ejection of matter during collapse is important.

This ejection of matter via scalar radiation, sometimes known as “gravitational cooling” [109], is the third important factor at play for Axion stars, and the most important factor in Region 3. If the Axion star mass is small, and the initial field velocity is large, gradient pressure prevents collapse and the continuous ejection of shells of matter will gradually disperse the star.

We illustrate dispersal in Region 3 qualitatively in Fig. 2.6 with contour plots at fixed time slices, and more quantitatively in Fig. 2.7 where we show the time evolution of the field and conformal metric factor at the origin. Dispersal of the Axion star in Region 3 is indicated most clearly by the time evolution of the metric conformal factor at the origin, $\chi(0)$. As detailed in Appendix A.3, for weak field gravity the conformal factor is approximately related to the Newtonian gravitational potential V_{Newton} by:

$$\chi = \sqrt{\frac{1}{1-2V_{Newton}}}, \tag{2.18}$$

Thus as χ decreases below 1, this corresponds to a negative potential into which the field initially infalls. Later, matter ejection takes over when χ is driven to $\chi > 1$, indicating that the Newtonian potential is positive and the Axion star is dispersing. The intervening oscillations are the result of shells of matter collapsing and then being “blown off" during the gravitational cooling. Eventually, when all the material has dispersed, it will settle back to $\chi \approx 1$, corresponding to flat space and the absence of a gravitational potential.

A qualitatively new feature in Region 3 is seen by inspecting the evolution of the central value of the axion field, $\phi(0)$. The initial field velocity in Region 3 is large, and the central axion field value undergoes winding in the $U(1)$ vacuum manifold, oscillating around zero with an almost fixed period and decaying amplitude. In the cosine potential, this is seen as the field moving "over the top" of the potential hills. Like a wound-up spring, after the field goes over the top a number of times, it unwinds and returns to negative values. This unwinding is symmetric and the field always oscillates about $\phi = 0$, never getting trapped in one of the other minima, due to the boundary conditions on the field, which impose conserved zero winding number.

Given that we have identified three distinct regions of Axion stars, and mapped some of the structure of the solution space, it is evident that there must exist a *"triple point"*, where dispersal, collapse, and stability co-exist. We can estimate the approximate location of the triple point:

$$M_{\rm TP} \sim 2.4 \frac{M_{pl}^2}{m_a}\,, \tag{2.19}$$

$$f_{\rm TP} \sim 0.3 M_{pl}\,. \tag{2.20}$$

The existence of the triple point has the interesting consequence that for $f_a < f_{\rm TP}$, increasing the mass of a stable Axion star will move it into the dispersal region before moving into the BH region. This suggests that BH formation from stable Axion stars may be impossible for $f_a < f_{\rm TP}$ (barring violent, non-adiabatic processes leading to a rapid increase in mass).

2.2.5 "Scalar Wigs"

We noted in the simulations that following BH formation, the residual axion field outside the horizon settled into semi-stable configurations. These are shown in Fig. 2.8, where we plot the scalar field value near the horizon at $r = 6/m_a$ from the time at which the apparent horizon forms. These configurations appear to be similar to the "scalar wigs" described in Refs. [156–159]. It is likely that eventually these wigs will partly fall into the black hole, and thus increase its final mass, and partly disperse to infinity. This is evident in Fig. 2.8 where we notice the scalar amplitude oscillate and decay. We did not investigate these structures and their stability in great detail, as the timescales involved would have required much longer runs and significant computational resources, and reflections from our computational boundary could become problematic. We leave further study of scalar wigs formed from gravitational collapse of Axion stars to future work.

2.3 Observational Consequences

2.3.1 BH – Axion star mass relation

We simulated the formation of a BH from an Axion star close to the boundary separating regions R1 and R2: $(M_{\rm ADM}, f_a) = (2.81, 0.57)$, shown as the R2 diamond in Fig. 2.1. We found that the final BH mass in this case was:

$$M_{\rm BH} = (2.80 \pm 0.03)\frac{M_{pl}^2}{m_a}, \tag{2.21}$$

where the error arises from the limited numerical resolution, with additional error of up to 0.1% due to reflections of outgoing scalar waves. Thus, within the errors of our simulation, almost all of the mass of a stable Axion star above the “triple point” could be expected to form a BH if it accretes mass and moves over the phase boundary. We point out that almost all of the initial mass gets absorbed into the BH.

Above the “triple point” the line separating stable Axion stars from BHs scales with f_a as $M_{\rm stable} \sim f_a^p$, with $p \approx 0.2$ fit from the points on the line separating R1 and R2 in Fig. 2.1. Converting to astrophysical units, the typical BH mass formed from collapse of initially stable Axion stars is thus of order:

$$\begin{aligned} M_{\rm BH} &\sim 1.4 \times 10^7 \left(\frac{10^{-18}\ {\rm eV}}{m_a}\right)\left(\frac{f_a}{0.6M_{\rm pl}}\right)^{0.2} M_\odot\,, \\ &(f_a \gtrsim 0.3M_{pl})\,. \end{aligned} \tag{2.22}$$

Plugging in the relation $m_a \approx 6\,\mu{\rm eV}(10^{12}\ {\rm GeV}/f_a)$ for the QCD axion [160, 161] yields:

$$M_{\rm BH,QCD} \sim 3.4(f_a/0.6M_{pl})^{1.2} M_\odot\,. \tag{2.23}$$

That this is of the order of the BH mass relevant for superradiance for the QCD axion [162] is not entirely a coincidence, since in both cases one is equating the two length scales of Compton wavelength and Schwarzschild radius. Superradiance is absent in our simulations due to the spherical symmetry. We note that observations of spinning solar mass BHs exclude 3×10^{17} GeV $< f_a < 1 \times 10^{19}$ GeV QCD axions [163], which excludes $f_a \sim f_{\rm TP}$, though super-Planckian QCD axions are allowed. It will be interesting in future to study the interplay of BH formation and superradiance in systems with angular momentum, such as Axion star binaries.

We emphasize that the relationship Eq. (2.22) is approximate, and only holds in the small region of the solution space that we have studied. We further emphasize the conjectural nature of our division of the phase space, and that this work does not constitute a study of criticality of Axion stars.

2.3.2 Axion stars as seeds of SMBHs?

In models with Axions as dark matter and ordinary, almost scale invariant, adiabatic initial conditions with scalar amplitude $A_s \approx 2 \times 10^{-9}$ normalized by the CMB (case I in Appendix A.1.3), galaxies are expected to host Axion stars at their cores [111] (for sufficiently low Axion mass such that the Axion stars are large and not disrupted by repeated mergers). Galaxy formation is non-relativistic, and the simulations of Ref. [116] found that the Axion star-halo mass relation is given by:[9]

$$M_\star = \eta(z) \left(\frac{M_h}{M_{\text{min.}}} \right)^{1/3} M_{\text{min.}} \,, \tag{2.24}$$

where $M_{\text{min.}} \sim 40 M_\odot (m_a/10^{-18}\ \text{eV})^{-3/2}$ and $\eta(z)$ is a redshift dependent function that can be found in Ref. [116] (the details needn't concern us here). If the Axion star mass in a given halo exceeds the critical mass for BH formation, the galaxy should instead host a BH formed by collapse of the Axion star, if $f_a > f_{\text{TP}}$.

The above mechanism provides a potential origin for a seed population of super massive BHs (SMBHs).[10] SMBHs provide the engines powering active galactic nuclei (AGN) and quasars at high redshift, $z \approx 6$, which require $M_{\text{BH}} \approx 10^9 M_\odot$. Such a SMBH can grow at the Eddington rate from a seed mass of around $M_{\text{seed}} \approx 10^4 M_\odot$ if it was formed when the Universe was approximately 0.5×10^9 years old. Modelling the evolution of a population of BHs is a complex astrophysical problem, and we will make no attempt here to address the issue in any detail, but simply point out this interesting possibility. Ref. [116] have also suggested that the presence of an Axion star core may provide a favourable environment for SMBH formation.

The formation of SMBH seeds from direct collapse of an Axion star in the centre of a DM halo, assuming 100% BH formation efficiency above the critical mass, is similar in spirit to SMBH seed models based on gas-dynamical processes [164]. These processes can, e.g. via rotational support and angular momentum shedding, lead to the formation of very massive stars of $10^4 M_\odot$ if the accumulation of gas proceeds correctly. Such an isolated star will collapse into a massive seed Kerr BH [165].

---

[9] Note that this relation is empirical, and was not recovered in similar simulations in Ref. [90]. The origins and applicability of the scaling relation thus remains unclear.

[10] For a review, see Ref. [164].

On the other hand, the formation of SMBH seeds from collapse of an Axion star is quite different to the mechanism of "Dark Stars" in WIMP models with large annihilation rates [166–171]. Dark Stars provide a route to form objects of $\sim 10^3 M_\odot$ at much earlier times around 10^6 years, falling in the category of SMBH seeds from Pop-III remnants [164].

2.3.3 BHs from axion miniclusters?

Axion "miniclusters" [112] can form from strong perturbations in the axion field caused if PQ-symmetry breaking occurs after inflation (case II in Appendix A.1.3). Miniclusters, if present, would form the first generation of Axion stars at very early times around matter radiation equality. Miniclusters provide a different route to Axion star formation than the hierarchical formation discussed above.

The bound on the tensor-to-scalar ratio in the CMB, $r_T < 0.12$ [172], implies that miniclusters can only form the first generation of Axion stars if $f_a < 1.4 \times 10^{13}$ GeV $\ll f_{\rm TP}$. This value of f_a is far below the "triple point" we postulate in the Axion star stability diagram. *It is thus highly unlikely that axion miniclusters can collapse to form BHs.* Instead, as their mass is increased and winding of the axion field begins they will first cross from the stable to the dispersing region of the phase diagram; they will then lose mass due to scalar radiation before returning to the stable regime.

We postulate that this sets a maximum axion minicluster mass given by the boundary between the stable and dispersing phases at $f_a < f_{\rm TP}$. Strong perturbations to the stable phase may allow for collapse to BHs [55], but this is unlikely in astrophysical environments where accretion is a very slow process compared to the dynamical timescale, m_a.

2.3.4 Quantum Effects and Axion Emission

Our analysis makes no attempt to capture any truly quantum effects, which could change the state, $|\phi\rangle$ in Eq. (2.2) by the production of individual highly relativistic axions. There is a considerable body of work considering quantum effects for Axion stars and how well such effects are captured in the classical field theory: a non-exhaustive list of such works includes Refs. [173–175, 137, 151, 176–179].

Our analysis has been entirely classical in the sense that we have solved the classical field equations under the assumption that the occupation number of the axion field is much greater than unity. We leave the assessment of quantum effects in our analysis to a future work, but note that the dominant effects on the time scales considered should be captured in the classical theory. By considering the axion decays in e.g. Ref. [162] and the analogous process for gravity wave/graviton production in Ref. [180] (see also Ref. [181] for the axion maser effect when a canonical photon coupling is included), it is clear that a classical treatment captures, on simulation time scales, the large number limit of tree-level axion production processes when the grid resolution is small enough to resolve the produced relativistic modes (our maximum mesh refinement gives a resolution of relativistic modes up to $k \approx 2^7 m_a$).

2.4 Conclusions

For the first time, Axion stars in full numerical relativity using GRChombo with the non-perturbative instanton potential, $V(\phi) = m_a^2 f_a^2[1-\cos(\phi/f_a)]$. We studied the solution space, Fig. 2.1, parameterized by the axion decay constant, f_a, and the initial ADM mass, M_{ADM}, of a one parameter family of initial conditions. Our initial conditions are based on the quasi-stable $m^2\phi^2$ solutions known as oscillatons, and are specified in terms of a radial profile for the field velocity, $\Pi(r)$, with $\phi = 0$ everywhere such that the Hamiltonian constraint is satisfied in the interacting cosine potential.

We identified three distinct regions of the solution space: a (quasi-)stable region of true axion stars; an unstable region where the initial axion star collapses to a BH; an unstable region where the initial axion star disperses via scalar radiation. The stable axion stars are new solutions, and differ from oscillatons by the presence of a second modulating frequency in the solution. The existence of the second frequency can be understood from a perturbative analysis, as can the qualitative feature that the solution space is separated into stable and unstable regions depending on the value of f_a.

BH formation via increase of M_{ADM} from the stable branch can only be achieved above the “triple point" separating the three phases, $f_a > f_{\mathrm{TP}} \approx 0.3 M_{pl}$. This could have astrophysical consequences for axion stars as seeds for supermassive BHs. The existence of the dispersing region separating the stable region from BH formation when $f_a < f_{\mathrm{TP}}$ would appear to prohibit BH formation via slow accretion of mass onto axion miniclusters.

For each value of f_a, as we scan the initial values of ADM mass, we expect within some range to see behaviour akin to that observed in critical collapse ([182], for a review see [183]). That is, just above some critical value of M_{ADM}, the star will collapse and form a BH, with a universal scaling relation between the masses. In the present work we do not seek to investigate the criticality of the solutions – that is, we do not seek to demonstrate a universal scaling relation in the final masses of black holes which occur near the critical point – since we are for the moment interested in the overall solution space. However, based on previous studies of massive scalar field collapse in Ref. [184], we would expect type II behaviour similar to that found in the massless case (e.g. in [182]) where the mass of the axion is negligible in comparison to the initial ADM mass of the star (that is, in the bottom right of our phase space, below the dashed line). In this case the mass of the critical BH formed would be zero. We may also expect to observe type I behaviour for larger values of f_a, in which case the black hole formed at the transition point has a finite mass. This appears consistent with our findings, although we have not investigated sufficiently close to the critical point to confirm it.

Various authors have studied collisions of oscillatons in the $m^2\phi^2$ potential and Boson stars, see Ref. [86] in the relativistic case, and Refs. [185, 186, 116, 90, 187, 188] in the non-relativistic case. Studying collisions of axion stars, and in particular whether colliding stable axion stars can cause BH formation, is left to future work. The full 3+1 dimensional solutions possible with GRCHOMBO will allow us to study non-spherically symmetric axion stars with angular momenta, and axion star binaries, with possible applications to experimental searches for gravitational waves with LIGO [5, 189].

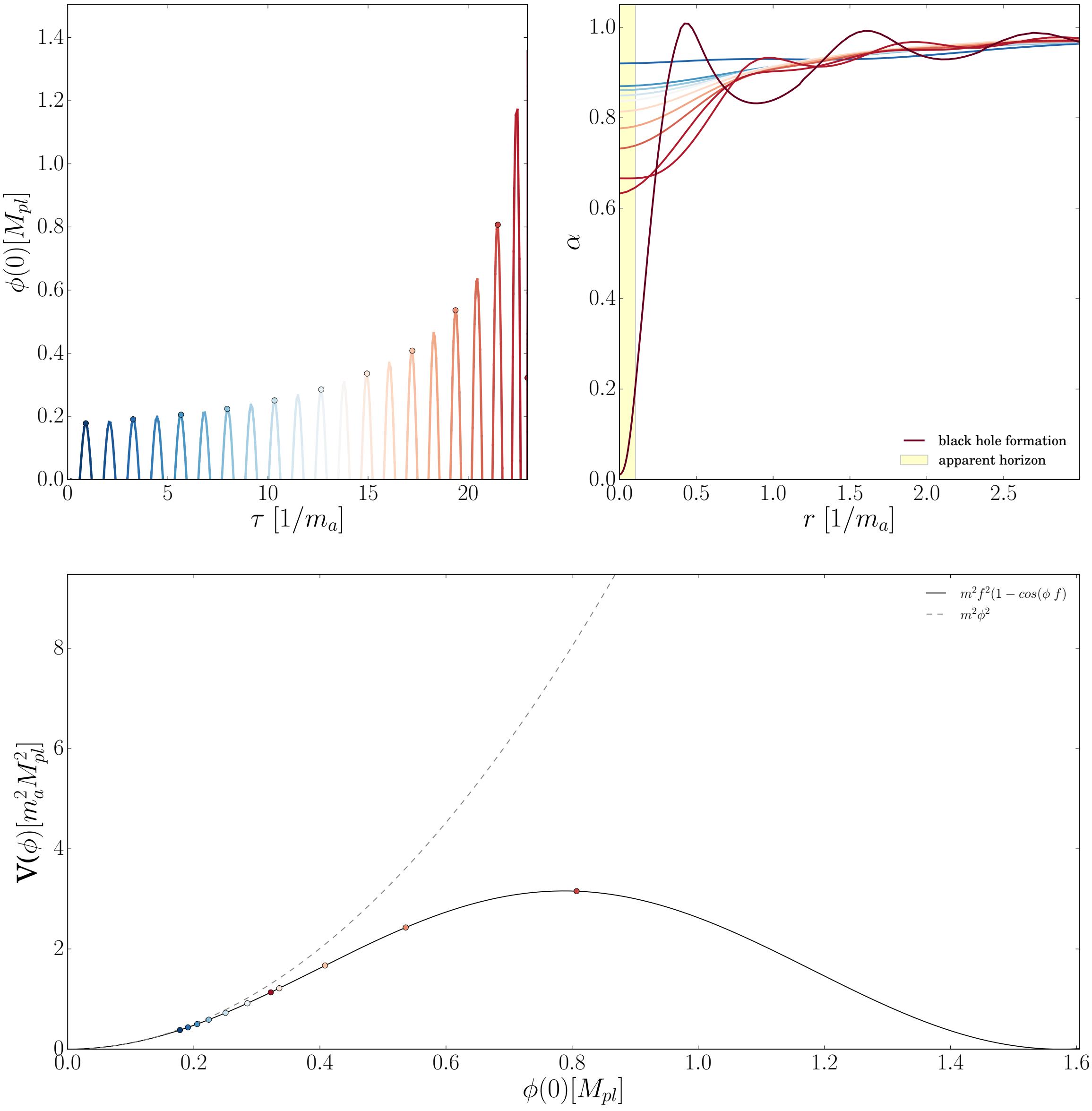

Fig. 2.4 **Black hole formation near the triple point.** $(M_{\mathrm{ADM}}, f_a) = (2.51, 0.35)$, R2 square in Fig. 2.1. The central field value is shown evolving over time in the top left panel, with the color gradient on the line used to indicate times in the other panels. The top right panel shows the radial profile of the lapse, α, on different time slices. In the bottom panel, several points are marked to show the movement of the central field value on the potential. Over time, the field amplitude slowly grows and leaves the $m^2\phi^2$ regime, even though initially it provides a good approximation to the axion potential. Shortly after the field goes over the “potential hill”, the Axion star collapses to form a BH. BH formation is indicated by the value of α at the centre approaching zero. The yellow bar indicates the position of the apparent horizon shortly after it forms. Note that local proper time τ is used rather than simulation time t, to remove gauge effects due to the strongly varying lapse.

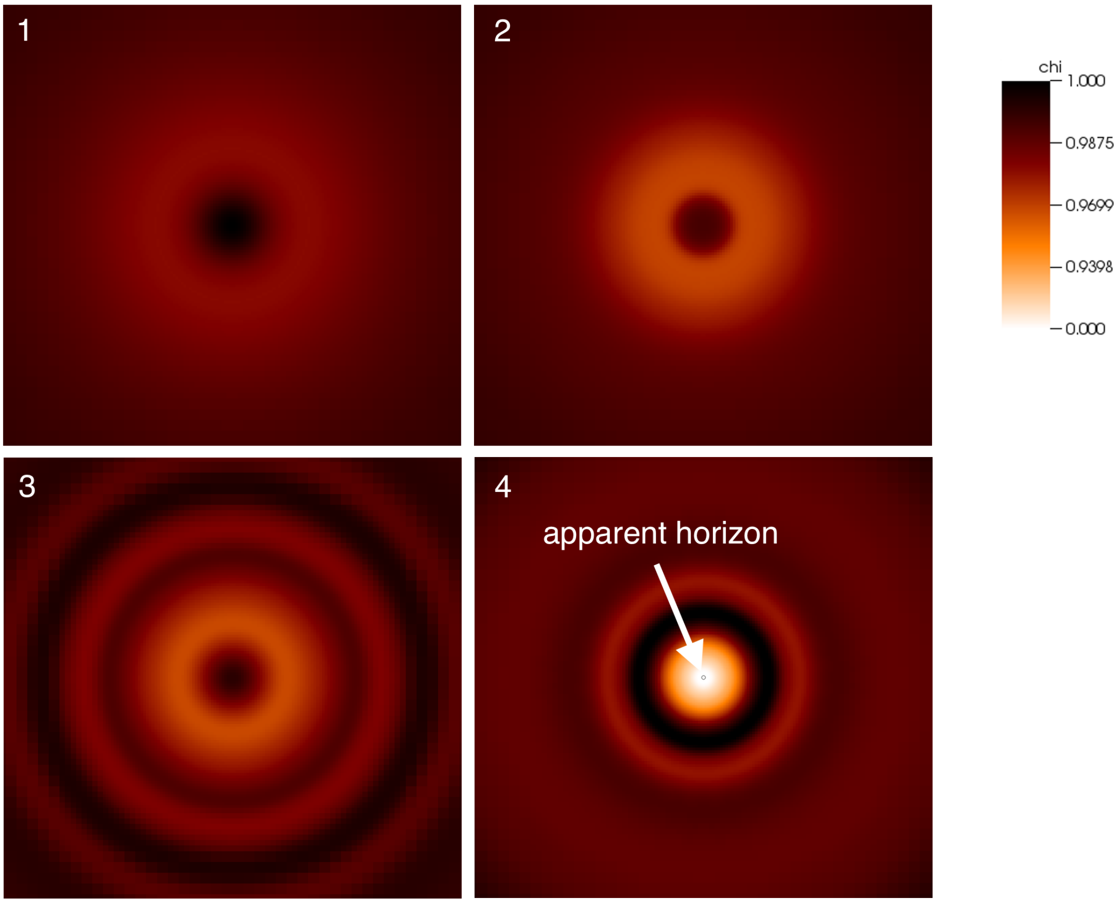

Fig. 2.5 **Black hole formation near the dispersal region.** $(M_{\mathrm{ADM}}, f_a) = (2.63, 0.055)$, R2 star in Fig. 2.1. The parameter shown is the conformal factor of the metric, χ (for a definition see Appendix A.3). The first panel shows the initial data, and subsequent panels show the evolution. The initial state is spatially extended, with low curvature. As collapse proceeds, the Axion star becomes smaller, and some scalar radiation is emitted in waves. The final BH has an apparent horizon that is very small compared to the initial Axion star size. Some of the axion field remains outside the BH, and gravitationally bound to it, which we discuss in Section 2.2.5.

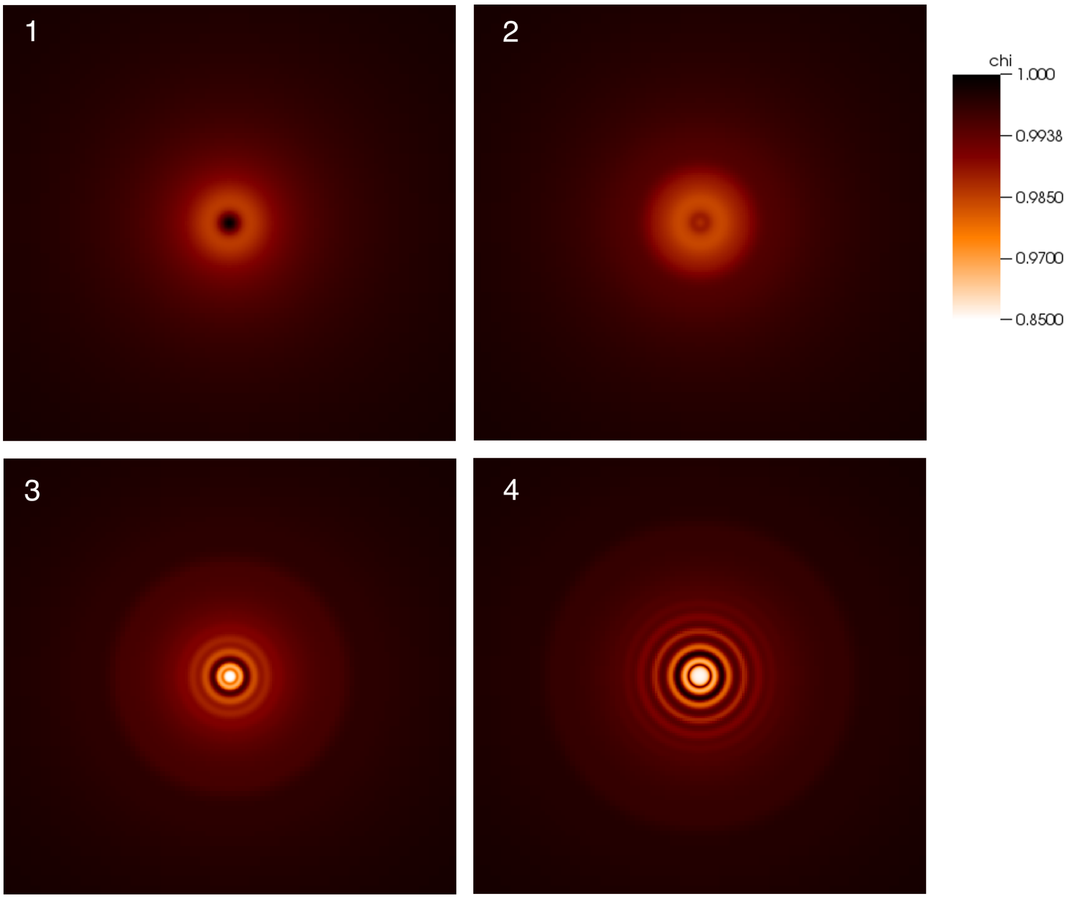

Fig. 2.6 **Dispersion of Axion stars.** $(M_{\mathrm{ADM}}, f_a) = (2.40, 0.14)$, R3 star in Fig. 2.1. The parameter shown is the conformal factor of the metric, χ (for a definition and relation to the Newtonian potential see Appendix A.3). Note that the colour scale for the conformal factor, χ is not the same as in Fig. 2.5, since in the dispersing case the variation in χ is much smaller, corresponding to less spatial curvature. The first panel shows the initial data. The second shows some initial collapse. Collapse then slows, which can be seen by the central peak getting broader and smaller in amplitude from the third to the fourth panel. As the dispersal continues, we notice matter shells being ejected. The evolution of $\chi(0)$ over a longer time scale is shown in Fig. 2.7.

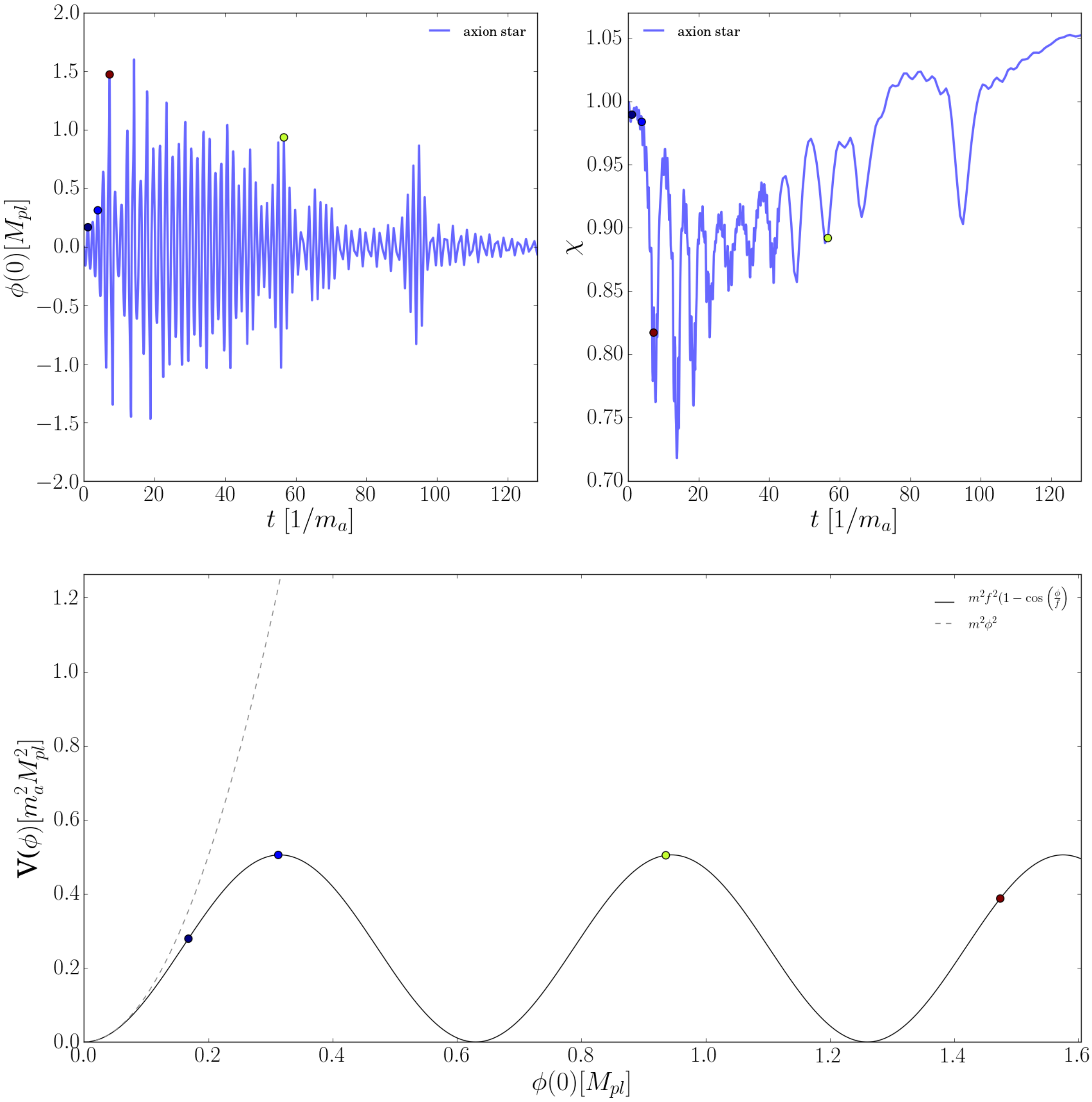

Fig. 2.7 **Dispersion of Axion stars.** $(M_{\mathrm{ADM}}, f_a) = (2.40, 0.14)$, R3 star in Fig. 2.1. The parameter shown is the conformal factor of the metric, χ, which can be related to the Newtonian Potential in the weak gravity case (for a definition see Appendix A.3). Several points are marked to show the movement of the field on the field potential. The field quickly leaves the stable Axion star regime and the amplitude grows. Eventually the field goes “over the top” in the cosine potential: equivalent to the field winding in the complex plane. The amplitude then slowly decays by ejecting matter shells (see panel 4 of Fig. 2.6). The interplay between gradient energy and nonlinear interaction causes a very intricate evolution.

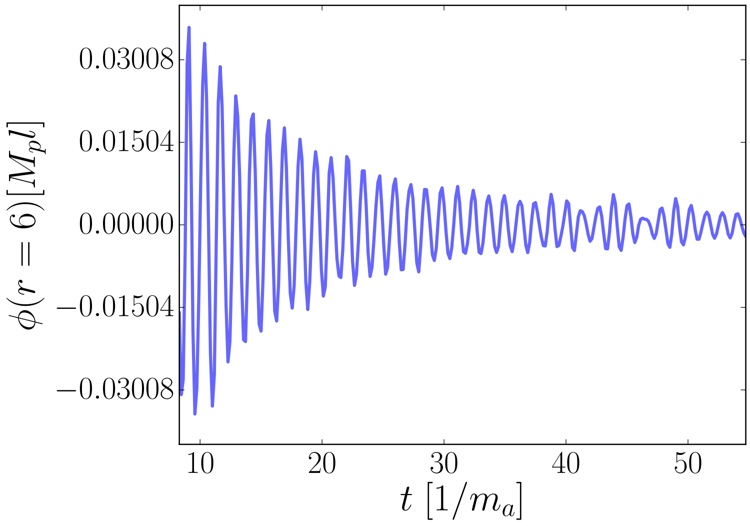

Fig. 2.8 **"Scalar wig".** $(M_{\mathrm{ADM}}, f_a) = (2.63, 0.055)$, R2 star in Fig. 2.1. Evolution of the scalar field outside the horizon, beginning at the point in time when the apparent horizon appears. The scalar field seems to fall slowly into the black hole, however, the configuration seems to be long-lived, i.e. stable for many oscillations.

Chapter 3

Formation of Relativistic Axion Stars

The work presented in this chapter is derived from the paper "Formation of Relativistic Axion Stars" [190], published in the Journal of Cosmology and Astroparticle Physics (JCAP).

Axions and axion-like particles are compelling candidates for the missing dark matter of the universe. As they undergo gravitational collapse, they can form compact objects such as Axion stars or even Black holes. In this paper, we study the formation and distribution of such objects. First, we simulate the formation of compact Axion stars using numerical relativity with aspherical initial conditions that could represent the final stages of axion dark matter structure formation. We show that the final states of such collapse closely follow the known relationship of initial mass and axion decay constant f_a. Second, we demonstrate with a toy model how this information can be used to scan a model density field to predict the number densities and masses of such compact objects. In addition to being detectable by the LIGO/VIRGO gravitational wave interferometer network for axion mass of $10^{-9} < m_a < 10^{-11}$ eV, we show using peak statistics that for $f_a < 0.2M_{pl}$, there exists a "mass gap" between the masses of Axion stars and Black holes formed from collapse.

3.1 Introduction

The Advanced Laser Interferometry Gravitational wave Observatory (LIGO) has made historic measurements of gravitational waves (GW) from the binary coalescence of Black holes [5] and neutron stars [191]. This paves the way for searches for signals from "exotic compact objects" (ECO; see e.g. [55, 16, 85, 192, 83, 86, 193]). Axions and axion-like particles [194–197, 139, 160, 161, 198, 199, 128, 200, 140, 201, 202] (which we refer to collectively as simply "axions") can form such ECO, known as Axion stars, which are related to a family of compact scalar field (pseudo)-solitons including Wheeler's "geons", Boson stars, and oscillatons [28, 108, 34, 109, 203].

To have a strong GW signal in LIGO, the ECO must have mass and compactness,

$$\mathcal{C} \equiv \frac{GM_\star}{R}, \tag{3.1}$$

where $M_\star$ is the mass of the object, in a particular range [16]. Simulations have shown that there are known environments in dark matter halos in which non-relativistic Axion stars form [204–208]. Any source of large (possibly primordial) density perturbations, or rapid merging and accretion could potentially grow such stars into the range of mass and compactness accessible to LIGO, and even beyond as they collapse to BH or disperse as novae [17]. However, there have not been simulations of the final stages of Axion star formation in the full relativistic regime and beyond spherical symmetry, which are required to determine the fate of large axion densities.

In the following we simulate the formation of compact Axion stars and BH from some pseudo-random initial conditions using full (3+1) dimensional numerical relativity simulations with GRCHOMBO [209]. Our results can be used to assess Axion star formation given some input realisation of the axion density field. We demonstrate this for a toy model density field, using peak statistics to label compact Axion stars and BH in the LIGO frequency band.

We remain agnostic about the amount of dark matter (DM) that might be contained in compact Axion stars, noting only that it must be relatively small, of order a few percent (see e.g. the compilations of primordial BH constraints in [210–212]). Given the theoretical uncertainties in formation mechanisms for compact Axion stars from axion dark matter, such bounds can easily be consistent with all the dark matter being axions.

We use units $= c = 1$ and $M_{pl} = 1/\sqrt{8\pi G}$ is the reduced Planck mass.

3.2 Gravitational Waves from ECOs

In the following we review the description of GWs from ECOs given in [16]. An ECO is described by two parameters, the mass, $M_\star$, and the compactness, $\mathcal{C}$, which together determine the frequency and amplitude of GWs produced in a binary inspiral (the merger and ringdown phase contain more information requiring direct simulation). The orbital period, P, is related to the total binary mass, M_{tot} and semi-major axis, l, by Kepler's third law

$$P^2 = \frac{4\pi^2 l^3}{GM_{tot}}. \tag{3.2}$$

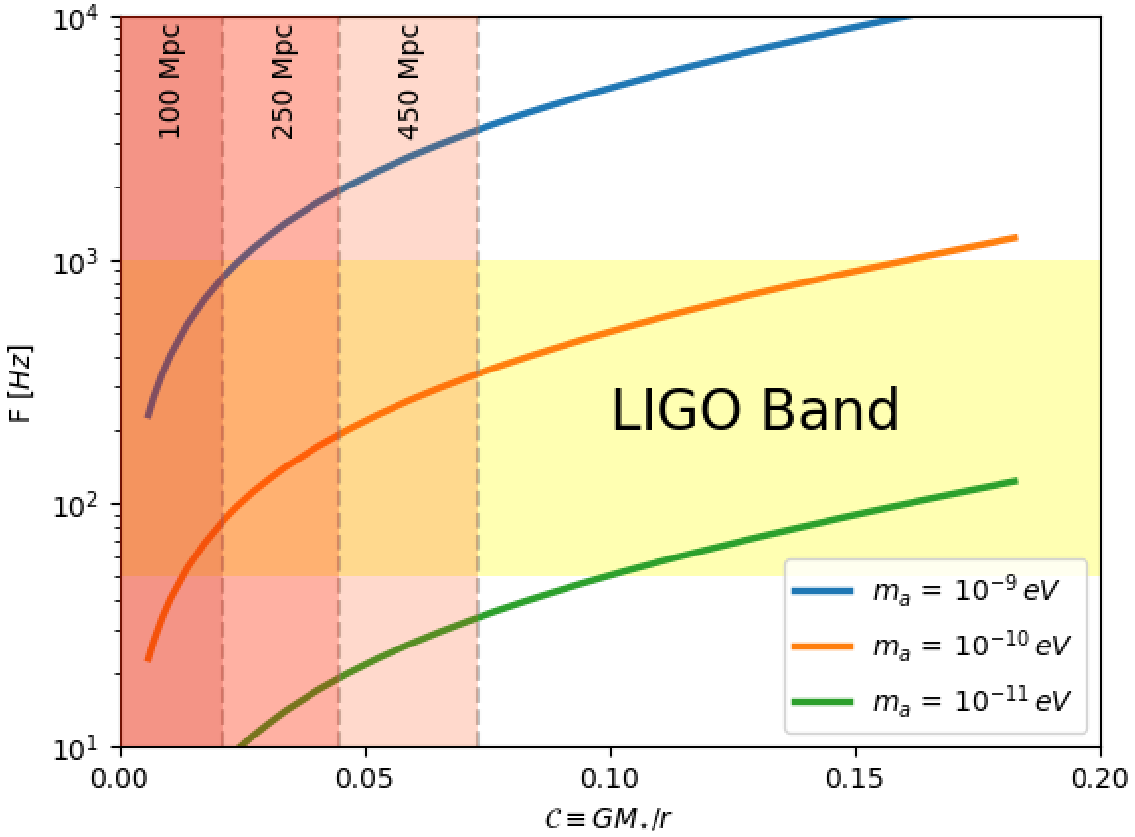

Fig. 3.1 **LIGO frequency band for Axion stars.** The frequency is given by the ISCO frequency, Eq. (3.6). The compactness $\mathcal{C}(M)$ is for non-interacting oscillatons, which is a good description of stable Axion stars. Assigning a luminosity distance to binaries, the minimum compactness is found from the results of Ref. [16]. Axion stars detectable by LIGO must have $\mathcal{C} \gtrsim 0.02$ and axion mass $m_a \approx 10^{-10}$ eV.

The frequency, f, of gravitational wave emission is twice [1] the orbital frequency, $\nu = 1/P$, and hence is given by

$$f = \sqrt{\frac{GM_{tot}}{\pi^2 l^3}} \,. \tag{3.3}$$

The innermost stable circular orbit, ISCO, determines the end of the inspiral phase, and the beginning of the merger phase. For a blackhole binary, the ISCO is given by

$$R_{\rm BH}^{\rm ISCO} = 6GM_{tot} \,. \tag{3.4}$$

For an ECO, the ISCO is modified by the variable compactness:

$$R_{\rm ECO}^{\rm ISCO} = \frac{3GM_{tot}}{\mathcal{C}} \,. \tag{3.5}$$

Hence the typical frequency, $f_{\rm ECO}^{\rm ISCO}$, of two merging ECO is

$$f_{\rm ECO}^{\rm ISCO} = \frac{\mathcal{C}^{\frac{3}{2}}}{3^{\frac{3}{2}}\pi GM_{tot}} \,. \tag{3.6}$$

For blackholes, the maximum frequency for gravitational wave emission at the end of the inspiral is given by numerical relativity, and is defined as $f = (1+\Delta) f_{\rm BH}^{\rm ISCO}$. Δ is a correction term computed in post-Newtonian approximation [213], and is dependant of the mass ratio and spins of the blackholes. In the parameter range where the post-Newtonian approximation is valid, it was found that $\Delta = \mathcal{O}(1)$, although we only expect this to hold for relatively compact objects with $\mathcal{C}$ within a factor of a few of BH. With this knowledge, for the discussion we deem it adequate to take Eq. 3.6 as the typical frequency of gravitational wave emission.

The LIGO noise-power spectral density is minimized between 50 Hz and 1000 Hz. Placing the frequency in Eq. 3.6 in the LIGO band gives the range of M and $\mathcal{C}$. For BH we find the benchmark mass for LIGO of $M_\star \approx 10 M_\odot$ stellar mass BH, while for LISA one finds sensitivity to supermassive BHs, $M_\star \approx 10^3 - 10^7 M_\odot$. Ref. [16] considered the signal to noise for ECO binary mergers in the LIGO band, and found that for events within a given luminosity distance D_L there is a minimum value of $\mathcal{C}$ at any given mass to give an event with large signal to noise.

Fig. 3.1 shows the results of Ref. [16] for the minimum compactness for different luminosity distances together with the $\mathcal{C}(M)$ relation for Axion stars determined from spherically symmetric numerical GR [17, 19]. Axion stars detectable by LIGO must have $\mathcal{C} \gtrsim 0.02$ and axion mass $m_a \approx 10^{-10}$ eV, implying that the Axion stars are of approximately solar mass.

---

[1] As both frequency, f, and orbital frequency, ν, contain factors of 2π we can cancel them for ease

3.3 Axion Star Formation

Axion stars giving rise to potential GW inspiral signals in LIGO have high compactness, and are thus relativistic objects. If Axion stars can reach such high compactness, they could also surpass their maximum stable mass, entering the unstable region in the "phase diagram" [17, 18, 214], either collapsing to a BH or dispersing in a nova, depending on the axion "decay constant", f_a.

3.3.1 Initial Conditions

We consider an initial state of energy density in the axion field characterised by a single momentum scale, $k_\star$, in a superposition of waves in (x, y, z):

$$\phi = \varphi \left[\cos k_\star x + \cos k_\star y + \cos k_\star z\right] . \tag{3.7}$$

The waves have initially zero velocity, $\dot{\phi} = 0$. We impose periodic boundary conditions on our computational domain, and hence the initial condition is that of a superposition of waves that is not spherically symmetric, but possesses a 6-fold discrete permutation symmetry. This breaks spherical symmetry for the density peak, allowing us to investigate the effects of anisotropy while keeping the parameter space sufficiently small so that we can scan through them with available computational resources. This initial condition represents a locally overdense region dominated by the axion energy density, and hence is decoupled from the Hubble flow.

According to the results of Ref. [17] we expect collapse to be governed by two parameters: the total mass, M, in a single overdensity (periodic boundary conditions means that this is half the total box mass), and the axion decay constant, f_a, defining a "phase diagram".[2] The total maximum mass in an overdensity is found by integrating the initial potential energy inside the box, and dividing by two (as two objects will form due to symmetry):

$$\frac{1}{2} \int_V \rho \sqrt{\det \gamma_{ij}} dV \, , \tag{3.8}$$

---

[2] This diagram has been explained by various arguments in Refs. [215, 216]. The phase boundaries have been accurately determined using spherically symmetric simulations by [18]. See also the simulations of [214] who study the regime of low f_a and low curvature leading to axion emission.

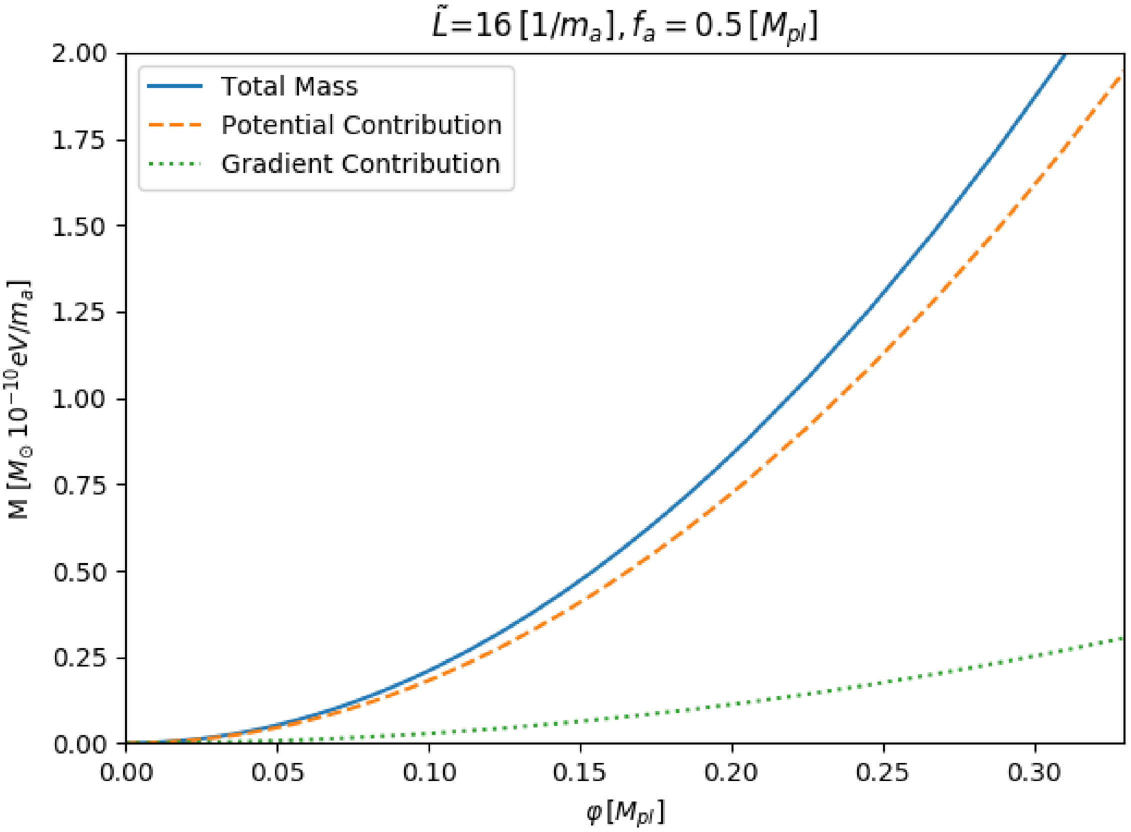

Fig. 3.2 Using 3.10 we calculate the total box mass, M, of our initial conditions for a box size of $\tilde{L} = 16 m_a^{-1}$ and $f_a = 0.5 M_{pl}$, as well as the contributions to M of the gradient term, $\frac{1}{2}(\partial_i \phi)^2$, and the potential term, $V(\phi)$. For the f_a simulated it can be seen that our initial mass is dominated by contributions from the potential term.

with

$$\rho = n^{\mu} n^{\nu} T_{\mu\nu} \,, \tag{3.9}$$

where n^{μ} is the normal to the hypersurface and γ_{ij} the 3-D spatial metric. Assuming that the metric is conformally flat as our initial energy density has a small average density, then using B.9

$$M = \frac{1}{2} \int_{-L/2}^{L/2} \mathrm{d}x \, \mathrm{d}y \, \mathrm{d}z \left(\frac{1}{2} (\partial_i \phi)^2 + V(\phi) \right) \,, \tag{3.10}$$

where $L \equiv 2\pi / k_*$ is the physical size of the periodic domain. We also define the corresponding scaled size $\tilde{L} = 2\pi m_a / k_\star$ and mass $\tilde{M} = M m_a$. The axion potential energy is given by

$$V(\phi) = m_a^2 f_a^2 \left[1 - \cos\left(\frac{\phi}{f_a} \right) \right] \,. \tag{3.11}$$

By a choice of units, the axion mass m_a can be scaled out of all our simulations; units can be easily restored to set the physical mass of the compact objects formed. To achieve this scaling, we chose

$$M = 0.27 \tilde{M} \left(\frac{10^{-10} \text{ eV}}{m_a} \right) M_{\odot} \tag{3.12}$$

where $M_{\odot}$ is the solar mass. Meanwhile, for small $\tilde{L} < (\varphi / f_a)$ the gradient term dominates. Eq. 3.2 shows the initial conditions for the smallest $\tilde{L}$ we simulated and for $f_a = 0.5 M_{pl}$. All of our numerical simulations had initial conditions where potential energy dominated.

Finally, we can compute the average energy density of the simulation domain via

$$\bar{\rho} = \frac{M}{L^3} \,, \tag{3.13}$$

and hence the "local" Hubble constant $H_{\text{local}}^2 = (1/3 M_{pl}^2) \bar{\rho}$ which is $H_{\text{local}} \sim m_a$. We emphasise that this is not related to the "global" Hubble constant, since we are simulating a local overdense region.

Our simulations begin at an arbitrary dimensionless time, and we should ask how this is related to the cosmic time. In our simulations, we are evolving an axion dominated overdense local patch that is much smaller than the current Hubble radius, thus it is assumed that the expansion of the Universe and the presence of any fluctuation in energy density of non-axion components can be neglected. Thus, a fluctuation of any amplitude in our simulations will collapse, and cosmologically we cannot relate this to the collapse threshold for a given redshift.

A perturbation mode of *co-moving* wave number k with frequency $\omega^2(a) = (k/a)^2 + m_a^2$ will begin to evolve when $\omega(a) > H(a)$. Consider a co-moving mode $k_{\rm cm}$ which re-enters the horizon at time $a_{\rm ret}$, $k_{\rm cm} = a_{\rm ret}H(a_{\rm ret})$. Furthermore, if $H(a_{\rm ret}) < m_a$, then the mode will collapse only at time $a_{\rm osc} > a_{\rm ret}$ where $H(a_{\rm osc}) \approx m_a$, i.e. when the mode is subhorizon. In our simulations, our box size is set to $\tilde{L} = 2\pi m_a/k_\star$ where $k_\star$ is a *physical scale* and related to the co-moving wave vector $k_{\rm cm}$ by an arbitrary scale factor a.

From our choice of dimensionless units, this means that the physical length $k_\star^{-1} = (\tilde{L}/2\pi)m_a^{-1}$. As will be described in section 3.3.2, we take $\tilde{L} = \mathcal{O}(16 \sim 128)$ in our simulations, and hence $k_\star < m_a$, which satisfies the condition for subhorizon collapse above.

3.3.2 Numerical Simulations

We simulated collapse of a massive scalar field, ϕ, with an axion potential in numerical relativity, using GRChombo [134]. Details of the numerical scheme can be found in **??**. We probed a three dimensional “phase diagram", summarised in Fig. 3.3, to investigate how collapse differed whilst varying initial mass M, length scale of the axion waves $\tilde{L}$, and decay constant f_a. In the following sections we will explore the different types of structure that can be formed according to the parameters of the “phase diagram", as well as commenting on the technical limitations that we faced.

To explore the possible “phase diagram" of initial conditions for Axion star collapse, we choose three length scales of the axion waves $\tilde{L} = 16, 64, 128\ m_a^{-1}$, two decay constants $f_a = 5.0, 0.5\ M_{pl}$ and four initial total box masses $M = 2.14, 1.34, 1.07, 0.80\ M_\odot\,(10^{-10}\text{eV}\ m_a^{-1})$. These initial conditions were chosen so that we can form a range of final structures; Axion stars and Black holes, like those found in [17, 18]. We fix our boundary conditions to be periodic.

We used varying adaptive mesh refinement (AMR) conditions based on the length scale, $\tilde{L}$, of the axion wave (discussed in B.1.2 in more detail). Each AMR level had a refinement ratio of two, with the coarsest grid set at a resolution of 64^3. Convergence and stability of the simulations is discussed in B.1.3.

B.1.1 has a complete discussion on the initial conditions used. To summarise we calculate the initial value of trace of the extrinsic curvature, K, using

$$K = -\sqrt{24\pi G\langle\rho\rangle}\,, \tag{3.14}$$

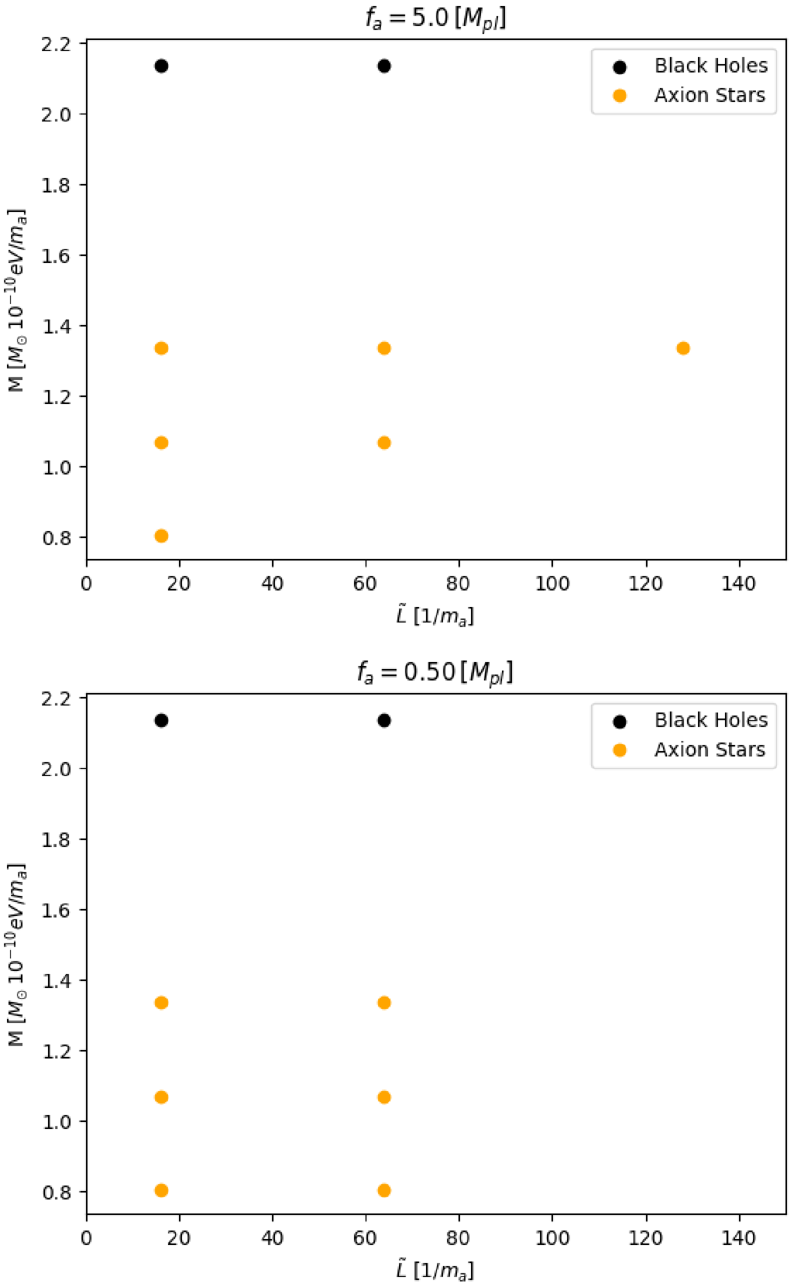

Fig. 3.3 **These plots are a summary of all numerical simulations performed**. Black circles indicate that blackholes where formed from the initial conditions and yellow circles indicate that Axion stars were formed. We emphasise that the y-axis labels the *initial total mass* of the simulation initial conditions, not the final mass of the formed objects. No dispersion cases were obtained, and the reason for this is outlined in 3.3.5. The results presented here mirror that of [17, 18], so when discussing the likely structure formation we will use the “phase diagram" constructed there.

where $\langle\rho\rangle$ average initial energy density. The conformal factor, χ, was calculated using a relaxation procedure until we reached a relative Hamiltonian constraint violation, $\mathcal{H}$

$$\mathcal{H} \equiv \frac{H_{center}}{16\pi G \rho_{center}}, \tag{3.15}$$

of $\mathcal{O}(0.1\%)^3$ and where H_{center} and ρ_{center} are the corresponding variables evaluated in the center of grid. The larger the length scale of the axion waves, the more numerically expensive the simulations were to perform due to an increase in the time scale of collapse, and a need for more refinement layers to track formation and the evolution of the resulting structure.

Blackhole formation is identified using a horizon finder and the formation of an Axion star was identified using an “Axion star location" script, which is detailed in B.1.4.

3.3.3 Axion Star Formation and Evolution

Our simulations with initial conditions $M \leq 1.34\, M_{\odot}\, 10^{-10}\text{eV}\; m_a^{-1}$ resulted in Axion star formation (see Fig. 3.3). To compute the mass, $M_{\star}$, of the Axion stars, we use 3.8, with the radius R computed to be such that $\rho(R) = 0.05\ \rho_{max}$ – this is a good approximation since the Axion star sphericalizes rapidly.

During the course of the evolution the Axion stars were found to be stable (i.e. they do not disperse nor collapse into a BH), sphericalizing rapidly leaving only a dominant radially perturbative mode (see Fig. 3.4). Fig. 3.5 shows the variation of the radius of Axion stars over time generated from spherically symmetric initial data [17, 19]. The radial variation in the spherically symmetric case is long lived, and the computational cost of evolving the stars to their final end-state (presumably an unexcited star) is prohibitive. For $f_a = 5.0 M_{pl}$ the radial variation presented in Fig. 3.4 is negligible for both masses shown. When lowering f_a to $0.5 M_{pl}$ it can be seen that the more massive Axion star collapses to a blackhole, however for the less massive Axion star a radial variation with a period of $300 m_a^{-1}$ develops. The radial variation shown here has a longer period compared to the most massive case for $\tilde{L} = 16$, and shorter compared to $\tilde{L} = 64$. We conclude that the variation in radius of the stars from our formation process comes dominantly from decaying radially perturbative modes.

As has been shown in [55], ground state Axion stars span a family parameterized by the compactness parameter $\mathcal{C}$. When studying the compactness of Axion stars formed by our collapse process vs this family, it can be seen that these formed stars oscillate around this family, hence represents stable stars. This can be seen in Fig. 3.4.

---

[3] During the relaxation routine the value of H and ρ at the centre of the simulation was also the max value of those variables

Finally, we compute the efficiency of the Axion star formation process, which is defined as

$$\text{Efficiency} \equiv \frac{\text{Total Initial Mass}}{\text{Mass captured in AS}}\,. \tag{3.16}$$

This is measured to range from 0.5 for $\tilde{L} = 128$ to 0.8 for $\tilde{L} = 16$. In other words, a large fraction of the initial mass forms the Axion star. Since our simulation domain is periodic, and hence "free scalar field energy" has no place to disperse, we might worry that this may be due to a significant reabsorption. We observed that the Axion star formed in $\mathcal{O}(10)$ "box crossing" times and if reabsorption of the scalar field was big, we should see a modulation in ϕ at 10 times that frequency, which we do not. Hence we surmise that reabsorption is small and expect that while in a dispersive environment the efficiency will be lower, it will not be significantly lower.

3.3.4 Black hole Formation

Meanwhile, our simulations show that initial conditions with $M = 2.14\, M_\odot\, 10^{-10}\text{eV}\; m_a^{-1}$ resulted in Black hole formation (see Fig. 3.3). This is consistent with the "phase diagram" presented in [17, 18]. Similar to the Axion star formation process, we found that the efficiency of Black hole formation was $\mathcal{O}(1)$ (i.e. the final BH contained most of the initial mass).

3.3.5 Dispersion Regime

As shown in the phase diagram constructed in [17, 18], there exists "dispersal regions" where the Axion star is not stable and disperses into scalar radiation. This occurs in regions with sufficiently low f_a and M. Due to the periodic domain, dispersed scalar fields will eventually fall back into a (possibly dispersing Axion star), and hence we cannot probe this possibility. Instead we use the phase diagram constructed in [17, 18] for the analysis that follows.

3.4 Axion Stars and Gravitational Waves

Relativistic Axion stars with high compactness can emit sufficiently strong GW signals which makes them possible targets of gravitational wave detectors. In this section, we will explore this possibility.

The phase diagram of Ref. [17] suggests that, for each value of f_a below the "triple point", $f_{\rm TP} \approx 0.2 M_{pl}$, there are three phases of Axion star: low mass stars are stable; those above a first critical mass, $M_{\rm disp.}$ are unstable to emission of relativistic axion waves; those above

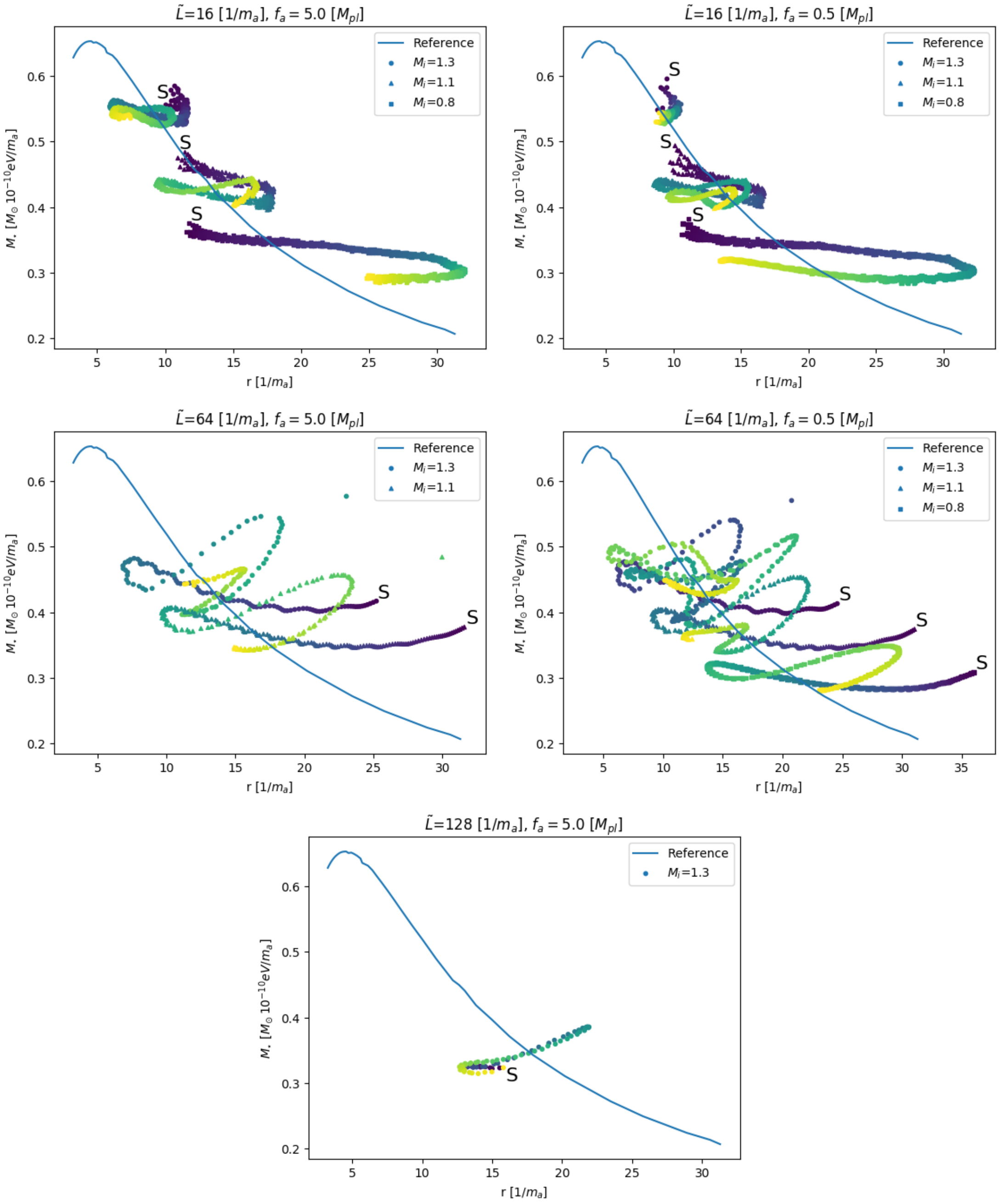

Fig. 3.4 **Evolution of the mass-radius relation of all simulations whose end state was identified as an Axion star.** The reference line in the plots is the mass radius relation for an unexcited Axion star, and the points on top indicate the evolution of the observed star forming. The evolution in time of the mass-radius relation is indicated by the colour of the point, with the darkest points being the earliest in the evolution and the lightest points being the end of the evolution. Additionally the start point of the evolution is indicated by an ‘S’. The mass radius relation fluctuates significantly over time, varying in a decaying way around the unexcited star value. This process is attributed to the formed stars having radial perturbative modes. Outliers on these graphs are due to the Axion star finder, outlined in B.1.4

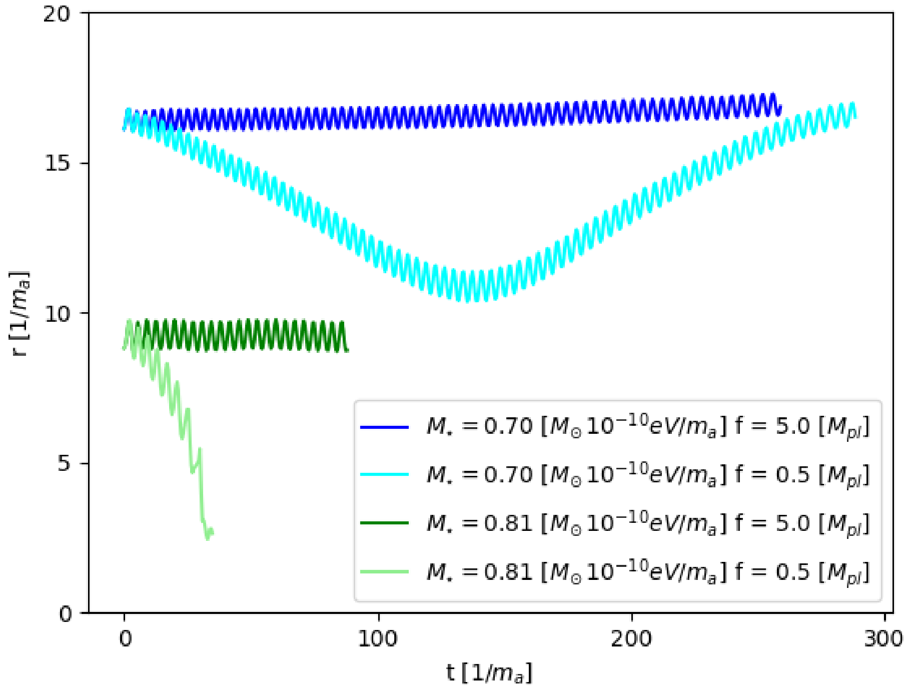

Fig. 3.5 **Variation of the Axion star radius over time for spherically symmetric initial data [17, 19]** . For $f_a = 5.0 M_{pl}$ the radial variation is negligible for both masses shown. When lowering f_a to $0.5 M_{pl}$ it can be seen that the more massive Axion star collapses to a blackhole, however for the less massive Axion star a radial variation with a period of $300 m_a^{-1}$ develops. The radial variation shown here has a longer period compared to the most massive case for $\tilde{L} = 16$, and shorter compared to $\tilde{L} = 64$.

a second critical mass, M_{BH}, collapse to BHs. Above the triple point, the dispersal phase no longer exists, and compact objects form for all masses. Our numerical simulations have verified that this same picture applies to the "cosmological" initial conditions of Fig. 3.7.

3.4.1 Cosmological Formation of Axion Stars

Axion stars are the (quasi-)stable end point of gravitational collapse of the axion field, and in simulations of dark matter structure formation have been observed to form in diverse conditions [208, 111, 188]

Non-relativistic axions stars are observed to form in simulations with coherent initial conditions, where they condense via monolithic collapse as the first generation of axion DM halos, with a population expected to inhabit the centres of all halos [111, 217, 207]. These Axion stars form from the small ($\zeta \approx 10^{-5}$) amplitude adiabatic curvature fluctuations which dominate the Universe on large scales, with the coherent initial conditions provided if Peccei-Quinn symmetry is broken during inflation. Cosmological simulations of this formation mechanism have only been performed for ultralight axions with $m_a \approx 10^{-22}$ eV. The corresponding Axion stars in dwarf galaxies are too heavy to be relevant for LIGO. The formation mechanism, however, is expected to be operative for all axion masses in all dark matter halos [218], potentially leading to relativistic cores in some region of parameter space.

Recently, axions stars were also shown to condense from highly incoherent initial conditions [208]. This mechanism is expected to be active in axion "miniclusters" [219, 112, 220, 221], and indeed throughout any axion dark matter halo, potentially leading to spontaneous Axion star formation. [208] proposes a growth rate that could make these Axion stars reach relativistic masses if it does not quench. Mergers of such Axion stars could also lead to mass increase.

Non-relativistic simulations like these provide realisations of the axion field with Axion star locations. Dense peaks of this field will require individual relativistic simulations, and the evolution should resemble the cases that we have studied in the present work. In this model, the Axion star population builds up over time in an astrophysical way, just as ordinary stars and BH do.

It is also possible that relativistic Axion stars could form directly in the early Universe from large amplitude primordial fluctuations, a possibility we discuss in more detail in Section 3.5. In this case also, dense peaks of the axion field will evolve to relativistic Axion stars as studied above. In this model, the Axion star population resembles primordial BH.

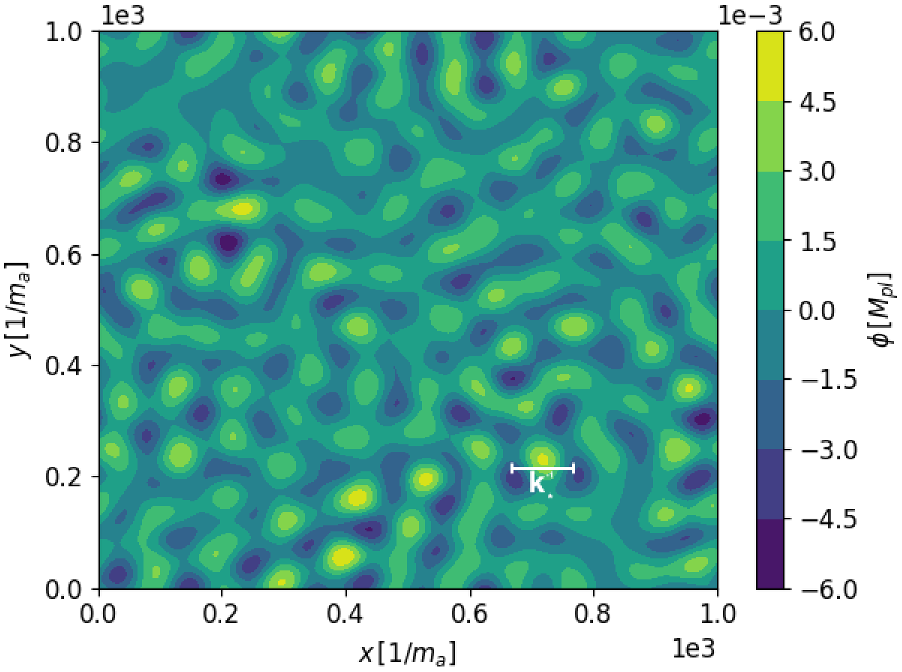

Fig. 3.6 **A toy model realisation of the axion density field** that can be filtered to locate candidate compact Axion stars.

3.4.2 Peak Statistics

Simulating a cosmological volume of initial conditions for the axion field with numerical relativity is not feasible. Instead we consider our simulations as representing isolated peaks in the density field.

We consider a toy model for an axion density field containing large amplitude peaks that can be described by our numerical simulations. A simple mechanism to form massive, dense, primordial AS in the LIGO band is to enhance the axion power spectrum by a Gaussian bump on small scales:

$$P_{\delta\phi} \equiv A \exp\left[\frac{-(k-k_\star)^2}{2\sigma_k^2}\right] , \tag{3.17}$$

where A is the amplitude, $k_\star$ the central mode, and $\sigma_k \ll k_\star$ the width. The amplitude has units $M_{pl}^2 m_a^{-3}$. Fig. 3.6 shows the toy model for the axion density field with k_*^{-1} roughly equal to the size of a peak described by our numerical simulations. For any axion density field like this toy example (e.g. density field and Axion star location inside a DM halo), we can calculate the mass distribution of Axion stars and BH formed by the extreme peaks by analogy to the theory of critical collapse for BHs, and to the Press-Schechter theory of cosmological structure formation.

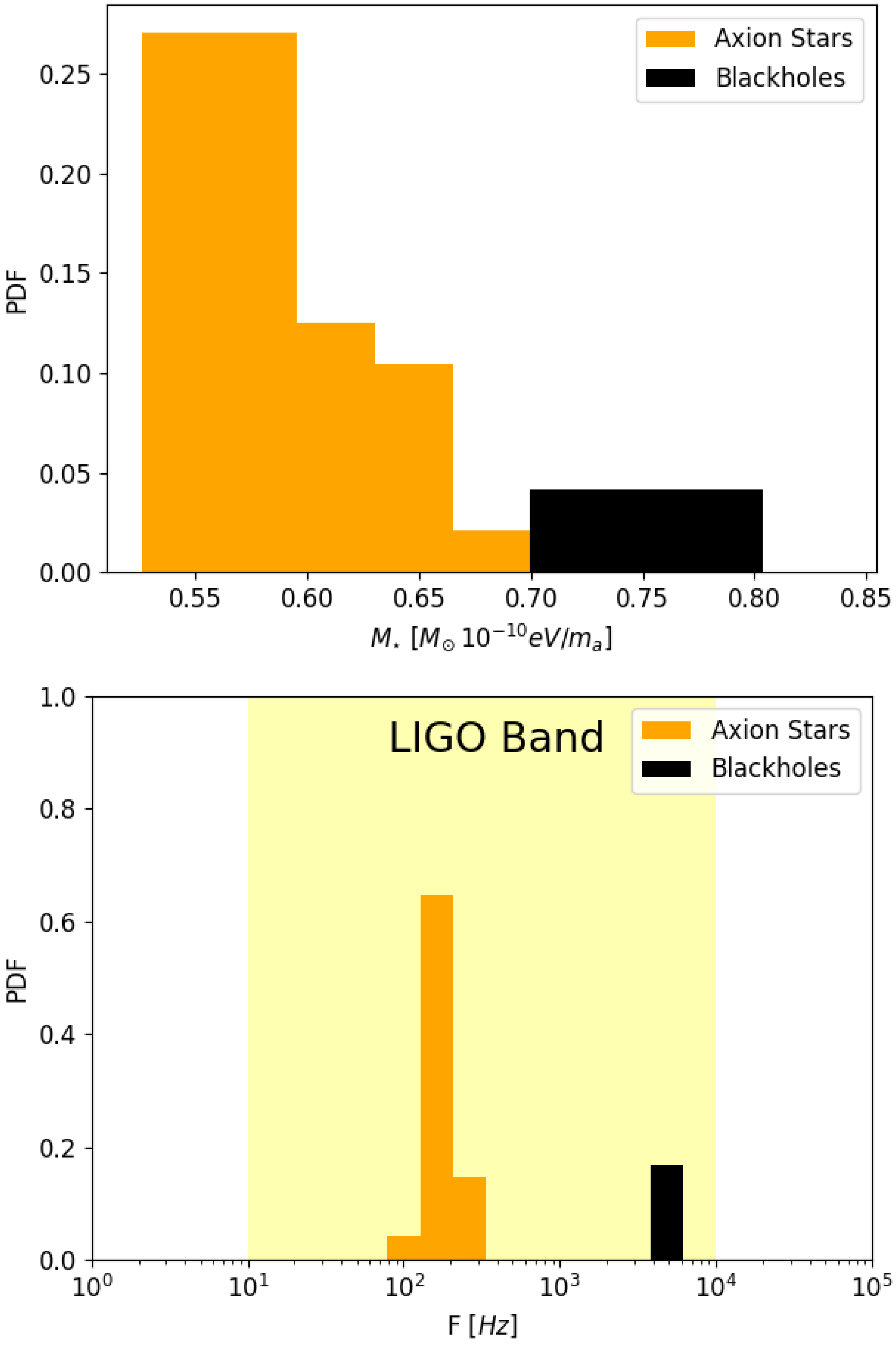

Fig. 3.7 Top panel: Peaks of the toy model density field are assigned masses as Axion stars and Black holes according to the location on the phase diagram with $f_a = 0.5\ M_{pl}$. Bottom panel: Using Eq. 3.6 and the $\mathcal{C}(M)$ relation for Axion stars, we calculate the gravitational wave frequencies for Axion star and BH equal mass binary mergers.

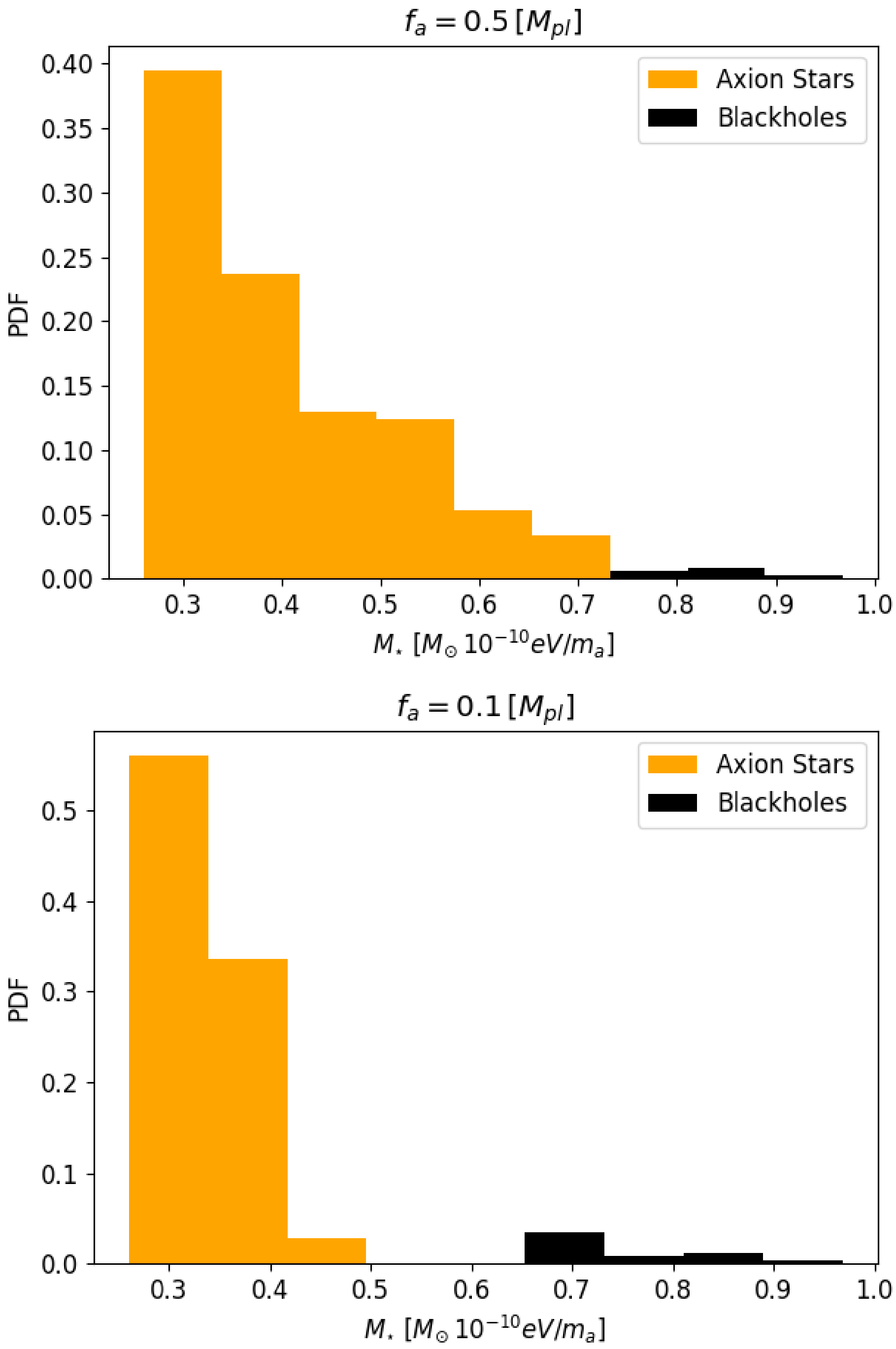

Fig. 3.8 Peaks of the toy model density as Fig. 3.7 with $f_a = 0.5\ M_{pl}$ (upper panel) and $f_a = 0.1\ M_{pl}$ (lower panel). Note that as f_a dips below the triple point [17], a dispersal gap appears between the formation of Black holes and Axion stars.

The peak statistics are determined by thresholding the field, and are classified using a two pass connected component clustering algorithm, see B.1. We partition the distribution for $\tilde{M}_{\star}(f_a)$ according to the critical masses $M_{\text{disp.}}$ and M_{BH} in the phase diagram [17]. In our numerical simulations, due to the construction with periodic boundary conditions and an isolated fluctuation, fluctuations of all amplitudes leading to Axion stars with radius smaller than the box size will eventually collapse under self-gravity. Thus we cannot determine the critical threshold for Axion star collapse. However, we are only interested phenomenologically in the densest, and thus most massive stars, and so we threshold our field for a minimum compactness of the final Axion star assuming that at least these most compact objects successfully collapse.

Figs 3.7 and 3.8 apply such a thresholding and labelling to a statistically representative realisation of the toy model field of Fig. 3.6, taking only the one percent densest peaks. The labelled peaks span from Axion stars, to a mix of Axion stars and blackholes, to primarily blackholes depending on the field variance. Lowering f_a below f_{TP} results in the formation of a mass gap of objects. In particular, as f_a dips below the triple point at $f_{\text{TP}} = 0.2M_{pl}$, a mass gap appears between the masses of formed Axion stars and Black holes. This mass gap is a characteristic feature of Axion stars, hence the observation of a mass gap in the power spectrum of compact objects is a clear method of identifying the existence of axions in the universe.

We can also estimate the frequency of gravitational waves emitted by an Axion star-Axion star or BH-BH binary merger using Eq. (3.6). Assuming binary mergers from the density field simply takes the field statistics as representative: no merger rate is calculated. Fig. 3.7 shows the frequencies with an axion mass of $m_a \approx 10^{-10}$eV. We observe that, for this distribution of peaks, Axion star binary coalescence, as well as BH-BH binary coalescence from collapsed Axion stars fall in the LIGO band.

3.5 Discussion

It is important to note that only a small fraction of the DM density should be contained in Axion stars and primordial BH. It is still an intriguing possibility that some GW events detectable by LIGO might be due to primordial BH, and the distribution of GW events could be used to confirm this [101]. Similarly, GW events and their distribution could confirm the existence of a fraction of DM in Axion stars and BH formed from their collapse [222, 223].

Recent work with scalar compact objects head on mergers [85, 83, 19, 224] indicates distinctions in the gravitational wave signal with respect to blackholes. If these distinctions also exist in binary coalescence (see [14, 225, 84] for Boson star inspirals), a single GW event could be a smoking gun for the existence of Axion stars. The end state mass spectrum from a number of such events could be used to determine the axion decay constant.

One possible mechanism to form compact axions stars in the early Universe is to enhance the axion power spectrum, $\langle \delta\phi(k)\delta\phi(k')\rangle$, on small scales, similarly to production methods for primordial Black holes (see Ref. [226] and references therein). Such enhanced axion fluctuations on small scales arise generically in models of inflation in which the radial mode of the Peccei-Quinn field evolves as a spectator, leading to a strongly blue axion spectrum [227, 228].

Unfortunately, under standard cosmological assumptions such a power spectrum cannot form compact Axion stars. A fluctuation in the axion field at early times is isocurvature (since the axions are subdominant compared to the radiation). During the radiation epoch, the linear transfer function of isocurvature overdensities is close to unity [229]. This implies that, between the time the axion field becomes non-relativistic, $H(a_{\rm osc}) \approx m_a$, and matter-radiation equality, $a_{\rm eq}$, the field fluctuation is redshifted as $\delta\phi \sim a^{-3/2}$. For the axion masses of interest, $m_a \approx 10^{-10}$ eV $\Rightarrow a_{\rm osc}/a_{\rm eq} \approx 10^{-14}$, giving huge redshift factors.

Collapse of primordial fluctuations could occur during a putative early matter dominated phase [230, 231] (as expected in supersymmetric models, e.g. Refs. [232, 233]), or during reheating if the equation of state is in the correct regime. Study of collapse of Axion stars during such a period, or from primordial curvature perturbations in the radiation era, requires additional simulations that account for the background fluid in addition to the axion scalar field. This interesting possibility, incorporating fluids into GRCHOMBO, will be the subject of future study.

An Axion star in the LIGO band requires $m_a \approx 10^{-10}$ eV. The QCD axion with this mass has $f_a \approx 10^{16}$ GeV, which could possibly be detected directly by ABRACADABRA [234] or CASPEr [235]. However, with this low value of f_a Axion stars cannot reach the required high compactness before becoming unstable. This leads to the interesting conclusion that any future observation of GWs from Axion stars would imply the existence of contributions to the axion spectrum beyond QCD, and could thus lend support to the idea of a "String Axiverse" [200] or other non-standard axion scenarios [236].

Chapter 4

Gravitational Wave Emission from Collisions of Compact Scalar Solitons

The work presented in this chapter is derived from the paper "Gravitational Wave Emission from Collisions of Compact Scalar Solitons" [19], published in the Journal Physical Review D (PRD).

We numerically investigate the gravitational waves generated by the head-on collision of equal-mass, self-gravitating, real scalar field solitons (oscillatons) as a function of their compactness $\mathcal{C}$. We start with solitons that are initially at rest with respect to each other, and show that there exist three different possible outcomes resulting from their collisions: (1) an excited stable oscillaton for low $\mathcal{C}$, (2) a merger and formation of a black-hole for intermediate $\mathcal{C}$, and (3) a pre-merger collapse of both oscillatons into individual black-holes for large $\mathcal{C}$. For (1), the excited, aspherical oscillaton continues to emit gravitational waves. For (2), the total energy in gravitational waves emitted increases with compactness, and possesses a maximum which is greater than that from the merger of a pair of equivalent mass black-holes. The initial amplitudes of the quasi-normal modes in the post-merger ring-down in this case are larger than that of collisions of corresponding mass black-holes – potentially a key observable to distinguish black-hole mergers from their scalar mimics. For (3), the gravitational wave output is indistinguishable from a similar mass, black-hole–black-hole merger. Based on our results, LIGO may be sensitive to oscillaton collisions from light scalars of mass $10^{-12}\,\mathrm{eV} \lesssim m \lesssim 10^{-10}\,\mathrm{eV}$.

4.1 Introduction and Results

The spectacular recent detections of gravitational waves from binary black-hole mergers has heralded a new golden age in gravitational wave physics [5, 237, 238]. Gravitational waves from the merger of compact objects are one of our best resources for probing the strong-field regime of gravity. They also provide us with a probe of the nature of the compact objects themselves.

In addition to black-holes (BH) and neutron stars (NS), the expected quality of the gravitational wave data could allow for the search of exotic compact objects as progenitors in such collisions [85]. In particular, coherent, self-gravitating, non-topological solitons made of scalar fields are known to have highly compact cores [239, 10, 54]. Their collisions may generate observable amounts of gravitational waves and whose waveforms can deviate from those of BH-BH or NS-NS mergers (see in particular [83, 224, 14, 225]).

In this chapter, we study the head-on collisions of a class of *real* scalar field solitons called *oscillatons* [203] using `GRChombo` [134] in full general relativity. Unlike Boson stars made of complex scalar fields, oscillatons do not have a conserved $U(1)$ charge, but can nevertheless be stable on cosmological time scales [240]. For example, such objects can consist of a spatially localized condensate of an axion field oscillating near the minimum of the potential [17]. Such axion fields are ubiquitous in many high energy physics theories, and are considered to be plausible dark matter candidates (see [201] for a review).[1]

Our main result for the gravitational wave output from equal-mass oscillaton collisions as a function of the compactness of the solitons is shown in Fig. 4.1. In particular, the new results are: (1) a jump in the fractional gravitational wave output near a critical compactness value $\mathcal{C} \approx 0.14$, and (2) the fractional gravitational wave output near this $\mathcal{C}$ value exceeds that of corresponding mass black-holes. In order to achieve these results, we constructed *unexcited* oscillaton binaries which possess no spurious additional modes. Such "clean" initial conditions allow us to accurately extract the GW production efficiency $E_{\mathrm{gw}}/E_{\mathrm{tot}}$. Furthermore, we also compute the gravitational waveforms for such collisions to show that the quasi-normal modes are significantly different from equivalent BH-BH collisions during merger and in their ringdown phase, which suggests that they can be distinguished.

---

[1] We cannot claim that such compact soliton collisions are likely sources of gravitational waves; an estimate of their population and distribution would be needed, which is beyond the scope of this work. We hope that the results from this work will motivate such studies further.

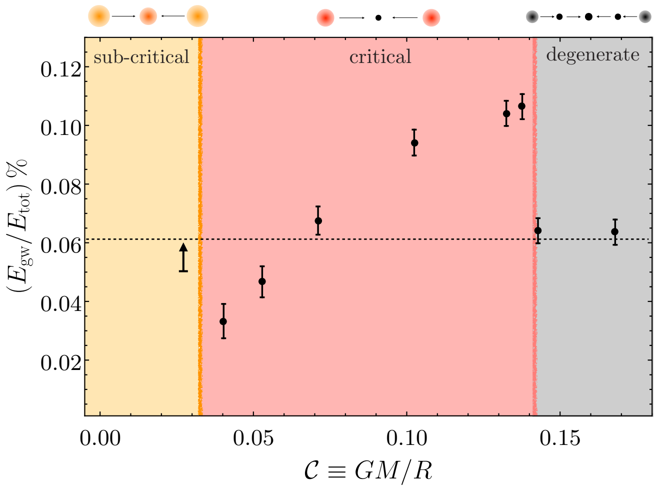

Fig. 4.1 Fraction of initial rest mass energy of the two oscillatons (E_{tot}) radiated into gravitational waves (E_{gw}) as a function of the initial compactness ($\mathcal{C}$) of each oscillaton. In the subcritical case, oscillatons collide to form a new stable but aspherical, excited oscillaton. In the critical regime, oscillatons collide to yield a black-hole after/during the collision. In the degenerate case, individual oscillatons collapse to black-holes before the collision. Note that in the critical regime (and possibly in the subcritical regime also), the emitted fraction in gravitational waves can exceed that of corresponding mass black-holes (0.06% dashed line).

4.2 Initial Set-Up of Solitons

We consider a free, massive, real scalar field, which is minimally coupled to gravity with the action[2]

$$S = \int d^4x\sqrt{-g}\left[\frac{R}{16\pi G} - \frac{1}{2}\partial_\mu\phi\partial^\mu\phi - \frac{1}{2}m^2\phi^2\right], \tag{4.1}$$

where g is the determinant of the metric, R is the Ricci scalar, and m is the mass of the real scalar field[3] ϕ. We briefly discuss self-interactions in the Appendix. Conservatively, the results are expected to apply for solitons made of a sub-dominant axionic dark matter component with the axion decay constant $f \gtrsim m_{\rm Pl}$. Assuming we have a scenario similar to [192], for $f \gtrsim m_{\rm Pl}$, the total dark matter abundance bound requires the axion to be unacceptably light ($m \lesssim 10^{-30}$ eV), in conflict with observations [201]. We further discuss this issue and possible solutions in the Appendix.

This theory contains a single parameter family of localized, solitonic solutions called oscillatons (once the mass m is scaled out). We choose to parametrize our solutions in terms

---

[2] We use the $-+++$ convention for the metric, and set $= c = 1$. Our Planck mass $M_{\rm Pl} = 1/\sqrt{G}$.

[3] We have ignored possible self-interactions of $\lambda\phi^3$ and higher order terms.

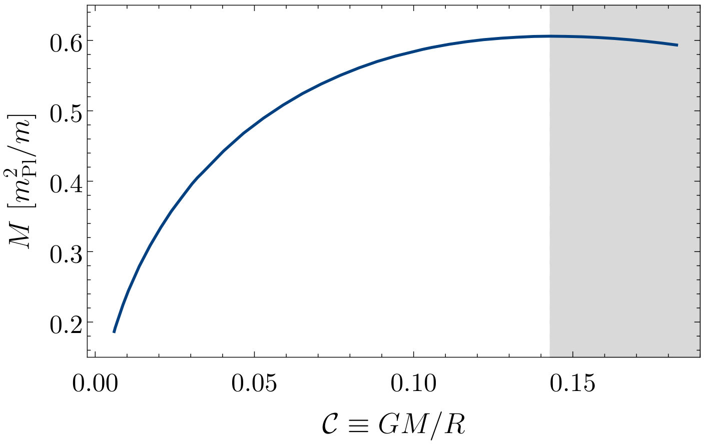

Fig. 4.2 **Relationship between the mass M and the compactness $\mathcal{C}$ of the oscillaton**. Note that for $\mathcal{C} \gtrsim 0.14$ ($M \approx 0.605 M_{\rm Pl}^2/m$) oscillatons become unstable under perturbations (grayed area).

of their *compactness*, which we define as

$$\mathcal{C} \equiv \frac{GM}{R}, \tag{4.2}$$

where M is the Arnowitt-Deser-Misner (ADM) mass, and R is the effective radius of the oscillaton which encompasses 95% of its mass. The maximum mass of the oscillaton $M_{\rm max} \approx 0.605 M_{\rm Pl}^2/m$ occurs when $\mathcal{C} \approx 0.14$. When $\mathcal{C} < 0.14$, the oscillatons are stable against perturbations. For $\mathcal{C} > 0.14$, they are unstable with respect to perturbations [55] (Fig. 4.2).

To ensure that these results are qualitatively and quantitatively robust, we implemented several steps such that the initial conditions for these oscillatons are in their unexcited "ground" state. We refer the reader to the Appendix for details of this construction, and other numerical convergence tests.

We set up two equal $\mathcal{C}$ (and hence equal mass) oscillatons at a distance of $60m^{-1}$, both of which are initially at rest, and explore the end-state of the collision and gravitational wave signature as a function of $\mathcal{C}$. These oscillatons can also have a relative phase $0 < \Delta\theta < \pi$ between their respective oscillations. Oscillatons are considered "in-phase" when $\Delta\theta = 0$; this is the scenario we focus on in this paper. "Out-of-phase" $\Delta\theta \neq 0$ oscillatons exhibit additional *repulsive* force that, at sufficiently large phase differences, prevents a merger from occurring. We will leave the results of out-of-phase initial conditions to a future publication.

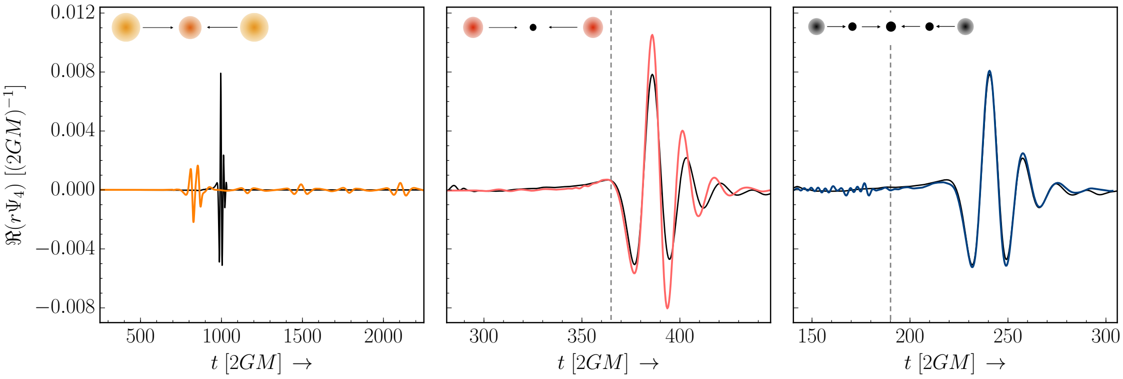

Fig. 4.3 **The panel shows the numerically evaluated gravitational wave waveforms** (the dominant quadrupole mode: $l = 2$, $m = 0$ is shown) for typical subcritical ($\mathcal{C} = 0.03$), critical ($\mathcal{C} = 0.10$) and degenerate ($\mathcal{C} = 0.15$) collisions. For comparison, the waveform for the corresponding mass black-hole collision is also shown in black. Note that in the sub-critical case (left panel), the resulting excited oscillaton continues to emit gravitational waves. In the critical case (middle panel), the waveform is qualitatively similar to a BH-BH merger, but importantly, the post-merger QNM amplitude is greater for the oscillaton merger as they are less "rigid". Since there is some mass loss during the merger, the final mass is less than that of the equivalent BH-BH merger, leading to a slightly shorter QNM period (as observed). Finally, the degenerate case is almost indistinguishable from a BH-BH collision (right panel). The vertical dashed line indicates time of BH formation during the merger in the critical case, and pre-merger in the degenerate case. Note that $r\Psi_4 \sim r\ddot{h}$, and $t = 0$ is associated with the time when the objects are $\approx 60m^{-1}$ apart. Movie links for the time evolution of the gravitational wave signal and the energy density ρ are available for the subcritical, critical and degenerate mergers [20–22].

4.3 Gravitational Waves from Collisions

We find that there are three possible outcomes of head-on collisions of equal mass solitons depending on the initial $\mathcal{C}$ of the oscillatons.

4.3.1 Subcritical Case $\mathcal{C} \lesssim 0.04$

Collisions of these less compact oscillatons form another more massive and quasi-stable, but aspherical and excited oscillaton. The merger proceeds via multiple stages. As we have shown in Fig. 4.4, the oscillatons collide and initially form a very perturbed oscillaton, whose density oscillates in a "+" pattern (i.e. periodically becomes elongated along two perpendicular axes). A significant amount of mass is lost during the initial collision. This mass loss can be inferred from the fact that $M(\mathcal{C} = 0.03) = 0.41M_{\text{Pl}}^2/m > 0.5M_{\text{max}}$ – this is consistent with the results first obtained in [86]. Without any mass loss, the final oscillaton in this case would have been unstable, which is not seen in our simulations. The oscillaton continues to radiate scalar waves and, notably, a long-time-scale continued emission of gravitational waves [85, 193].

From Fig. 4.4 and the first panel in Fig. 4.3, we see repeated alternating max/min bursts of gravitational waves coinciding with the maximum deformation of the perturbed oscillaton perpendicular-to/along the axis of collision. While the lack of computational resources prevented us from evolving this end state further in time, we expect that the continued emission of both scalar waves and GW will eventually sphericalize the oscillaton. This so-called “super-emitter” [193] will eventually emit more total GW energy than the corresponding equal-mass BH-BH merger. We have only found the lower bound on this GW energy output numerically.

4.3.2 Critical Case $0.04 \lesssim \mathcal{C} \lesssim 0.14$

These more massive and compact oscillatons collide to form a black-hole surrounded by a thin scalar field “wig". There is a slight mass loss during the collision, but the majority ($\approx 90\%$) of the initial mass remains in the final black-hole state. The total GW energy emitted by this merger monotonically scales with $\mathcal{C}$ in this regime. However, interestingly, for oscillatons with $\mathcal{C} > 0.06$, the fraction of the emitted gravitational wave energy[4] to the total initial energy, $E_{\text{gw}}/E_{\text{tot}}$, is *greater* than that from an equivalent head-on merger of a pair of equal mass black-holes ($E_{\text{gw}}/E_{\text{tot}} = 0.06\%$). The maximum gravitational wave energy emitted $E_{\text{gw}}/E_{\text{tot}} \approx 0.11\%$ occurs at $\mathcal{C} \approx 0.14$, the boundary where the individual oscillatons themselves become unstable.

A typical waveform of the merger from this region is shown in the middle panel of Fig. 4.3. Black-hole formation occurs rapidly after the initial merger. For less compact oscillatons, not surprisingly, the scalar dynamics during merger will lead to different GW waveforms that distinguishes it from that of a BH-BH merger [85, 225]. Crucially however, even for very compact oscillatons where BH formation is very rapid, the waveform differs from that of a BH-BH collision even in the post-merger ringdown stages. The quasi-normal mode (QNM)

---

[4] This energy is computed by integrating over time the total power given by

$$\frac{dE_{\text{gw}}}{dt} = \lim_{r\to\infty} \frac{r^2}{16\pi} \oint \left| \int_{-\infty}^{t} \Psi_4(r)\, dt' \right|^2 d\Omega, \tag{4.3}$$

where Ψ_4 is the Newman-Penrose scalar. For our simulations the extraction radius $r = 60m^{-1}$. Moreover, $E_{\text{tot}} = 2M$, i.e. total initial ADM mass of the oscillatons.

frequency during the ring down is close to that of a BH-BH merger (as expected) with a shorter period due to mass loss during merger. Importantly, the initial amplitude of the QNM is different. In particular, we find that for $\mathcal{C} \gtrsim 0.06$ the initial QNM amplitude is *larger* than that of an equal mass BH-BH merger leading to the aforementioned higher output in total GW emission (see Fig. 4.1).

We believe that this higher initial amplitude for the QNM is due to the fact that oscillatons are "less rigid" than black-holes, and hence easier to excite during the initial merger phase.

Interestingly, in [85], the authors argue instead that collisions of more massive Boson stars will lead to a more rapid collapse into BHs and hence to a smaller deviation from a BH-BH merger. Our results here show that the deviation is *more* significant for oscillatons, allowing us to directly test for such non-BH merger scenarios.[5]

4.3.3 Degenerate Case $\mathcal{C} > 0.14$

Oscillatons with $\mathcal{C} > 0.14$ are inherently unstable to perturbations. We find that as they fall towards one another, mutual tidal forces generate sufficient perturbations to cause the oscillatons to collapse into a pair of BHs before they collide. The new BHs (with a thin wig) then collide and merge as in the standard BH-BH case to form a larger black-hole. The waveform (see rightmost panel of Fig. 4.3) and the fraction of energy in gravitational waves is indistinguishable from the BH case and remains constant as we continue to increase the compactness (see Fig. 4.1). This expected behavior in the degenerate case makes for a strikingly steep transition in the emitted gravitational wave energy from the critical to the degenerate regime (near $\mathcal{C} \approx 0.14$, see Fig. 4.1).

4.4 Discussion and Future Directions

Our main results can be seen in Fig. 4.1 and Fig. 4.3. Through detailed calculations using the full power of numerical GR, we showed that oscillaton head-on mergers have distinctly different GW signatures than that of their corresponding equal mass BH-BH counterparts. We found three different outcomes of collisions depending on the initial compactness of the oscillatons: formation of excited oscillatons (sub-critical), formation of a black-hole after

---

[5] Furthermore we note that while Boson star mergers can be qualitatively similar to our oscillaton mergers, there are differences. For example, a collision between a Boson star and anti-Boson star can lead to annihilation, with a dispersal of most of the field to infinity [84]. Analogs of Boson star/anti-Boson star pairs are not present in the oscillaton merger case. Note that an initial phase difference between pre-merger oscillatons cannot mimic these configurations.

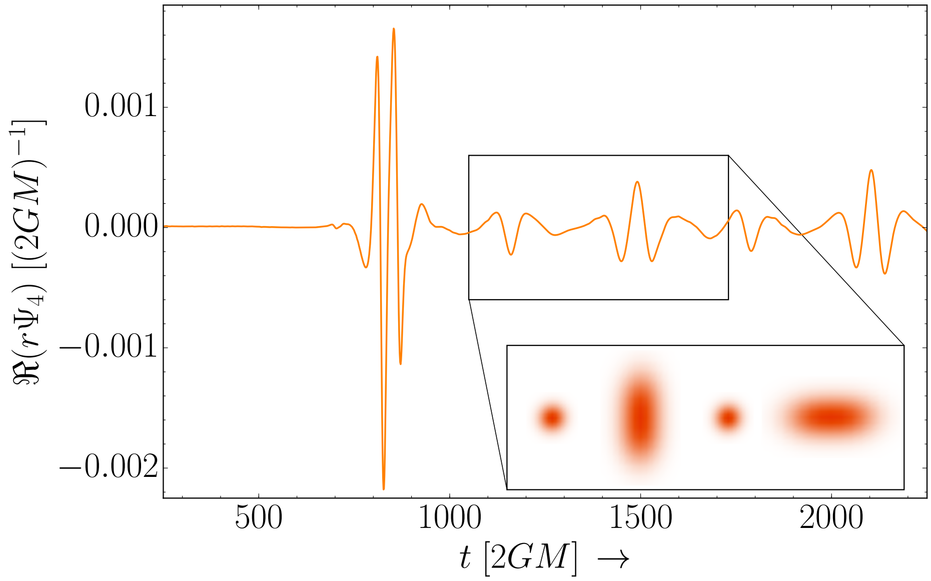

Fig. 4.4 **Numerically evaluated gravitational wave waveform for a typical subcritical ($\mathcal{C} = 0.03$) collision**, demonstrating bursts of repeating gravitational waveforms. Inset shows the "$+$" pattern of oscillations of the density of the perturbed final state.

collision (critical) and formation of black-holes before collision (degenerate) due to tidal forces.

In terms of gravitational waves, the subcritical merger results in a potentially long lived source of gravitational waves. The gravitational waveform is qualitatively different from the Black hole merger case with multiple post merger pulses. For the degenerate case, the dynamics and gravitational wave signatures are very similar to that of corresponding mass black-holes.

Most interestingly, for critical mergers where the final state is a BH, the post-merger QNM mode has a significantly larger amplitude than that of an equivalent BH-BH merger (for sufficiently compact oscillatons). We believe that this is due to the fact that oscillatons are less rigid and easier to excite than BHs. This raises the possibility that, without inspiral GW information, compact oscillatons mergers may mimic BH mergers of a larger mass, though QNM frequency information will allow us to break this degeneracy. Conversely with inspiral information, this may provide a distinct GW signature for the detection of such exotic compact objects. If these results carry through to inspiral mergers, the ratio of the GW amplitude during the inspiral phase and the ringdown phase will be a strong indicator of exotic mergers. While these are plausible arguments, we admit that more work is needed in the inspiral case to make a convincing argument regarding observationally distinguishing BH-BH mergers from OS-OS ones.

For the cases checked (in head-on collisions), we found that the fraction of energy density in gravitational waves is relatively independent of the initial separation of the solitons (within numerical error, we confirmed this for separations of $40m^{-1}$, $55m^{-1}$ and $65m^{-1}$ in the critical and degenerate regimes). The critical-degenerate boundary in Fig. 4.1 is similarly robust, suggestive of some novel criticality in terms of the dynamics and the gravitational wave output near $\mathcal{C} \approx 0.14$, which is worth investigating in detail. Further investigation of this criticality by scanning through different initial velocities, relative phases and a larger variance in distances is needed.

Assuming that our oscillatons are stellar mass so that their QNM frequencies fall within LIGO range, this allows us to probe light oscillaton masses of $10^{-12}\,\mathrm{eV} \lesssim m \lesssim 10^{-10}\,\mathrm{eV}$. On the other hand, interactions of free scalar fields with rotating Black holes can cause a superradiance instability, robbing the blackholes of their spin – LIGO (LISA) observations of stellar mass (supermassive) spinning Black holes can potentially rule out $10^{-13} \lesssim m \lesssim 10^{-12}$ eV ($10^{-19} \lesssim m \lesssim 10^{-17}$ eV) [223].

In conclusion, we have found that in head-on collisions, compact scalar field solitons can be louder in gravitational waves than their black-hole counterparts. Moreover, a new critical transition in the GW amplitude is seen at $\mathcal{C} \approx 0.14$. It will be interesting to see if these results are replicated in the inspiral case (e.g. [225]), which we are currently investigating.

Chapter 5

Cosmic String Loop Collapse in Full General Relativity

The work presented in this chapter is derived from the paper “Cosmic String Loop Collapse in Full General Relativity” [241], published in the Journal Physical Review D (PRD).

We present the first fully general relativistic dynamical simulations of Abelian Higgs cosmic strings using 3+1D numerical relativity. Focusing on cosmic string loops, we show that they collapse due to their tension and can either (i) unwind and disperse or (ii) form a Black hole, depending on their tension $G\mu$ and initial radius. We show that these results can be predicted using an approximate formula derived using the hoop conjecture, and argue that it is independent of field interactions. We extract the gravitational waveform produced in the Black hole formation case and show that it is dominated by the $l = 2$ and $m = 0$ mode. We also compute the total gravitational wave energy emitted during such a collapse, being 0.5 ± 0.2 % of the initial total cosmic string loop mass, for a string tension of $G\mu = 1.6 \times 10^{-2}$ and radius $R = 100\ M_{\rm Pl}^{-1}$. We use our results to put a bound on the production rate of planar cosmic strings loops as $N \lesssim 10^{-2}$ Gpc^{-3} yr^{-1}.

5.1 Introduction

The recent detection of Gravitational Waves (GW) from Black hole (BH) [5] binaries by the LIGO/VIRGO collaboration marked the start of a new era of observations. Beyond astrophysical objects such as BH and neutron stars, this paved the way for the use of GW to search directly for signatures of new physics. One of the key targets for this search are cosmic strings [242, 9, 243].

Cosmologically, cosmic string networks naturally arise after a phase transition in the early universe, possibly during GUT symmetry breaking. More speculatively, string theory also suggests the presence of cosmological fundamental superstrings, especially through the mechanism of brane inflation [244, 245]. These networks may manifest themselves through several channels, such as imprints via lensing on the Cosmic Microwave Background [246] and possibly through the presence of a stochastic gravitational wave background. The latter in particular is recently searched for by the LIGO/VIRGO collaboration [9]. More intriguingly, one can search for localized coherent events of these strings, such as when the strings self-interact through the formation of sharp cusps or through the collisions of traveling kinks that are formed during the intercommutation (i.e. collisions) of cosmic strings.

Before this work, the two primary methods of modeling cosmic strings has been through solving the field theory equations in flat or expanding spacetime, or through an effective Nambu-Goto prescription with weak coupling to gravity (see e.g. [247]). In either case, by considering the stress-energy of a network of strings, one can then compute in the weak gravity limit a stochastic GW background [248, 249]. Local events such as the collisions of traveling kinks and cusps along the strings are expected to produce bursts of GW – these bursts events have been computed using the Nambu-Goto approximation, again in the weak field limit [249]. These two methods do not coincide in general, mainly due to their disagreement on the primary energy loss mechanism of the cosmic strings (see [250–255]).

Going beyond the weak field limit requires the finding of the solutions to the full field theory coupled to general relativity – and in this work we present the *first numerical relativity simulation of Abelian Higgs cosmic strings in full general relativity*. We numerically explore the collapse of a circular cosmic string loop in extreme regimes ($4\times10^{-3} < G\mu < 4\times10^{-2}$). We show that whether the loop collapses into a BH or unwinds itself depends on a simple analytic relation derived using the hoop conjecture. In the former case, we computed both the gravitational waveform (fig. 5.1) and its integrated GW energy emitted from such a collapse. For the latter, we found that the total energy emitted in gravitational waves is 0.5 ± 0.2 % of the initial mass, which is in agreement with the bound of $< 29\%$ [256].We will discuss direct detection prospects of such individual collapse events with GW detectors in section 5.5.

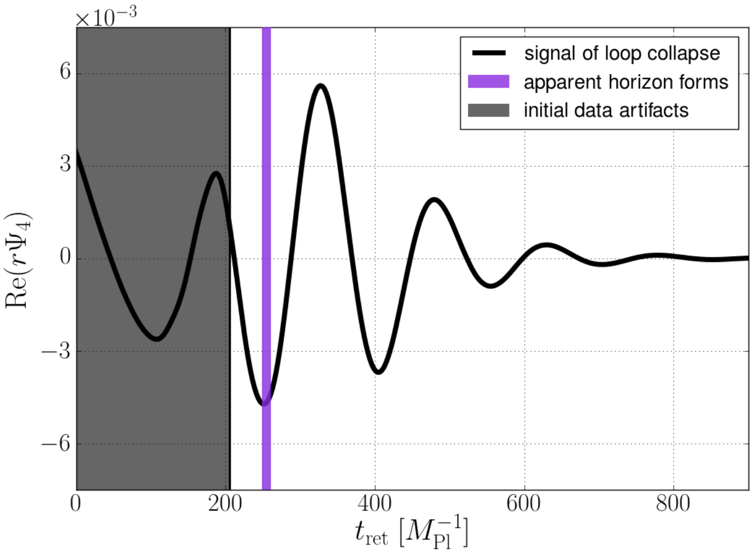

Fig. 5.1 **GW for a BH formed from circular cosmic string loop collapse:** We plot the real part of the dominant $l = 2$ $m = 0$ mode of $r\Psi_4$ over time. The loop has tension $G\mu = 1.6 \times 10^{-2}$ and an initial radius $R = 100\, M_{\rm Pl}^{-1}$. The grey shaded area of the plot are mixed with stray GWs that arise as artifacts of the initial data. The x-axis $t_{\rm ret} = t - r_{\rm ext}$ is the retarded time where $r_{\rm ext}$ is the extraction radius.

5.2 Abelian Higgs with Gravity

The action of the Abelian Higgs model minimally coupled to gravity [1]

$$S = S_{EH} - \int d^4x\sqrt{-g}\left[(D_\mu\phi)^*(D^\mu\phi) + \frac{1}{4}F_{\mu\nu}F^{\mu\nu} + V(\phi)\right] , \tag{5.1}$$

where $S_{EH} = \int dx^4\sqrt{-g}(R/16\pi G)$, D_μ is the covariant derivative $(\partial_\mu - ieA_\mu)$ with its $U(1)$ gauge field A^μ, and $V(\phi)$ is the potential of the complex scalar field ϕ given by

$$V(\phi) = \frac{1}{4}\lambda\left(|\phi|^2 - \eta^2\right)^2 , \; F_{\mu\nu} = \partial_\mu A_\nu - \partial_\nu A_\mu . \tag{5.2}$$

For simplicity, we set the charge e and the dimensionless coupling constant λ to obey the critical coupling limit

$$\beta = \frac{\lambda}{2e^2} = 1 , \tag{5.3}$$

---

[1] We use the $-+++$ convention for the metric, and set $= c = 1$ and $M_{\rm Pl} = 1/\sqrt{G}$.

in which the Higgs and vector masses are identical and μ simplifies to

$$\mu = 2\pi\eta^2 \ . \tag{5.4}$$

As a check of our code, we numerically construct a fully relativistic infinite static string coupled to gravity and demonstrate that its evolution is indeed static and stable. The details of this construction can be found in Appendix D.2.

We consider circular string loops. To construct the initial conditions, we define toroidal coordinates

$$\begin{aligned} x &= \cos\varphi(R + r\cos\theta) \ , \\ y &= \sin\varphi(R + r\cos\theta) \ , \\ z &= r\sin\theta \ , \end{aligned} \tag{5.5}$$

where R is the radius of the loop and choose the following ansatz for the field variables

$$\phi = f(r)e^{in\theta} \ , \ A_\theta = \frac{n\alpha(r)}{e} \ , \tag{5.6}$$

where n is the winding number of the string which is set to one throughout this paper. To construct the loop we use the profile $f(r)$ from the static string[2]. After making the conformal metric ansatz

$$\gamma_{ij}dx^i dx^j = \chi(dx^2 + dy^2 + dz^2) \ , \tag{5.7}$$

we solve the Hamiltonian constraint to obtain the conformal factor χ.

5.3 Results

We simulate the collapse of circular loops, scanning through the initial condition parameter radius R and the model symmetry-breaking scale η (and hence string tension via Eq. 5.4), in the critical coupling limit with $e = 1$ and $\lambda = 2$. The loop begins at rest but quickly accelerates to close to the speed of light due mainly to the string tension. We find this motion to be consistent with the Nambu-Goto action dynamics (see Appendix D.3)

$$r = R\cos\frac{\tau}{R} \ , \tag{5.8}$$

---

[2] See Appendix D.2 for details.

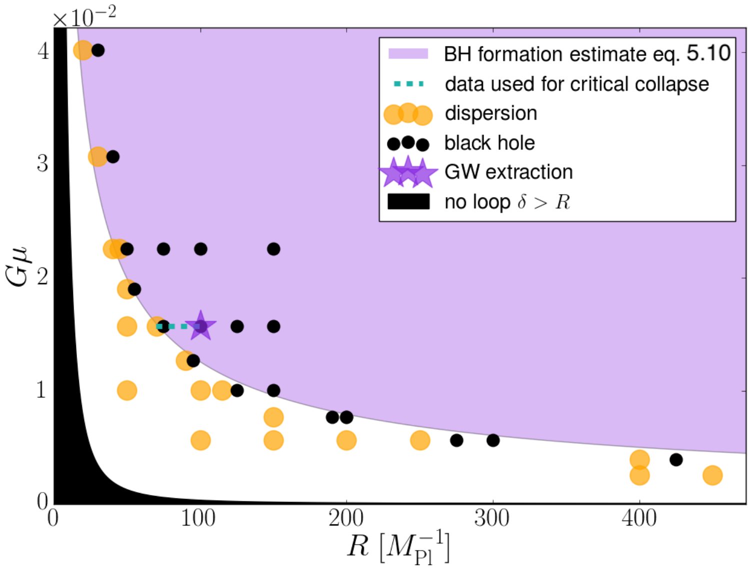

Fig. 5.2 **Overview of simulations :** The loop can either form a BH or unwind and radiate all its mass. The analytical expression derived from the hoop conjecture accurately predicts the outcome. Movie links for the evolution over time of the collapse are available for the dispersion [23] and Black hole [24] cases.

up to $r \sim \delta$ which is the thickness of the string given by

$$\delta = \frac{1}{\eta\sqrt{\lambda}}\,, \tag{5.9}$$

and τ is the time coordinate at spatial infinity. Depending on the choice of μ and R, there are two possible outcomes: (i) the string unwinds itself and the resulting radiation disperses or (ii) a BH forms.

This result can be predicted using the hoop conjecture as follows. A BH forms if the loop mass $M_{\rm loop} = 2\pi\mu R$ is enclosed within a radius smaller than its Schwarzschild radius $2GM_{\rm loop}$. In addition, the smallest volume in which a loop can be contained before the string unwinds has radius δ, which sets the Schwarzschild radius the lower bound for BH formation to be $2GM_{\rm loop} > \delta$, or

$$R > \sqrt{\frac{1}{8\pi\lambda}}(G\mu)^{-3/2}M_{\rm Pl}^{-1}\,. \tag{5.10}$$

Moreover, as the minimum radius of a loop is $R = \delta$, we don't expect dispersion cases for $G\mu > (4\pi)^{-1}$ and all loops will form BHs. We find this estimate to be a good predictor (see fig. 5.2), which suggests that Black hole formation is broadly independent of field interactions.

If a Black hole forms, the amount of initial mass that falls into the Black hole depends on the initial radius R for fixed $G\mu$, with the rest being radiated in either gravitational waves or matter.

We investigate whether this collapse is a Type I or Type II transition [183] by studying the mass of the Black hole close to the critical radius. Supposing it is a Type II collapse and let R_* be the critical point such that $M_{\rm BH}(R_*) = 0$, one can compute the critical index γ defined by

$$M_{\rm BH} \propto (R - R_*)^{\gamma} \,. \tag{5.11}$$

The value asumming the theoretical prediction of Eq. 5.10, $R_*^{\rm th} = \sqrt{1/8\pi\lambda}(G\mu)^{-3/2}M_{\rm Pl}^{-1}$, is $\gamma = 0.39$, see fig. 5.3. However, in our simulations we have observed $R_*^{\rm ob} > R_*^{\rm th}$, giving $\gamma = 0.17$, showing that γ is highly dependent on the choice of the actual value of R_* – of which we are unable to identify with confidence due to the lack of computational resources. Therefore, we conclude that $\gamma = 0.28 \pm 0.11$.

In the subcritical limit where $2GM_{\rm loop} < \delta$, the loop unwinds as it collapses, transferring all the mass into matter and gravitational radiation. If $R \gg \delta$ the velocity at unwinding is much larger than the escape velocity and all the energy is radiated away. However, if $R \sim \delta$, the velocity can be small enough so that instead of full dispersal the mass slowly decays at the center and a soliton might form.

5.4 Gravitational Waves from Black hole formation

We compute the gravitational waveform from the collapse of a loop with $G\mu = 1.6 \times 10^{-2}$ and $R = 100\ M_{\rm Pl}^{-1}$ into a Black hole, fig. 5.1. Post formation of the apparent horizon, the waveform exhibits the characteristic quasi-normal mode decay, with the dominant mode being the $l = 2, m = 0$ mode as usual. We found the integrated energy of the signal to be

$$\varepsilon \equiv \frac{E_{\rm GW}}{M_{\rm loop}} = 0.5 \pm 0.2\ \% \,. \tag{5.12}$$

The error bars come primarily from the presence of the spurious modes from the initial data mixing in with the early part of the collapse (grey area in fig. 5.1). Even though the velocity of the loop at collision is ultra-relativistic, $\sim 0.99\ c$, the GW production is strongly suppressed when compared to other ultra-relativistic events. For comparison, a boosted head-

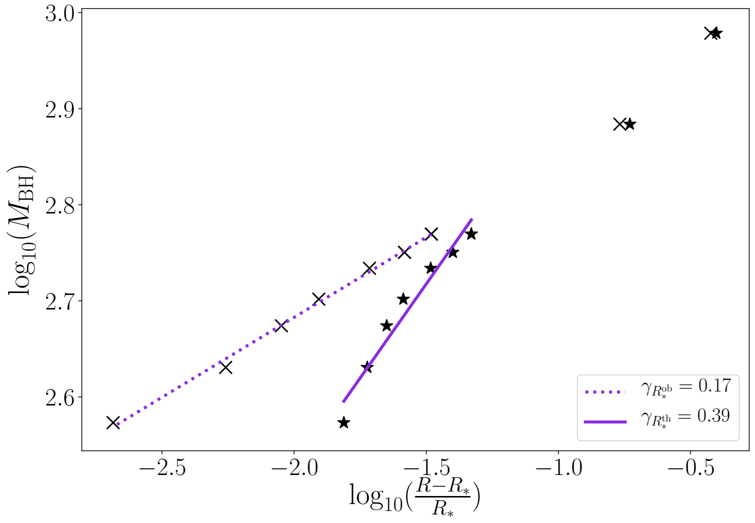

Fig. 5.3 **Critical collapse**: We plot the logarithm of the mass of the Black hole vs the logarithm of the difference between the initial and the theoretical(star)/observed(cross) critical radius for $G\mu = 1.6 \times 10^{-2}$. As we argued in the text, our simulation showed that the actual $R_*^{\rm ob} > R_*^{\rm th}$, resulting in a critical index within $0.17 < \gamma < 0.39$, where the error is due to the uncertainty in determining numerically $R_*^{\rm th} < R_* < R_*^{\rm ob}$. Note that we only use the first 7 points to compute the critical index for $R \leq 0.05R_*$ as the critical relation is only expected to hold perturbatively.

on Black hole merger ($14 \pm 3\%$) and relativistic fluid particle collapse ($16 \pm 2\%$) radiates a much larger fraction of its total mass in gravitational waves [257, 258]. This suggests that the initial apparent horizon is very spherical – possibly due to the thickness of our strings when compared to the Schwarzschild radius, i.e. $2GM_{\rm loop} \sim \mathcal{O}(1) \times \delta$. In the limit of infinitisimally thin strings, the maximum GW production was calculated by Hawking to be 29% [256]. Hence, we believe that one can boost the efficiency by colliding thinner strings (i.e. $2GM_{\rm loop} \gg \delta$) – in this limit the hoop conjecture argument above suggests that a Black hole will form before the loop has a chance to interact and unwind, thus it is possible that the GW emission will be larger via Hawking's argument, though this has not been demonstrated numerically.

Finally, loops in general are generated non-circularly with many different oscillating stable configurations. Nevertheless, in the presence of gravity, we expect gravity to eventually win out, with roughly the timescale of their gravitational collapse to be the free-fall time-scale. In the final stages of collapse, we expect the tension to circularize the loops and thus our results might also for more general initial data.

5.5 Discussion and detection prospects

We have extracted the gravitational wave signal for the case $G\mu = 1.6 \times 10^{-2}$, and $R = 100\, M_{\rm Pl}^{-1}$ and found that the efficiency $\varepsilon = 0.5 \pm 0.2$ % of the initial mass is radiated into gravitational waves. The QNM frequency of our GW waveform (fig. 5.1) is in the UV range and out of any current or future detectors. On the other hand, if we assume that our numerical results scale, we can ask whether we can detect suitably massive cosmic strings loops with current or future detectors. The two key parameters are (i) the frequency and (ii) the luminosity of the event, both which depend on the masses. The former constrains our loop parameter space to $2\pi\mu R \approx M_{detector}$. We choose $M_{detector}$ such that its frequency lies at peak sensitivity of LIGO/VIRGO ($f \sim\ 100Hz$). For the latter, the strain h observed at a distance d from a source of GWs is

$$\left(\frac{h}{10^{-21}}\right) \sim \sqrt{\frac{E_{\rm GW}}{3\times 10^{-3} M_\odot}} \left(\frac{10\ {\rm Mpc}}{d}\right) . \tag{5.13}$$

Cosmic strings loops are generated during the evolution of the string network when strings intercommute, although there is presently no consensus on the probability distribution of loops and their classification (see e.g. [259, 260]). Furthermore, it is not clear that all loops will collapse due to the presence of non-intersecting loop configurations and the uncertainty in their angular momentum loss mechanisms. Hence, we will take the agnostic view that only planar loops will collapse – assuming that planar loops will circularize as argued by [261]. Suppose then $N(R,z)$ is the co-moving production density rate of planar loops of radius R at redshift z (i.e. it has dimensions $[N(R,z)] = L^{-3}T^{-1}$), then the detection rate is given by

$$\Gamma = \int_0^{z_d} 4\pi \left[\int_0^z \frac{dz'}{H(z')}\right]^2 \frac{N(r,z)dz}{H(z)} \ , \ d = \int_0^{z_d} \frac{dz}{(1+z)H(z)} . \tag{5.14}$$

such that z_d is the maximum range in redshift of the detector, which itself depends on the energy of the GW $E_{\rm GW}$ emitted. Our numerical results Eq. 5.12 suggest that 0.5% of the total string loop mass is emitted, which is an order of magnitude smaller than that of the typical BH-BH mergers, translating to about a factor of 3 shorter in detectable distance d. For LIGO/VIRGO and ET, the maximum redshift range is then $z_d \sim 0.005$ and $z_d \sim 0.05$ respectively. In this limit, Γ can be approximated as

$$\Gamma \approx \varepsilon^{3/2} \left(\frac{R}{GM_\odot}\right)^{3/2} (G\mu)^{3/2} \left(\frac{10^{-19}}{h}\right)^3 \left(\frac{N(R,z)}{{\rm Mpc}^{-3}}\right) . \tag{5.15}$$

Clearly, Γ depends linearly on $N(R,z)$, which itself depends on the cosmic string model and its network evolution, which at present is still being debated vigorously as mentioned above. For example, in [261], it was estimated that $N(R,z) \propto (G\mu)^{2R/s-4}$ where s is the correlation length of the loop. Other estimates are given in [262, 263]. On the other hand, we can use the non-detection of such collapse events in the present LIGO/VIRGO to put a constraint on $N(R,z)$. For $G\mu \sim 10^{-10}$ which leads to solar system sized loops of $R \sim \mathcal{O}(100)$ a.u., this is $N(R,z) < 10^{-2}$ Gpc^{-3} yr^{-1}, which is a lower detection rate than what is expected from BH mergers of $\mathcal{O}(10)$ Gpc^{-3} yr^{-1} [264].

Finally, we note that this is a conservative estimate since these solar system sized loops satisfy $R_{\mathrm{BH}} \sim \mathcal{O}(10^{40}) \times \delta$ and hence are thin loops. In this limit, ε might be closer to 29 %, with a corresponding increase in d. We will numerically investigate the collapse of these thin loops in a future work.

Chapter 6

Conclusions

6.1 Summary

In chapters 2, 3 and 4 we studied Axion stars [19, 17, 190]. We discussed their formation in chapter 3, end-of-life in chapter 3 and emitted signals in a merger in chapter 4. In chapter 5 we discussed gravitational waves from collapsing cosmic string loops.

Chapter 2 focused on Axion stars [17]. We find that due to the axion potential

$$V(\phi) = m_a^2 f_a^2 \left[1 - \cos\left(\frac{\phi}{f_a}\right)\right] \tag{6.1}$$

an instability develops which can either collapse the Axion star into a Black hole, or disperse its content to infinity. We studied the solution space, Fig. 2.1, parameterized by the axion decay constant, f_a, and the initial ADM mass, M_{ADM}, of a one parameter family of initial conditions.

In chapter 3 [190] we discussed the formation of such objects with non-spherical initial data

$$\phi = \varphi \left(\cos(k_\star x) + \cos(k_\star y) + \cos(k_\star z)\right) \ . \tag{6.2}$$

for selfinteraction $f = 0.5\,M_{\text{Pl}}$ and $5\,M_{\text{Pl}}$. We find that, depending on the initial mass, we form either Oscillatons or Black holes where most of the mass is in final object. With further analysis we are able to determine the populations of boson stars and Black holes and find a mass-gap for $f_a < 0.2 M_{\text{Pl}}$ [1] which could be detected by LIGO/VIRGO for axion masses of $10^{-9} eV < m_a < 10^{-10} eV$.

---

[1] $M_{\text{Pl}} = \frac{1}{\sqrt{8\pi G}}$ for all of chapter 3

In chapter 4, we studied the merger of oscillatons, where we found three different types of merger dubbed subcritical, critical and degenerate mergers. A subcritical merger forms a stable boson star as a final product, a critical merger formed a Black hole as a final product and a degenerate merger collapsed each star collapsed into a Black hole even before they merge.

In chapter 5 [241] we studied cosmic strings in full numerical general relativity for the first time. More specifically, we study the collapse of a ring of a cosmic string and the possible outcomes, as well as the radiated gravitational waves (see movie).

6.2 Future work

In planned research, we hope to gain a better understanding of the final state of a boson star merger and the formation of rotating state and their nature. Furthermore, we hope to further improve initial data even further for binary systems.

We will extend our study of the dynamics of cosmic strings, to that of a cosmic string cusps and study their collisions to produce large GWs. We will generate the initial data by constructing travelling waves as in [265]. This construction does give solutions of cosmic string travelling waves in their minimum energy state without any constraint violations. Ultimately, we hope to construct the necessary theory and numerical infrastructure to characterise the GW signatures from a wide range of cosmic string phenomena, in order to enable a waveform search by GW detectors.

We intend to study superradiance, an effect where bosonic particles interact violently with the spin of Black holes. This phenomenon can reduce the spin of Black holes if axions exist, thus giving us a way of discovering them. This is a technically difficult phenomenon to simulate because of the vast hierarchy in the timescales of BH and scalar fields. We plan to mitigate this problem by ignoring the loss of spin from the Black hole, which reduces the complexity of the problem and allows us to simulate for longer. This would allow us to study the stability of this process under more realistic conditions. By running these simplified scenarios, we hope to develop the technical tools to make fewer assumptions. Our goal ultimately is to understand if superradiance can happen under realistic conditions.

References

[1] M. J. Turk *et al.*, The Astrophysical Journal Supplement Series **192**, 9 (2011), 1011.3514.

[2] J. D. Hunter, Computing In Science & Engineering **9**, 90 (2007).

[3] E. Jones *et al.*, SciPy: Open source scientific tools for Python, 2001.

[4] S. G. Hahn and R. W. Lindquist, Annals of Physics **29**, 304 (1964).

[5] LIGO Scientific Collaboration and Virgo Collaboration, B. P. Abbott, Phys. Rev. Lett. **116**, 061102 (2016).

[6] J. G. Baker, J. Centrella, D.-I. Choi, M. Koppitz, and J. van Meter, Phys. Rev. Lett. **96**, 111102 (2006), gr-qc/0511103.

[7] F. Pretorius, Phys. Rev. Lett. **95**, 121101 (2005), gr-qc/0507014.

[8] M. Campanelli, C. O. Lousto, P. Marronetti, and Y. Zlochower, Phys. Rev. Lett. **96**, 111101 (2006), gr-qc/0511048.

[9] Virgo, LIGO Scientific, B. Abbott *et al.*, Phys. Rev. **D97**, 102002 (2018), 1712.01168.

[10] M. Colpi, S. L. Shapiro, and I. Wasserman, Phys. Rev. Lett. **57**, 2485 (1986).

[11] P. Jetzer and J. V. D. Bij, Physics Letters B **227**, 341 (1989).

[12] R. Brito, V. Cardoso, C. A. R. Herdeiro, and E. Radu, Phys. Lett. **B752**, 291 (2016), 1508.05395.

[13] P. Grandclément, C. Somé, and E. Gourgoulhon, Phys. Rev. D **90**, 024068 (2014).

[14] N. Sennett, T. Hinderer, J. Steinhoff, A. Buonanno, and S. Ossokine, Phys. Rev. **D96**, 024002 (2017), 1704.08651.

[15] H. Olivares *et al.*, (2018), 1809.08682.

[16] G. F. Giudice, M. McCullough, and A. Urbano, JCAP.**10**, 001 (2016), 1605.01209.

[17] T. Helfer *et al.*, JCAP **1703**, 055 (2017), 1609.04724.

[18] F. Michel and I. G. Moss, (2018), 1802.10085.

[19] T. Helfer, E. A. Lim, M. A. G. Garcia, and M. A. Amin, Phys. Rev. **D99**, 044046 (2019), 1802.06733.

[20] GRChombo, Subcritical merger, 2018, https://youtu.be/ri2jkxA-a-o.

[21] GRChombo, Critical merger, 2018, https://youtu.be/FHYvFCSwcaY.

[22] GRChombo, Degenerate merger, 2018, https://youtu.be/R6Hz2Q4FbIU.

[23] GRChombo, Dispersion - cosmic string loop collapse in full gr, 2018, https://youtu.be/nHH3gTEjMPo.

[24] GRChombo, Black hole formation - cosmic string loop collapse, 2018, https://youtu.be/U5CkThsDU6w.

[25] GRChombo, Unfixed radial mode in oscillaton, 2018, https://youtu.be/h0MXVNd8u2E.

[26] GRChombo, Fixed radial mode in oscillaton, 2018, https://youtu.be/W95UkprupyA.

[27] S. Bonazzola and F. Pacini, Phys. Rev. **148**, 1269 (1966).

[28] D. J. Kaup, Phys. Rev. **172**, 1331 (1968).

[29] R. Ruffini and S. Bonazzola, Phys. Rev. **187**, 1767 (1969).

[30] V. Cardoso and P. Pani, Living Rev. Rel. **22**, 4 (2019), 1904.05363.

[31] S. L. Liebling and C. Palenzuela, Living Rev. Rel. **15**, 6 (2012), 1202.5809, [Living Rev. Rel.20,no.1,5(2017)].

[32] F. E. Schunck and E. W. Mielke, Class. Quant. Grav. **20**, R301 (2003), 0801.0307.

[33] P. Jetzer, Physics Reports **220**, 163 (1992).

[34] A. R. Liddle and M. S. Madsen, Int. J. Mod. Phys. **D1**, 101 (1992).

[35] E. W. Mielke and F. E. Schunck, Boson and axion stars, in *Recent developments in theoretical and experimental general relativity, gravitation and relativistic field theories. Proceedings, 9th Marcel Grossmann Meeting, MG'9, Rome, Italy, July 2-8, 2000. Pts. A-C*, pp. 581–591, 2000.

[36] E. W. Mielke and F. E. Schunck, Boson stars: Early history and recent prospects, in *Recent developments in theoretical and experimental general relativity, gravitation, and relativistic field theories. Proceedings, 8th Marcel Grossmann meeting, MG8, Jerusalem, Israel, June 22-27, 1997. Pts. A, B*, pp. 1607–1626, 1997, gr-qc/9801063.

[37] S. Doeleman *et al.*, Nature **455**, 78 (2008), 0809.2442.

[38] K. Akiyama *et al.*, Astrophys. J. **807**, 150 (2015), 1505.03545.

[39] C. Goddi *et al.*, Int. J. Mod. Phys. **D26**, 1730001 (2016), 1606.08879, [1,863(2017)].

[40] S. H. Hawley and M. W. Choptuik, Phys. Rev. **D67**, 024010 (2003), gr-qc/0208078.

[41] M. Choptuik, R. Masachs, and B. Way, (2019), 1904.02168.

[42] M. Gleiser, Phys. Rev. D **38**, 2376 (1988).

[43] P. Jetzer, Nuclear Physics B **316**, 411 (1989).

[44] E. Seidel and W.-M. Suen, Phys. Rev. D **42**, 384 (1990).

[45] F. S. Guzmán, Phys. Rev. D **70**, 044033 (2004).

[46] F. S. Guzman, Rev. Mex. Fis. **55**, 321 (2009), 1907.08193.

[47] J. Balakrishna, E. Seidel, and W.-M. Suen, Phys. Rev. **D58**, 104004 (1998), gr-qc/9712064.

[48] P. Amaro-Seoane, J. Barranco, A. Bernal, and L. Rezzolla, JCAP **1011**, 002 (2010), 1009.0019.

[49] T. D. Lee, Phys. Rev. D **35**, 3637 (1987).

[50] R. Friedberg, T. D. Lee, and Y. Pang, Phys. Rev. D **35**, 3658 (1987).

[51] F. E. Schunck and D. F. Torres, Int. J. Mod. Phys. **D9**, 601 (2000), gr-qc/9911038.

[52] S. Yoshida and Y. Eriguchi, Phys. Rev. D **56**, 762 (1997).

[53] D. Pugliese, H. Quevedo, J. A. Rueda H., and R. Ruffini, Phys. Rev. **D88**, 024053 (2013), 1305.4241.

[54] E. Seidel and W. M. Suen, Phys. Rev. Lett. **66**, 1659 (1991).

[55] M. Alcubierre *et al.*, Class. Quant. Grav. **20**, 2883 (2003), gr-qc/0301105.

[56] L. A. Ureña-López, Class. Quant. Grav. **19**, 2617 (2002), gr-qc/0104093.

[57] L. A. Urena-Lopez, S. Valdez-Alvarado, and R. Becerril, Class. Quant. Grav. **29**, 065021 (2012).

[58] F. Muia *et al.*, (2019), 1906.09346.

[59] M. Minamitsuji, Phys. Rev. **D97**, 104023 (2018), 1805.09867.

[60] I. Salazar Landea and F. García, Phys. Rev. **D94**, 104006 (2016), 1608.00011.

[61] R. Brito, V. Cardoso, and H. Okawa, Phys. Rev. Lett. **115**, 111301 (2015), 1508.04773.

[62] M. Alcubierre *et al.*, Class. Quant. Grav. **35**, 19LT01 (2018), 1805.11488.

[63] P. Jetzer, Physics Letters B **231**, 433 (1989).

[64] M. Duarte and R. Brito, Phys. Rev. **D94**, 064055 (2016), 1609.01735.

[65] N. Sanchis-Gual, C. Herdeiro, E. Radu, J. C. Degollado, and J. A. Font, Phys. Rev. **D95**, 104028 (2017), 1702.04532.

[66] F. Di Giovanni, N. Sanchis-Gual, C. A. R. Herdeiro, and J. A. Font, Phys. Rev. **D98**, 064044 (2018), 1803.04802.

[67] L. A. Ureña-López, T. Matos, and R. Becerril, Class. Quant. Grav. **19**, 6259 (2002).

[68] Y.-s. Kobayashi, M. Kasai, and T. Futamase, Phys. Rev. D **50**, 7721 (1994).

[69] F. E. Schunck and E. W. Mielke, Rotating boson stars., in *Relativity and Scientific Computing. Computer Algebra, Numerics, Visualization*, edited by F. W. Hehl, R. A. Puntigam, and H. Ruder, pp. 138–151, 1996.

[70] J. L. Friedman, Communications in Mathematical Physics **63**, 243 (1978).

[71] C.-W. Lai, *A Numerical study of boson stars*, PhD thesis, British Columbia U., 2004, gr-qc/0410040.

[72] V. Silveira and C. M. G. de Sousa, Phys. Rev. D **52**, 5724 (1995).

[73] M. P. Hertzberg and E. D. Schiappacasse, JCAP **1808**, 028 (2018), 1804.07255.

[74] N. Sanchis-Gual *et al.*, (2019), 1907.12565.

[75] C. A. R. Herdeiro and E. Radu, Int. J. Mod. Phys. **D27**, 1843009 (2018), 1803.08149.

[76] L. G. Collodel, B. Kleihaus, and J. Kunz, Phys. Rev. **D99**, 104076 (2019), 1901.11522.

[77] C. Herdeiro, I. Perapechka, E. Radu, and Ya. Shnir, (2019), 1906.05386.

[78] H.-B. Li, S. Sun, T.-T. Hu, Y. Song, and Y.-Q. Wang, (2019), 1906.00420.

[79] R. F. P. Mendes and H. Yang, Class. Quant. Grav. **34**, 185001 (2017), 1606.03035.

[80] V. Cardoso, E. Franzin, A. Maselli, P. Pani, and G. Raposo, Phys. Rev. **D95**, 084014 (2017), 1701.01116, [Addendum: Phys. Rev.D95,no.8,089901(2017)].

[81] H. Witek, L. Gualtieri, P. Pani, and T. P. Sotiriou, Phys. Rev. **D99**, 064035 (2019), 1810.05177.

[82] J. Balakrishna, *A Numerical study of boson stars: Einstein equations with a matter source*, PhD thesis, Washington U., St. Louis, 1999, gr-qc/9906110.

[83] C. Palenzuela, I. Olabarrieta, L. Lehner, and S. L. Liebling, Phys. Rev. **D75**, 064005 (2007), gr-qc/0612067.

[84] M. Bezares, C. Palenzuela, and C. Bona, Phys. Rev. **D95**, 124005 (2017), 1705.01071.

[85] V. Cardoso, S. Hopper, C. F. B. Macedo, C. Palenzuela, and P. Pani, Phys. Rev. **D94**, 084031 (2016), 1608.08637.

[86] R. Brito, V. Cardoso, C. F. B. Macedo, H. Okawa, and C. Palenzuela, Phys. Rev. **D93**, 044045 (2016), 1512.00466.

[87] N. Sanchis-Gual, C. Herdeiro, J. A. Font, E. Radu, and F. Di Giovanni, Phys. Rev. D **99**, 024017 (2019).

[88] M. Bezares and C. Palenzuela, Class. Quant. Grav. **35**, 234002 (2018), 1808.10732.

[89] M. Bezares, D. Vigano, and C. Palenzuela, (2019), 1905.08551.

[90] B. Schwabe, J. C. Niemeyer, and J. F. Engels, ArXiv e-prints (2016), 1606.05151.

[91] T. Dietrich, F. Day, K. Clough, M. Coughlin, and J. Niemeyer, Mon. Not. Roy. Astron. Soc. **483**, 908 (2019), 1808.04746.

[92] K. Clough, T. Dietrich, and J. C. Niemeyer, Phys. Rev. **D98**, 083020 (2018), 1808.04668.

[93] T. Dietrich, S. Ossokine, and K. Clough, Class. Quant. Grav. **36**, 025002 (2019), 1807.06959.

[94] LIGO Scientific, Virgo, B. P. Abbott *et al.*, Phys. Rev. Lett. **119**, 161101 (2017), 1710.05832.

[95] F. H. Vincent, Z. Meliani, P. Grandclement, E. Gourgoulhon, and O. Straub, Class. Quant. Grav. **33**, 105015 (2016), 1510.04170.

[96] P. V. P. Cunha *et al.*, Phys. Rev. **D96**, 104040 (2017), 1709.06118.

[97] R. Hlozek *et al.*, Astrophysical Journal**749**, 90 (2012), 1105.4887.

[98] F. Menanteau *et al.*, Astrophysical Journal**748**, 7 (2012), 1109.0953.

[99] J. Bovy, D. Erkal, and J. L. Sanders, ArXiv e-prints (2016), 1606.03470.

[100] B. Bozek, D. J. E. Marsh, J. Silk, and R. F. G. Wyse, Mon. Not. R. Astron. Soc.**450**, 209 (2015), 1409.3544.

[101] S. Bird *et al.*, ArXiv e-prints (2016), 1603.00464.

[102] D. J. E. Marsh, Physics Reports**643**, 1 (2016), 1510.07633.

[103] J. Preskill, M. B. Wise, and F. Wilczek, Phys. Lett. B **120**, 127 (1983).

[104] L. F. Abbott and P. Sikivie, Phys. Lett. B **120**, 133 (1983).

[105] M. Dine and W. Fischler, Phys. Lett. B **120**, 137 (1983).

[106] M. S. Turner, Physical Review D**28**, 1243 (1983).

[107] M. Khlopov, B. Malomed, and I. Zeldovich, Mon. Not. R. Astron. Soc.**215**, 575 (1985).

[108] R. Ruffini and S. Bonazzola, Physical Review **187**, 1767 (1969).

[109] E. Seidel and W.-M. Suen, Physical Review Letters **72**, 2516 (1994), gr-qc/9309015.

[110] F. S. Guzmán and L. A. Ureña-López, Astrophysical Journal**645**, 814 (2006), astro-ph/0603613.

[111] H.-Y. Schive, T. Chiueh, and T. Broadhurst, Nature Physics **10**, 496 (2014), 1406.6586.

[112] C. J. Hogan and M. J. Rees, Phys. Lett. B **205**, 228 (1988).

[113] E. W. Kolb and I. I. Tkachev, Physical Review D**49**, 5040 (1994), astro-ph/9311037.

[114] K. M. Zurek, C. J. Hogan, and T. R. Quinn, Physical Review D**75**, 043511 (2007), astro-ph/0607341.

[115] S. Davidson and T. Schwetz, Physical Review D**93**, 123509 (2016), 1603.04249.

[116] H.-Y. Schive *et al.*, Physical Review Letters**113**, 261302 (2014), 1407.7762.

[117] D. J. E. Marsh and A.-R. Pop, Mon. Not. R. Astron. Soc.**451**, 2479 (2015), 1502.03456.

[118] W. H. Press, B. S. Ryden, and D. N. Spergel, Physical Review Letters **64**, 1084 (1990).

[119] J. A. Frieman, C. T. Hill, A. Stebbins, and I. Waga, Physical Review Letters **75**, 2077 (1995), astro-ph/9505060.

[120] T. Matos, F. S. Guzman, and L. A. Ureña-López, Class. Quant. Grav. **17**, 1707 (2000), astro-ph/9908152.

[121] V. Sahni and L. Wang, Physical Review D**62**, 103517 (2000), astro-ph/9910097.

[122] W. Hu, R. Barkana, and A. Gruzinov, Physical Review Letters **85**, 1158 (2000), astro-ph/0003365.

[123] T. Matos and L. Arturo Ureña-López, Physical Review D**63**, 063506 (2001), astro-ph/0006024.

[124] A. Arbey, J. Lesgourgues, and P. Salati, Physical Review D**68**, 023511 (2003), astro-ph/0301533.

[125] T. Rindler-Daller and P. R. Shapiro, Mon. Not. R. Astron. Soc.**422**, 135 (2012), 1106.1256.

[126] A. Suárez, V. H. Robles, and T. Matos, A Review on the Scalar Field/Bose-Einstein Condensate Dark Matter Model, in *Accelerated Cosmic Expansion*, edited by C. Moreno González, J. E. Madriz Aguilar, and L. M. Reyes Barrera, , Astrophysics and Space Science Proceedings Vol. 38, p. 107, 2014, 1302.0903.

[127] T. Banks, M. Dine, P. J. Fox, and E. Gorbatov, JCAP.**6**, 1 (2003), hep-th/0303252.

[128] P. Svrcek and E. Witten, Journal of High Energy Physics**6**, 51 (2006), hep-th/0605206.

[129] N. Arkani-Hamed, L. Motl, A. Nicolis, and C. Vafa, Journal of High Energy Physics**6**, 60 (2007), hep-th/0601001.

[130] E. Silverstein and A. Westphal, Physical Review D**78**, 106003 (2008), 0803.3085.

[131] T. C. Bachlechner, M. Dias, J. Frazer, and L. McAllister, Physical Review D**91**, 023520 (2015), 1404.7496.

[132] B. Heidenreich, M. Reece, and T. Rudelius, Journal of High Energy Physics **12**, 108 (2015), 1506.03447.

[133] T. C. Bachlechner, C. Long, and L. McAllister, Journal of High Energy Physics **1**, 91 (2016), 1503.07853.

[134] K. Clough *et al.*, Class. Quant. Grav. **32**, 245011 (2015), 1503.03436, [Class. Quant. Grav.32,24(2015)].

[135] T. W. Baumgarte and S. L. Shapiro, Phys. Rev. **D59**, 024007 (1999), gr-qc/9810065.

[136] M. Shibata and T. Nakamura, Phys.Rev. **D52**, 5428 (1995).

[137] S. Davidson, Astropart. Phys. **65**, 101 (2015), 1405.1139.

[138] J. Barranco and A. Bernal, Physical Review D**83**, 043525 (2011), 1001.1769.

[139] R. Peccei and H. R. Quinn, Physical Review Letters**38**, 1440 (1977).

[140] J. P. Conlon, Journal of High Energy Physics **5**, 078 (2006), hep-th/0602233.

[141] J. E. Kim, H. P. Nilles, and M. Peloso, JCAP.**1**, 5 (2005), hep-ph/0409138.

[142] G. G. Raffelt, Astrophysical Axion Bounds, in *Axions*, edited by M. Kuster, G. Raffelt, and B. Beltrán, , Lecture Notes in Physics, Berlin Springer Verlag Vol. 741, p. 51, 2008, hep-ph/0611350.

[143] C. W. Misner, K. S. Thorne, and J. A. Wheeler, *Gravitation* (San Francisco: W.H. Freeman and Co., 1973, 1973).

[144] S. B. Giddings and A. Strominger, Nuclear Physics B **307**, 854 (1988).

[145] S. Coleman, Nuclear Physics B **310**, 643 (1988).

[146] G. Gilbert, Nuclear Physics B **328**, 159 (1989).

[147] M. Kamionkowski and J. March-Russell, Physics Letters B **282**, 137 (1992), hep-th/9202003.

[148] G. Grilli di Cortona, E. Hardy, J. Pardo Vega, and G. Villadoro, ArXiv e-prints (2015), 1511.02867.

[149] S. H. Hawley and M. W. Choptuik, Phys. Rev. **D62**, 104024 (2000), gr-qc/0007039.

[150] S. Kichenassamy, Communications on Pure and Applied Mathematics **44**, 789 (1991).

[151] M. P. Hertzberg, Phys. Rev. **D82**, 045022 (2010), 1003.3459.

[152] M. A. Amin, R. Easther, and H. Finkel, JCAP **1012**, 001 (2010), 1009.2505.

[153] M. A. Amin and D. Shirokoff, Phys. Rev. **D81**, 085045 (2010), 1002.3380.

[154] M. A. Amin, R. Easther, H. Finkel, R. Flauger, and M. P. Hertzberg, Phys. Rev. Lett. **108**, 241302 (2012), 1106.3335.

[155] T. W. Baumgarte and S. L. Shapiro, *Numerial Relativity : Solving Einstein's Equations on the Computer* (CUP, 2010).

[156] J. Barranco *et al.*, Phys. Rev. **D84**, 083008 (2011), 1108.0931.

[157] J. Barranco *et al.*, Phys. Rev. Lett. **109**, 081102 (2012), 1207.2153.

[158] H. Okawa, H. Witek, and V. Cardoso, Phys. Rev. **D89**, 104032 (2014), 1401.1548.

[159] F. S. Guzman and F. D. Lora-Clavijo, Phys. Rev. **D85**, 024036 (2012), 1201.3598.

[160] S. Weinberg, Physical Review Letters**40**, 223 (1978).

[161] F. Wilczek, Physical Review Letters**40**, 279 (1978).

[162] A. Arvanitaki and S. Dubovsky, Physical Review D**83**, 044026 (2011), 1004.3558.

[163] A. Arvanitaki, M. Baryakhtar, and X. Huang, Physical Review D**91**, 084011 (2015), 1411.2263.

[164] M. Volonteri, The Astronomy and Astrophysics Review**18**, 279 (2010), 1003.4404.

[165] M. Shibata and S. L. Shapiro, Astrophys. J. Lett.**572**, L39 (2002), astro-ph/0205091.

[166] D. Spolyar, K. Freese, and P. Gondolo, Physical Review Letters **100**, 051101 (2008), 0705.0521.

[167] K. Freese, P. Bodenheimer, D. Spolyar, and P. Gondolo, Astrophys. J. Lett.**685**, L101 (2008), 0806.0617.

[168] Rowan J. Smith and Fabio Iocco and Simon C. O. Glover and Dominik R. G. Schleicher and Ralf S. Klessen and Shingo Hirano and Naoki Yoshida, The Astrophysical Journal **761**, 154 (2012).

[169] E. Ripamonti *et al.*, Mon. Not. Roy. Astron. Soc. **406**, 2605 (2010), 1003.0676.

[170] E. Ripamonti *et al.*, PoS **IDM2008**, 075 (2009), 0903.0346.

[171] F. Iocco *et al.*, Mon. Not. Roy. Astron. Soc. **390**, 1655 (2008), 0805.4016.

[172] BICEP2/Keck and Planck Collaborations *et al.*, Physical Review Letters**114**, 101301 (2015), 1502.00612.

[173] M. P. Hertzberg, (2016), 1609.01342.

[174] P. Sikivie and E. M. Todarello, (2016), 1607.00949.

[175] S. Davidson and T. Schwetz, Phys. Rev. **D93**, 123509 (2016), 1603.04249.

[176] J. Eby, P. Suranyi, and L. C. R. Wijewardhana, Modern Physics Letters A **31**, 1650090 (2016), 1512.01709.

[177] J. Eby, M. Leembruggen, P. Suranyi, and L. C. R. Wijewardhana, ArXiv e-prints (2016), 1608.06911.

[178] E. Braaten, A. Mohapatra, and H. Zhang, ArXiv e-prints (2016), 1609.05182.

[179] A. Riotto and I. Tkachev, Phys. Lett. **B484**, 177 (2000), astro-ph/0003388.

[180] S. Weinberg, *Gravitation and Cosmology: Principles and Applications of the General Theory of Relativity* (Wiley-VCH, 1972).

[181] I. I. Tkachev, Soviet Journal of Experimental and Theoretical Physics Letters **101**, 1 (2015), 1411.3900.

[182] M. W. Choptuik, Phys.Rev.Lett. **70**, 9 (1993).

[183] C. Gundlach, Living Rev. Rel. **2**, 4 (1999), gr-qc/0001046.

[184] P. R. Brady, C. M. Chambers, and S. M. C. V. Goncalves, Phys. Rev. **D56**, 6057 (1997), gr-qc/9709014.

[185] J. A. Gonzalez and F. S. Guzman, Phys. Rev. **D83**, 103513 (2011), 1105.2066.

[186] A. Bernal and F. S. Guzmán, Phys. Rev. D **74**, 103002 (2006).

[187] A. Paredes and H. Michinel, Physics of the Dark Universe **12**, 50 (2016), 1512.05121.

[188] B. Schwabe, J. C. Niemeyer, and J. F. Engels, Phys. Rev. D **94**, 043513 (2016).

[189] A. Arvanitaki, M. Baryakhtar, S. Dimopoulos, S. Dubovsky, and R. Lasenby, ArXiv e-prints (2016), 1604.03958.

[190] J. Y. Widdicombe, T. Helfer, D. J. E. Marsh, and E. A. Lim, JCAP **1810**, 005 (2018), 1806.09367.

[191] B. P. Abbott *et al.*, Physical Review Letters **119**, 161101 (2017), 1710.05832.

[192] L. Hui, J. P. Ostriker, S. Tremaine, and E. Witten, Phys. Rev. **D95**, 043541 (2017), 1610.08297.

[193] C. Hanna, M. C. Johnson, and L. Lehner, Phys. Rev. **D95**, 124042 (2017), 1611.03506.

[194] Z. G. Berezhiani, M. Yu. Khlopov, and R. R. Khomeriki, Sov. J. Nucl. Phys. **52**, 65 (1990), [Yad. Fiz.52,104(1990)].

[195] Z. G. Berezhiani and M. Yu. Khlopov, Z. Phys. **C49**, 73 (1991).

[196] A. S. Sakharov and M. Yu. Khlopov, Phys. Atom. Nucl. **57**, 485 (1994), [Yad. Fiz.57,514(1994)].

[197] Z. G. Berezhiani, A. S. Sakharov, and M. Yu. Khlopov, Sov. J. Nucl. Phys. **55**, 1063 (1992), [Yad. Fiz.55,1918(1992)].

[198] A. G. Dias, A. C. B. Machado, C. C. Nishi, A. Ringwald, and P. Vaudrevange, Journal of High Energy Physics **6**, 37 (2014), 1403.5760.

[199] J. Jaeckel and A. Ringwald, Annual Review of Nuclear and Particle Science **60**, 405 (2010), 1002.0329.

[200] A. Arvanitaki, S. Dimopoulos, S. Dubovsky, N. Kaloper, and J. March-Russell, Phys. Rev. **D81**, 123530 (2010), 0905.4720.

[201] D. J. E. Marsh, Phys. Rept. **643**, 1 (2016), 1510.07633.

[202] M. Cicoli, M. Goodsell, and A. Ringwald, JHEP **10**, 146 (2012), 1206.0819.

[203] E. Seidel and W.-M. Suen, Physical Review Letters **66**, 1659 (1991).

[204] X. Du, B. Schwabe, J. C. Niemeyer, and D. Bürger, Phys. Rev. **D97**, 063507 (2018), 1801.04864.

[205] J. Veltmaat, J. C. Niemeyer, and B. Schwabe, Phys. Rev. **D98**, 043509 (2018), 1804.09647.

[206] H.-Y. Schive, T. Chiueh, and T. Broadhurst, Nature Phys. **10**, 496 (2014), 1406.6586.

[207] B. Schwabe, J. C. Niemeyer, and J. F. Engels, Physical Review D**94**, 043513 (2016), 1606.05151.

[208] D. G. Levkov, A. G. Panin, and I. I. Tkachev, (2018), 1804.05857.

[209] K. Clough *et al.*, Classical and Quantum Gravity **32**, 245011 (2015), 1503.03436.

[210] A. S. Josan, A. M. Green, and K. A. Malik, Phys. Rev. **D79**, 103520 (2009), 0903.3184.

[211] B. Carr, F. Kuhnel, and M. Sandstad, Phys. Rev. **D94**, 083504 (2016), 1607.06077.

[212] H. Niikura *et al.*, ArXiv e-prints (2017), 1701.02151.

[213] P. Ajith *et al.*, Phys. Rev. Lett. **106**, 241101 (2011), 0909.2867.

[214] D. G. Levkov, A. G. Panin, and I. I. Tkachev, Physical Review Letters **118**, 011301 (2017), 1609.03611.

[215] P.-H. Chavanis, (2017), 1710.06268.

[216] L. Visinelli, S. Baum, J. Redondo, K. Freese, and F. Wilczek, Phys. Lett. **B777**, 64 (2018), 1710.08910.

[217] H.-Y. Schive *et al.*, Physical Review Letters**113**, 261302 (2014), 1407.7762.

[218] X. Du, C. Behrens, J. C. Niemeyer, and B. Schwabe, Phys. Rev. **D95**, 043519 (2017), 1609.09414.

[219] A. S. Sakharov, D. D. Sokoloff, and M. Yu. Khlopov, Phys. Atom. Nucl. **59**, 1005 (1996), [Yad. Fiz.59N6,1050(1996)].

[220] E. W. Kolb and I. I. Tkachev, Phys. Rev. **D49**, 5040 (1994), astro-ph/9311037.

[221] M. Khlopov, A. Sakharov, and D. Sokoloff, Nuclear Physics B - Proceedings Supplements **72**, 105 (1999), Proceedings of the 5th IFT Workshop on Axions.

[222] D. Croon, M. Gleiser, S. Mohapatra, and C. Sun, (2018), 1802.08259.

[223] R. Brito *et al.*, Phys. Rev. **D96**, 064050 (2017), 1706.06311.

[224] M. W. Choptuik and F. Pretorius, Phys. Rev. Lett. **104**, 111101 (2010), 0908.1780.

[225] C. Palenzuela *et al.*, Phys. Rev. **D96**, 104058 (2017), 1710.09432.

[226] B. J. Carr, eConf **C041213**, 0204 (2004), astro-ph/0504034.

[227] S. Kasuya and M. Kawasaki, Phys. Rev. **D80**, 023516 (2009), 0904.3800.

[228] D. J. Chung and A. Upadhye, Phys. Rev. **D95**, 023503 (2017), 1610.04284.

[229] G. Efstathiou and J. R. Bond, Mon. Not. R. Astron. Soc.**218**, 103 (1986).

[230] M. Yu. Khlopov and A. G. Polnarev, Phys. Lett. **97B**, 383 (1980).

[231] T. Harada, C.-m. Yoo, K. Kohri, K.-i. Nakao, and S. Jhingan, Astrophysical Journal**833**, 61 (2016), 1609.01588.

[232] G. D. Coughlan, W. Fischler, E. W. Kolb, S. Raby, and G. G. Ross, Phys. Lett. B **131**, 59 (1983).

[233] L. Iliesiu, D. J. E. Marsh, K. Moodley, and S. Watson, Physical Review D**89**, 103513 (2014), 1312.3636.

[234] Y. Kahn, B. R. Safdi, and J. Thaler, Phys. Rev. Lett. **117**, 141801 (2016), 1602.01086.

[235] D. Budker, P. W. Graham, M. Ledbetter, S. Rajendran, and A. O. Sushkov, Phys. Rev. X **4**, 021030 (2014), 1306.6089.

[236] L. Di Luzio, F. Mescia, and E. Nardi, Phys. Rev. Lett. **118**, 031801 (2017), 1610.07593.

[237] Virgo, LIGO Scientific, B. P. Abbott *et al.*, Phys. Rev. Lett. **116**, 241103 (2016), 1606.04855.

[238] VIRGO, LIGO Scientific, B. P. Abbott *et al.*, Phys. Rev. Lett. **118**, 221101 (2017), 1706.01812.

[239] R. Friedberg, T. D. Lee, and Y. Pang, Phys. Rev. **D35**, 3640 (1987), [,55(1986)].

[240] D. N. Page, Phys. Rev. **D70**, 023002 (2004), gr-qc/0310006.

[241] T. Helfer, J. C. Aurrekoetxea, and E. A. Lim, Phys. Rev. **D99**, 104028 (2019), 1808.06678.

[242] T. W. B. Kibble, J. Phys. **A9**, 1387 (1976).

[243] E. J. Copeland and T. W. B. Kibble, Proc. Roy. Soc. Lond. **A466**, 623 (2010), 0911.1345.

[244] L. Pogosian, S. H. H. Tye, I. Wasserman, and M. Wyman, Phys. Rev. **D68**, 023506 (2003), hep-th/0304188, [Erratum: Phys. Rev.D73,089904(2006)].

[245] N. T. Jones, H. Stoica, and S. H. H. Tye, Phys. Lett. **B563**, 6 (2003), hep-th/0303269.

[246] Planck, P. A. R. Ade *et al.*, Astron. Astrophys. **571**, A25 (2014), 1303.5085.

[247] A. Vilenkin and E. P. S. Shellard, *Cosmic Strings and Other Topological Defects* (Cambridge University Press, 2000).

[248] A. Vilenkin, Phys. Lett. **107B**, 47 (1981).

[249] T. Damour and A. Vilenkin, Phys. Rev. **D71**, 063510 (2005), hep-th/0410222.

[250] M. Hindmarsh, J. Lizarraga, J. Urrestilla, D. Daverio, and M. Kunz, Phys. Rev. **D96**, 023525 (2017), 1703.06696.

[251] G. Vincent, N. D. Antunes, and M. Hindmarsh, Phys. Rev. Lett. **80**, 2277 (1998), hep-ph/9708427.

[252] J. N. Moore and E. P. S. Shellard, (1998), hep-ph/9808336.

[253] K. D. Olum and J. J. Blanco-Pillado, Phys. Rev. **D60**, 023503 (1999), gr-qc/9812040.

[254] J. N. Moore, E. P. S. Shellard, and C. J. A. P. Martins, Phys. Rev. **D65**, 023503 (2002), hep-ph/0107171.

[255] J. J. Blanco-Pillado, K. D. Olum, and B. Shlaer, Phys. Rev. **D83**, 083514 (2011), 1101.5173.

[256] S. Hawking, Physics Letters B **246**, 36 (1990).

[257] U. Sperhake, V. Cardoso, F. Pretorius, E. Berti, and J. A. Gonzalez, Phys. Rev. Lett. **101**, 161101 (2008), 0806.1738.

[258] W. E. East and F. Pretorius, Phys. Rev. Lett. **110**, 101101 (2013), 1210.0443.

[259] J. J. Blanco-Pillado and K. D. Olum, Phys. Rev. **D96**, 104046 (2017), 1709.02693.

[260] C. Ringeval and T. Suyama, JCAP **1712**, 027 (2017), 1709.03845.

[261] S. W. Hawking, Physics Letters B **231**, 237 (1989).

[262] A. Polnarev and R. Zembowicz, Phys. Rev. D **43**, 1106 (1991).

[263] R. R. Caldwell and P. Casper, Phys. Rev. D **53**, 3002 (1996).

[264] LIGO Scientific, Virgo, B. P. Abbott *et al.*, (2018), 1811.12907.

[265] D. Garfinkle and T. Vachaspati, Phys. Rev. D **42**, 1960 (1990).

[266] I. M. Moroz, R. Penrose, and P. Tod, Classical and Quantum Gravity **15**, 2733 (1998).

[267] A. H. Guth, M. P. Hertzberg, and C. Prescod-Weinstein, Physical Review D**92**, 103513 (2015), 1412.5930.

[268] P.-H. Chavanis, Physical Review D**84**, 043531 (2011), 1103.2050.

[269] A. H. Guth, Physical Review D**23**, 347 (1981).

[270] A. D. Linde, Phys. Lett. B **108**, 389 (1982).

[271] A. Albrecht and P. J. Steinhardt, Physical Review Letters**48**, 1220 (1982).

[272] G. W. Gibbons and S. W. Hawking, Physical Review D**15**, 2738 (1977).

[273] T. Hiramatsu, M. Kawasaki, K. Saikawa, and T. Sekiguchi, Physical Review D**85**, 105020 (2012), 1202.5851.

[274] H.-Y. Schive, T. Chiueh, T. Broadhurst, and K.-W. Huang, Astrophysical Journal**818**, 89 (2016), 1508.04621.

[275] M. Adams *et al.*

[276] M. Berger and J. Oliger, J. Comput. Phys. , 484 (1984).

[277] M. J. Berger and P. Colella, Journal of Computational Physics **82**, 64 (1989).

[278] M. J. Berger and I. Rigoutsos, IEEE Trans. Sys. Man & Cyber. **21**, 1278 (1991).

[279] M. Alcubierre *et al.*, Phys. Rev. **D67**, 084023 (2003), gr-qc/0206072.

[280] M. Shibata and T. Nakamura, Phys. Rev. D **52**, 5428 (1995).

[281] R. Arnowitt, S. Deser, and C. W. Misner, Phys. Rev. **116**, 1322 (1959).

[282] M. Hannam, S. Husa, F. Ohme, B. Bruegmann, and N. O'Murchadha, Phys.Rev. **D78**, 064020 (2008), 0804.0628.

[283] U. H. Hernandez-Belmonte, V. Ayala-Ramirez, and R. E. Sanchez-Yanez, A comparative review of two-pass connected component labeling algorithms, in *Advances in Soft Computing*, edited by I. Batyrshin and G. Sidorov, pp. 452–462, Berlin, Heidelberg, 2011, Springer Berlin Heidelberg.

[284] A. Rosenfeld and J. L. Pfaltz, J. ACM **13**, 471 (1966).

[285] L. D. Stefano and A. Bulgarelli, A simple and efficient connected components labeling algorithm, in *Proceedings 10th International Conference on Image Analysis and Processing*, pp. 322–327, 1999.

[286] L. He, Y. Chao, K. Suzuki, and K. Wu, Pattern Recognition **42**, 1977 (2009).

[287] K. Suzuki, I. Horiba, and N. Sugie, Comput. Vis. Image Underst. **89**, 1 (2003).

[288] K. Clough *et al.*, JCAP **1709**, 025 (2017), 1608.04408.

[289] I. Suh, G. J. Mathews, J. R. Haywood, and N. Q. Lan, Adv. Astron. **2017**, 6127031 (2017), 1601.01460.

[290] GRChombo, Stiffness test of oscillatons, 2018, https://youtu.be/LCpTmEuZm-I.

[291] J. E. Kim, H. P. Nilles, and M. Peloso, JCAP **0501**, 005 (2005), hep-ph/0409138.

[292] R. Kappl, S. Krippendorf, and H. P. Nilles, Phys. Lett. **B737**, 124 (2014), 1404.7127.

[293] M. Zilhão, H. Witek, and V. Cardoso, Class. Quant. Grav. **32**, 234003 (2015), 1505.00797.

[294] D. Hilditch, Int. J. Mod. Phys. **A28**, 1340015 (2013), 1309.2012.

[295] C. Palenzuela, L. Lehner, and S. Yoshida, Phys. Rev. **D81**, 084007 (2010), 0911.3889.

[296] J. G. Baker, M. Campanelli, and C. O. Lousto, Phys. Rev. **D65**, 044001 (2002), gr-qc/0104063.

[297] K. D. Kokkotas and B. G. Schmidt, Living Reviews in Relativity **2**, 2 (1999).

[298] M. Nagasawa and J. Yokoyama, Phys. Lett. **B345**, 416 (1995), astro-ph/9404041.

Appendix A

Black hole formation from Axion stars

A.1 Notes on Axions

A.1.1 Non-relativistic Axion stars and oscillotons

Here we give a brief and hopefully pedagogical introduction to Axion stars in the non-relativistic limit of weak gravity, rapid field oscillations, and small angle field excursions. This introduction should be familiar from studies of Axion and scalar field DM halos. We aim to provide intuition for the existence of Axion stars in this limit, without requiring numerical simulation.

The wave equation for the axion field after spontaneous symmetry breaking (SSB) is:

$$\Box\phi - \frac{\Lambda_a^4}{f_a}\sin(\phi/f_a) = 0\,. \tag{A.1}$$

In the regime of small ($\phi \ll f_a$) field fluctuations, consider the ansatz solution:

$$\phi = \psi e^{-im_a t} + \psi^\star e^{im_a t}\,. \tag{A.2}$$

Consider for simplicity the non-relativistic limit. The energy density of the axion field is

$$\rho_a = \frac{1}{2}m_a^2|\psi|^2\,, \tag{A.3}$$

and the “wavefunction” ψ obeys the Schrödinger-like Gross-Pitaevski equation (ignoring self interactions):[1]

$$i\dot{\psi} = -\frac{1}{2m_a}\nabla^2\psi + m_a\Psi\psi, \tag{A.4}$$

$$\nabla^2\Psi = \frac{m_a^2}{4M_{pl}^2}|\psi|^2, \tag{A.5}$$

where Ψ is the Newtonian potential.

Assuming spherical symmetry, stable solutions with constant (in time) ρ_a take the form $\psi(r,t) = e^{i\gamma t}g(r)$, leading to an eigenvalue problem for the radial function $g(r)$ (after specifying the boundary conditions). The ground state solution (found numerically) has $\gamma = -0.692 m_a$. The solutions possess a scaling symmetry, and are specified as a one parameter family, defined by the central field value, $\phi(r=0)$. This family of solutions to $m^2\phi^2$ theory are known as *oscillotons*. Here we have worked in the non-relativistic limit, but oscilloton solutions to the full Einstein-Klein-Gordon equations also exist, although they must be found numerically, as is described in the following section.

A.1.2 Relativistic Axion stars and oscillotons

The full spherically symmetric oscilloton solutions for the $m^2\phi^2$ theory in GR must be constructed for use in our initial conditions in Section 3.3.

To obtain the radial oscilloton profiles we use the ansatz for the spherically symmetric line element:

$$ds^2 = -\alpha^2 dt^2 + a^2 dr^2 + r^2(d\theta^2 + \sin^2(\theta)d\phi^2), \tag{A.6}$$

We define the quantities $A = a^2$, $C = \frac{a^2}{\alpha^2}$. Solutions are then obtained by expanding the metric functions and the scalar field in their Fourier components, assuming they have profiles that oscillate coherently with base frequency ω:

---

[1] For various useful discussions, derivations, solutions, and properties of this system of equations, relating both to axions and other scalar/condensate DM, see e.g. Refs. [266, 125, 267, 115]. A very thorough history can be found in Ref. [268].

$$\begin{aligned}\phi_m(t,r) &= \sum_{j\in 2\mathbb{N}_{\geq 0}+1}^{j_{\max}} \phi_{m,j}(r)\cos(j\omega t),\\ A(t,r) &= \sum_{j\in 2\mathbb{N}_{\geq 0}}^{j_{\max}} A_j(r)\cos(j\omega t),\\ C(t,r) &= \sum_{j\in 2\mathbb{N}_{\geq 0}}^{j_{\max}} C_j(r)\cos(j\omega t),\end{aligned} \tag{A.7}$$

where $j_{\max}$ is the maximum order in the Fourier expansion to which the solution is obtained. The value of $j_{\max}$ sets the amount by which the Hamiltonian and momentum constraints are violated by the approximate initial conditions, with higher values resulting in smaller constraint violation. We found that sufficient accuracy of $\mathcal{O}(1\%)$ in the relative Hamiltonian constraint violation (see Equation A.30) could be obtained with $j_{\max} = 12$. In similar numerical studies ([67]), values of $j_{\max}$ of 10 have been used. To generate these solutions efficiently for large $j_{\max}$ we used the code of Ref. [55].

One now substitutes the Fourier expansion into the Einstein-Klein-Gordon system of equations with $V(\phi) = m^2\phi^2/2$, which are

$$\partial_r A = \frac{8\pi A r}{2}\left(C(\partial_t\phi_m)^2 + (\partial_r\phi_m)^2 + Am^2\phi_m^2\right) + \frac{A}{r}(1-A), \tag{A.8}$$

$$\partial_r C = \frac{2C}{r}\left(1 + A\left(\frac{1}{2}8\pi r^2 m^2\phi_m^2 - 1\right)\right), \tag{A.9}$$

$$C\partial_t^2\phi_m = -\frac{1}{2}\partial_t C\partial_t\phi_m + \partial_r^2\phi_m + \partial_r\phi_m\left(\frac{2}{r} - \frac{\partial_r C}{2C}\right) - Am^2\phi_m, \tag{A.10}$$

$$\partial_t A = 8\pi r A\partial_t\phi_m\partial_r\phi_m, \tag{A.11}$$

These are effectively the Hamiltonian and Momentum constraints of GR with a scalar field as the energy-momentum source. The solutions thus found have $\phi_m(0,0) \neq 0$, and the subscript "m" reminds us that this particular solution for ϕ applies to the $m^2\phi^2$ theory. These profiles for ϕ in $m^2\phi^2$ theory are known as oscillotons and are described in e.g. Refs. [55, 67, 56]. They are a one parameter family, for which a larger ADM mass leads to a smaller radius and a higher central field value.

Assuming flat space at infinity and imposing regularity, one obtains boundary conditions both at the centre and at spatial infinity. The Fourier coefficients, and the frequency, $\omega = \Omega m$ with $\Omega \approx 1$, can be found numerically, using a shooting technique, in which the boundary conditions at infinity are sought by tuning those at the centre and integrating outwards until they coincide. To compensate for the small domain of the shooting technique, we truncate the field, setting ϕ to zero at a certain radius and extending the solution by matching it to a Schwarzschild solution.

As described in the main text, we use these oscilloton solutions to construct Axion star solutions valid for $V(\phi) = m_a^2 f_a^2 [1 - \cos(\phi/f_a)]$ in the following manner. The solutions for A, C, ϕ are taken on a hyperslice at $t_i = \frac{1}{\omega}\pi/2$, where $\phi = 0$ everywhere, but $\Pi(t_i) \neq 0$. The value of Π is obtained from the time derivative of the solution for ϕ at this point. Crucially, because on this initial hyperslice $\phi = 0$ everywhere, this implies $V(\phi = 0) = 0$, and therefore for each solution for Π the Hamiltonian constraint is satisfied and valid in the full cosine potential.

Although $\phi = 0$ everywhere on the initial hypersurface for our solutions, we refer to them as “Axion stars” because of their formal construction from the compact quasi-stable solutions in the $m^2\phi^2$ theory.

In Fig. A.1 we plot the ADM mass for the relativistic oscilloton solutions as a function of the first component of the Fourier expansion, $\phi_{1,m}$, which gives the approximate central field value of the oscilloton. As is well known [108], increasing $\phi_{1,m}$ results in a mass curve with a maximum value of $\phi_{1,m} \approx 0.48$, above which oscillotons are unstable [55].

Oscillotons are clearly a solution to the small-field axion equations of motion, where $\phi/f_a \ll 1$ and self-interactions can be neglected. When the axion is treated as having only a mass term, oscillotons form in simulations of the QCD phase transition [113], and in the centres of axion DM halos in cosmological simulations [111]. As these astrophysical Axion stars grow, either through accretion or mergers, the central axion field value will grow, and the Newtonian potential will increase. Thus, they will eventually leave the validity of the $m^2\phi^2$ approximation, i.e. they will no longer be oscillotons, and strong gravity effects will become important. Non-perturbative interactions (in the form of the cosine potential) and strong gravity effects are therefore both expected to play a role in the life, and death, of Axion stars. It is these effects which we seek to understand in this work.

A.1.3 Cosmological initial conditions and symmetry breaking

Consider the cosmological evolution of the PQ field. SSB occurs at the temperature $T_{\rm PQ} = f_a$ and non-perturbative effects switch on at $T_{\rm NP} \approx \Lambda_a$ (such that, to zeroth order, $\varepsilon(T > T_{\rm NP}) = 0$). We consider the order of events SSB followed by non-perturbative effects, i.e. $T_{\rm PQ} > T_{\rm NP}$. As the Universe cools, we first have PQ symmetry breaking, then shift symmetry breaking.

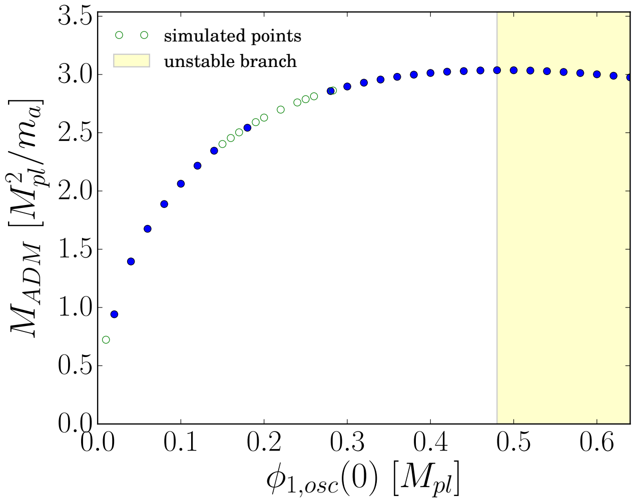

Fig. A.1 **Criticality of oscillotons.** We show the oscilloton ADM mass, M_{ADM}, versus $\phi_{1,m}(0)$, the value of the first component in the Fourier expansion of the field profile at the centre. There is a critical value $\phi_{1,m} = 0.48M_{pl}$ where the mass relation turns over, and oscillotons become unstable. This defines $M_{\text{crit.,osc.}}$, the oscilloton critical mass. Blue points show the oscilloton initial conditions used to map the $M_{\text{ADM}}(\phi_1)$ relationship. Green points show those values of M_{ADM} for which we actually simulate dynamical Axion stars. As we show above, Axion stars show non-trivial behaviour and collapse for $M_{\text{ADM}} < M_{\text{crit.,osc.}}$.

For simplicity, we describe axion cosmology in the context of the standard inflationary paradigm [269–271], but the picture is easy to generalize. The temperature during inflation is given by the Gibbons-Hawking temperature [272], $T_{\text{GH}} = H_I/2\pi$, where H_I is the Hubble scale. The maximum thermalization temperature after inflation (related to the reheating temperature) is $T_{\text{max.}}$. The values of T_{GH} and $T_{\text{max.}}$ compared to T_{PQ} serve to set the initial conditions on the axion field and determines how the axion DM relic abundance is determined, and how Axion stars are formed.[2]

If $T_{\text{PQ}} > \max\{T_{\text{GH}}, T_{\text{max.}}\}$ (case I), then the PQ symmetry is broken during inflation, and is not restored by thermal fluctuations in the post inflation Universe. In this case the axion field is initially approximately homogeneous across our entire causal volume. There are small, almost scale-invariant isocurvature perturbations in the axion field, as well as the dominant adiabatic curvature perturbation.

If $T_{\text{PQ}} < \max\{T_{\text{GH}}, T_{\text{max.}}\}$ (case II), then the PQ symmetry is broken sometime after inflation. The dominant adiabatic curvature perturbation is still present, but now there are also $\mathcal{O}(1)$ isocurvatrue perturbations in the axion field, coherent over scales of order the horizon size at symmetry breaking.

---

[2] The values of T_{GH} and $T_{\text{max.}}$ compared to T_{NP} also have an affect on the details of the relic abundance calculation, but the qualitative picture is unchanged.

When $T < T_{\rm NP}$ and $H \lesssim m_a$, the axion field begins to oscillate about its potential minimum. The coherent classical field then begins to behave like dark matter [106], and any topological defects decay into a cold population of axions (e.g. Ref. [273] and references therein). The axion DM fluctuations then begin to cluster and form structure in the Universe. On large scales, axions form DM haloes indistinguishable from those of standard cold DM as long as $m_a \gtrsim 10^{-22}$ eV (e.g. Refs. [100, 274]), while on small scales, pressure support leads to the formation of Axion stars (e.g. Refs. [113, 111]). The mass function (number density) of structures formed, and thus the characteristic mass of Axion stars in the Universe, depends on whether we are in case I or case II. We discuss the importance of this in Section 2.3.

A.2 GRChombo

This appendix summarises the key features of the numerical relativity code GRCHOMBO. For a more full discussion see [134].

A.2.1 Numerical implementation

GRCHOMBO is a multi-purpose numerical relativity code, which is built on top of the open source `Chombo` framework. `Chombo` is a set of tools developed by Lawrence Berkeley National Laboratory for implementing block-structured AMR in order to solve partial differential equations [275].

The key features of `Chombo` are:

- *C++ class structure*: `Chombo` is primarily written in the C++ language, using the class structure inherent in that language to separate the various evolution and update processes.

- *Adaptive Mesh Refinement*: `Chombo` provides Berger-Oliger style [276, 277] AMR with Berger-Rigoutsos [278] block-structured grid generation. Chombo supports full non-trivial mesh topology – i.e. many-boxes-in-many-boxes. The user is required to specify regridding criteria, which is usually based on setting a maximum threshold for the change in a variable across a gridpoint.

- *MPI scalability*: `Chombo` contains parallel infrastructure which gives it the ability to scale efficiently to several thousand CPU-cores per run. It uses an inbuilt load balancing algorithm, with Morton ordering to map grid responsibility to neighbouring processors in order to optimize processor number scaling.

- *Standardized Output and Visualization*: `Chombo` uses the `HDF5` output format, which is supported by many popular visualization tools such as `VisIt`. In addition, the output files can be used as input files if one chooses to continue a previously stopped run – i.e. the output files are also checkpoint files.

The key features of GRCHOMBO are:

- *BSSN formalism with moving puncture*: GRCHOMBO evolves the Einstein equation in the BSSN formalism with scalar matter. Singularities of Black holes are managed using the moving puncture gauge conditions [8, 6]. These evolution equations and gauge conditions are detailed further below.

- *4th order discretisation in space and time*: We use the method of lines with 4th order spatial stencils and a 4th order Runge-Kutta time update. We use symmetric stencils for spatial derivatives, except for the advection derivatives (of the form $\beta^i \partial_i F$) for which we use one-sided/upwinded stencils. In [134] it was shown that the convergence is approximately 4th order without regridding, but reduces to 3rd order convergence with regridding effects.

- *Kreiss-Oliger dissipation*: Kreiss-Oliger dissipation is used to control errors, from both truncation and the interpolation associated with regridding.

- *Boundary conditions*: We use either periodic boundaries or Sommerfeld boundary conditions [279], which allow outgoing waves to exit the grid with minimal reflections. For many simulations, the AMR ability allows us to set the boundaries far enough away so that reflections do not affect the results during simulation time.

- *Initial Conditions*: In principle any initial conditions can be used, for example, where solutions to the constraints have been found numerically, these can be read into the grid using a simple first order interpolation. Note that GRCHOMBO itself does not currently solve the constraints for the initial conditions.

- *Diagnostics*: GRCHOMBO permits the user to monitor the Hamiltonian and momentum constraint violation, find spherically symmetric apparent horizons, and calculate ADM mass and momenta values.

A.2.2 Gauge choice

GRCHOMBO uses the BSSN formalism [135, 280, 136] of the Einstein equation in 3+1 dimensions. This is similar to the more well known ADM decomposition [281], but is more stable numerically. The 4 dimensional spacetime metric is decomposed into a spatial metric on a 3 dimensional spatial hypersurface, γ_{ij}, and an extrinsic curvature K_{ij}, which are both evolved along a chosen local time coordinate t. Since one is free to choose what is space and what is time, the gauge choice must also be specified. The line element of the decomposition is

$$ds^2 = -\alpha^2 dt^2 + \gamma_{ij}(dx^i + \beta^i dt)(dx^j + \beta^j dt)\,, \tag{A.12}$$

where α and β^i are the lapse and shift, the gauge parameters. These parameters are specified on the initial hypersurface and then allowed to evolve using gauge-driver equations, in accordance with the puncture gauge [8][6], for which the evolution equations are

$$\partial_t \alpha = -\mu\alpha K + \beta^i \partial_i \alpha \,, \tag{A.13}$$

$$\partial_t \beta^i = B^i \,, \tag{A.14}$$

$$\partial_t B^i = \frac{3}{4}\partial_t \Gamma^i - \eta B^i \,, \tag{A.15}$$

where the constants η, of order $1/M_{ADM}$, and μ, of order 1, may be varied by the user to improve stability. The effect of the moving puncture gauge is to avoid resolving the central singularity of the Black hole. It was shown that in this gauge the central gridpoints asymptote to a fixed radius within the event horizon, the so-called “trumpet” solution described in [282]. Thus numerical excision of the central singularity is not required. Whilst constraint violation occurs at the central point due to taking gradients across the puncture, these remain within the horizon and do not propagate into the outside spacetime.

A.2.3 Evolution equations

In GRCHOMBO the induced metric is decomposed as

$$\gamma_{ij} = \frac{1}{\chi^2}\tilde{\gamma}_{ij} \quad \det\tilde{\gamma}_{ij} = 1 \quad \chi = \left(\det\gamma_{ij}\right)^{-\frac{1}{6}} \,. \tag{A.16}$$

Thus for weak gravity cases the conformal factor χ is approximately related to the Newtonian gravitational potential V_{Newton} by

$$\chi = \sqrt{\frac{1}{1-2V_{Newton}}} \, , \tag{A.17}$$

and a value of χ less than 1 can be loosely thought of as corresponding to a gravitational “well". The extrinsic curvature is decomposed into its trace, $K = \gamma^{ij}K_{ij}$, and its traceless part $\tilde{\gamma}^{ij}\tilde{A}_{ij} = 0$ as

$$K_{ij} = \frac{1}{\chi^2}\left(\tilde{A}_{ij} + \frac{1}{3}K\tilde{\gamma}_{ij}\right) \, . \tag{A.18}$$

The conformal connections $\tilde{\Gamma}^i = \tilde{\gamma}^{jk}\tilde{\Gamma}^i{}_{jk}$ where $\tilde{\Gamma}^i{}_{jk}$ are the Christoffel symbols associated with the conformal metric $\tilde{\gamma}_{ij}$.

The evolution equations for BSSN are then

$$\partial_t\chi = \frac{1}{3}\alpha\chi K - \frac{1}{3}\chi\,\partial_k\beta^k + \beta^k\,\partial_k\chi \, , \tag{A.19}$$

$$\begin{aligned}\partial_t\tilde{\gamma}_{ij} &= -2\,\alpha\tilde{A}_{ij} + \tilde{\gamma}_{ik}\,\partial_j\beta^k + \tilde{\gamma}_{jk}\,\partial_i\beta^k \\ &\quad - \frac{2}{3}\,\tilde{\gamma}_{ij}\,\partial_k\beta^k + \beta^k\,\partial_k\tilde{\gamma}_{ij} \, ,\end{aligned} \tag{A.20}$$

$$\begin{aligned}\partial_t K &= -\gamma^{ij}D_iD_j\alpha + \alpha\left(\tilde{A}_{ij}\tilde{A}^{ij} + \frac{1}{3}K^2\right) \\ &\quad + \beta^i\partial_i K + 4\pi\,\alpha(\rho + S) \, ,\end{aligned} \tag{A.21}$$

$$\begin{aligned}\partial_t\tilde{A}_{ij} &= \chi^2\left[-D_iD_j\alpha + \alpha\left(R_{ij} - 8\pi\,\alpha\,S_{ij}\right)\right]^{\mathrm{TF}} \\ &\quad + \alpha(K\tilde{A}_{ij} - 2\tilde{A}_{il}\tilde{A}^l{}_j) \\ &\quad + \tilde{A}_{ik}\,\partial_j\beta^k + \tilde{A}_{jk}\,\partial_i\beta^k \\ &\quad - \frac{2}{3}\tilde{A}_{ij}\,\partial_k\beta^k + \beta^k\,\partial_k\tilde{A}_{ij} \, ,\end{aligned} \tag{A.22}$$

$$\begin{aligned}\partial_t\tilde{\Gamma}^i &= 2\,\alpha\left(\tilde{\Gamma}^i_{jk}\tilde{A}^{jk} - \frac{2}{3}\,\tilde{\gamma}^{ij}\partial_j K - 3\tilde{A}^{ij}\frac{\partial_j\chi}{\chi}\right) \\ &\quad - 2\tilde{A}^{ij}\,\partial_j\alpha + \beta^k\partial_k\tilde{\Gamma}^i \\ &\quad + \tilde{\gamma}^{jk}\partial_j\partial_k\beta^i + \frac{1}{3}\,\tilde{\gamma}^{ij}\partial_j\partial_k\beta^k \\ &\quad + \frac{2}{3}\,\tilde{\Gamma}^i\,\partial_k\beta^k - \tilde{\Gamma}^k\partial_k\beta^i - 16\pi\,\alpha\,\tilde{\gamma}^{ij}\,S_j \, .\end{aligned} \tag{A.23}$$

The scalar field matter evolution equations are

$$\partial_t \phi = \alpha \Pi_M + \beta^i \partial_i \phi \,, \tag{A.24}$$

$$\begin{aligned} \partial_t \Pi_M = {} & \beta^i \partial_i \Pi_M + \alpha \partial_i \partial^i \phi + \partial_i \phi \partial^i \alpha \\ & + \alpha \left(K \Pi_M - \gamma^{ij} \Gamma^k_{ij} \partial_k \phi + \frac{dV}{d\phi} \right) \,, \end{aligned} \tag{A.25}$$

where the second order Klein Gordon equation has been decomposed into two first order equations as is usual. The stress energy tensor for a single scalar field is

$$T_{ab} = \nabla_a \phi \nabla_b \phi - \frac{1}{2} g_{ab} (\nabla_c \phi \, \nabla^c \phi + 2V) \,. \tag{A.26}$$

and the various components of the matter stress tensor are calculated from this as

$$\begin{aligned} & \rho = n_a \, n_b \, T^{ab} \,, \quad S_i = -\gamma_{ia} \, n_b \, T^{ab} \,, \\ & S_{ij} = \gamma_{ia} \, \gamma_{jb} \, T^{ab} \,, \quad S = \gamma^{ij} \, S_{ij} \end{aligned} \tag{A.27}$$

The Hamiltonian constraint is

$$\mathcal{H} = R + K^2 - K_{ij} K^{ij} - 16\pi\rho \,. \tag{A.28}$$

The Momentum constraint is

$$\mathcal{M}_i = D^j (\gamma_{ij} K - K_{ij}) - 8\pi S_i \,. \tag{A.29}$$

A.3 Specific Numerical Details

A.3.1 Initial Conditions, Convergence and Stability

To simulate Axion stars we use GRCHOMBO, a 3+1D numerical general relativity solver with full adaptive mesh refinement (AMR). Some generic details regarding the code are provided in Appendix A.2 above, including the evolution equations and numerical methods. In this section we provide further details specific to this work. Whilst the full 3+1D formulation is clearly not necessary for a spherically symmetric solution like an Axion star, we intend to expand the work in future to non-spherically symmetric cases, and thus we were content to sacrifice some efficiency in this simpler case in order to build our skills for future work with this code.

In our simulations, the gauge variables are initially are chosen in accordance with the spherical oscilloton solutions in polar-areal coordinates, as detailed in the main text, and then transformed into cartesian coordinates. This was done by interpolating a Mathematica solution for the gauge, metric and extrinsic curvature variables in radial coordinates onto each gridpoint (using linear interpolation of values lying between the Mathematica solution points), and then transforming this into cartesian coordinates using the relevant Jacobian transformation at each grid point. The values of the $\tilde{\Gamma}^i$ were then calculated from the derivatives of the spatial metric, rather than interpolated onto the grid. In figure A.4 we show that the generated initial data has $\mathcal{O}(0.1\%)$ relative Hamiltonian violation. On subsequent slices the gauge variables are allowed to evolve away from the polar areal gauge dynamically, in accordance with the puncture gauge in Eq. (A.13). This gauge choice allows us to resolve and stably evolve spacetimes containing Black holes without excision, but requires some care when interpreting results.

In cases of Black hole formation we see the expected "collapse of the lapse" and the solution quickly stabilises into the "trumpet" puncture solution described in [282]. We remove the effect of the changing lapse by plotting against the proper time τ rather than simulation time t for central values. This is achieved by integrating the lapse at each timestep. In other cases the lapse is of order 1 so simulation time is approximately equal to proper time locally. Modulo numerical error, the shift vector is always zero at the origin due to spherical symmetry.

The presence of a Black hole event horizon is gauge invariant. We use an apparent horizon finder which assumes spherically symmetry to identify marginally trapped surfaces on each spatial slice. Whilst these are local rather than global horizons, if we detect an apparent horizon on a time slice, the singularity theorems tell us that it must lie inside an event horizon (see, for example, section 7.1 of [155]). Thus if we detect an apparent horizon we can infer that a Black hole has formed, and the area of the apparent horizon provides a lower bound on the Black hole mass. Note that the converse is not true – the absence of an apparent horizon does not imply the absence of an event horizon.

For all our simulations we use a minimum of three fixed levels of refinement to get good spatial resolution, and add additional levels above this dynamically in response to the scales which develop in each case. The coarsest grid is 64^3 and has a physical length of $128m^{-1}$, and the refinement ratio at each level is 2. The conditions for AMR are based on the gradients of χ, the conformal factor. Depending on whether a Black hole formation occurs or whether the field disperses, we typically use a maximum of 5-8 levels of refinement.

We checked the convergence of the code in a fixed mesh refinement (FMR) case by tracking the difference in the value of ϕ when the highest refinement level was doubled succesively over three simulations. The results are shown in figure A.2, in which 3.5th order convergence is demonstrated, which is consistent with the spatial stencils and time integration used. For a selection of full AMR simulations, we repeated the runs with an additional grid and more aggressive threshold for refinement, to check that the same phenomena were observed and thus that the code had converged sufficiently. In addition, we track the relative violation of the Hamiltonian constraint at each timestep, calculated as

$$\mathcal{H}_{rel} = \frac{\mathcal{H}}{16\pi\rho_{avg}}, \tag{A.30}$$

with ρ_{avg} the average density inside the star. We define $\rho_{avg} = M_{ADM}/V_{Star}$, with $V_{Star} = vol(\{x \in \mathbb{R}^3 \mid \rho(x) \ > 0.05\max(\rho(x))\})$. We also measure the absolute violation of the Momentum constraint. We find that these remain stable and bounded throughout the simulation, see Figure A.3 and Figure A.5, although the absolute violation in the Momentum constraint increases somewhat during Black hole formation.

To determine the end state for an Axion star we simulated the star for approximately 87 crossing times of the numerical grid. We use Sommerfeld boundary conditions [279], which allow outgoing waves to exit the grid with minimal reflections in the case of a ϕ^2 potential. Whilst we consider a non free-field case, at the boundaries the field is near the minimum and therefore only probes the $m^2\phi^2$ part of the potential. We thus expect the condition to work reasonably well despite the additional self interaction terms. However, since we evolve for several crossing times, we must consider the possible effect of reflections on our results, which are difficult to quantify. Even though boundary conditions were used which allowed radiation to exit the grid, it is inevitable that some reflections will have occurred, and this adds uncertainty to any numerical values extracted from the final state.

We estimated that the reflected energy was of the order of $10^{-4}M_{pl}^2/m_a$ on the first reflection, and thus it was unlikely to significantly affect our results. We show in figure A.6 a plot of the mass of the apparent horizon, which quickly stabilises around a fixed value, showing that it is not significantly affected by reflections at later times. We also show in the same figure the ADM mass, calculated from ADM variables extracted on the surface of a square box with width 25.4 $1/m_a$, centred at $r = 0$. The ADM mass remains relatively constant during the simulation, which gives additional evidence that the boundaries are not significantly reflecting energy back into the domain.

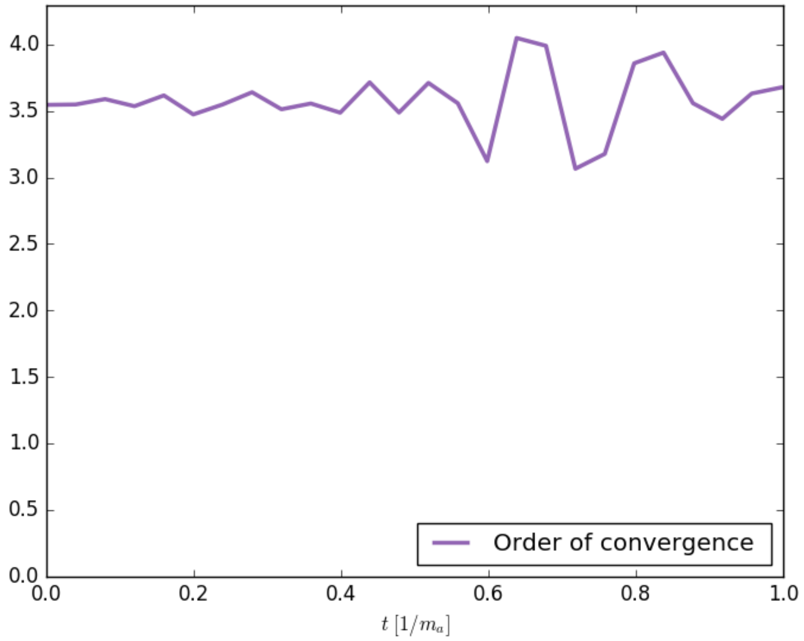

Fig. A.2 **FMR Covergence test.** We tested the convergence of the code in an FMR setup, in three runs with finest mesh spacings of $h_1 = 0.125$, $h_2 = 0.0625$ and $h_1 = 0.03125$. The results are shown in the figure, which demonstrates that the code has ≈ 3.5th order convergence. There is some loss of the expected 4th order, but this is partly due to interpolation errors when comparing solutions (since we use a cell centred grid, the cell centre at each additional refinment level is $\Delta x/2$ from that of the level below).

In addition, we checked the final state for $f_a/\sqrt{2} = 0.100$ and $\phi_{1,\mathrm{osc}}(0) = 0.15$, which has an initial total energy of 2.50 M_{pl}^2/m_a. After 87 light crossing times the total energy which remains in our grid is 2.25×10^{-9} M_{pl}^2/m_a. This indicates that the majority of the initial energy was dispersed and has been able to exit the grid. Additionally, we checked the final state for $f_a/\sqrt{2} = 0.040$ and $\phi_{1,\mathrm{osc}}(0) = 0.2$, which forms a Black hole. We simulate this case for 2.34 light crossing times which covers the period before and shortly after BH formation. The initial mass of the system is 2.62 M_{pl}^2/m_a, and this is found to be mostly absorbed into the Black hole which has a final mass of 2.0 M_{pl}^2/m_a. Although the exact value of the mass might be somewhat influenced by reflections, the formation of the Black hole occurs well before these could interfere with the dynamics of the system, so we are in no doubt that this is the correct end state. Our ability to evolve the quasi-stable solutions with a modulating self interaction over several periods is further evidence that reflections are not significantly contaminating our results.

A further constraint of the finite grid comes from the fact that, in cases where most of the Axion star mass gets ejected, the end state could be another low mass Axion star. Since the

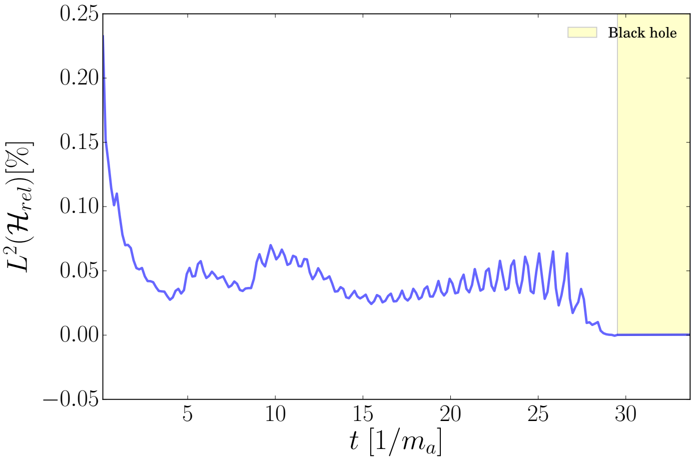

Fig. A.3 **Relative Hamiltonian constraint violation, L2 norm** $(M_{\mathrm{ADM}}, f_a) = (0.85, 0.25)$. The L2 norm $||f||_2 = \sqrt{\frac{1}{V}\int_V f^2 dV}$ of the relative Hamiltonian constraint violation (as defined in Eqn. (A.30)) for a case of Black hole formation. We excise the interior of the Black hole apparent horizon after it forms. Because the definition of the relative density does not make sense anymore after Black hole formation, we continue to use the value from shortly before the apparent horizon appears. We used a short relaxation routine for χ initially, in addition to the numerical solution, to improve the initial constraint violation.

radius of the Axion star increases with decreasing mass, if the final Axion stars are very low mass, and thus bigger than the initial grid, they will be impossible to resolve. This means that the size of the grid puts a lower bound on the mass of any oscillotons which can be identified as the final states of our system. However, this is a relatively small value, approximately 0.46 M_{pl}^2/m_a, and thus we say that the star has dispersed in these cases.

A.3.2 Complex PQ field versus real axion field

In this section, we comment on the mapping between S^1 and $\mathbb{R}^1$ for the axion field. For field values of the form $\varphi = f_a e^{i\phi/f_a}/\sqrt{2}$, the potentials in Eq. (2.4) and (2.5) should be equivalent, but with the significant difference that the real potential has distinct vacua and the complex one does not – going “over the potential hill" takes you back to where you started. However, because we have fixed our boundary conditions at infinity to be at the same central minimum in all directions, and assuming continuity in the solutions, we cannot have any charges corresponding to the distinct vacua, and therefore there should be no physical difference between the two, provided that the radial field stays in the minimum of the potential ring. This means that one should obtain the same results using a real scalar field and a real cosine potential, as would be obtained for the full complex potential, provided that

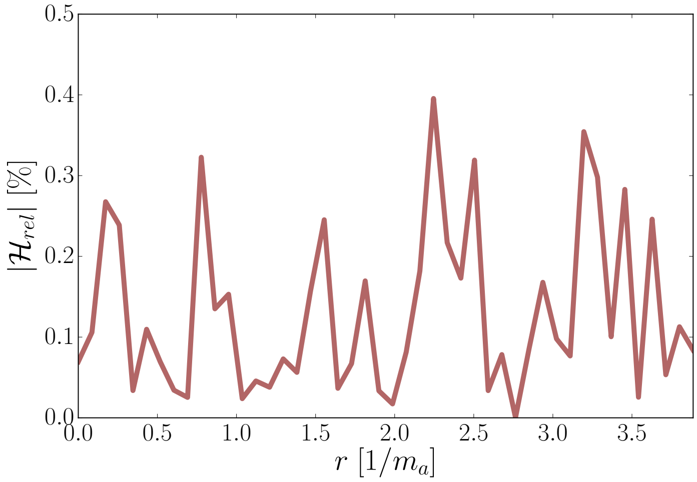

Fig. A.4 **Relative Hamiltonian constraint violation for initial conditions, radial profile** $(M_{\rm ADM}, f_a) = (0.85, 0.25)$. Initial relative Hamiltonian constraint violation, as defined in Eqn. (A.30). The zero radius marks the center of Axion star. The momentum constraint is identically zero initially, since $K_{ij} = 0$ and $S^i = 0$, so no plot is provided for this.

the radial oscillations in the complex case are small. We have confirmed that this is the case, as detailed below.

The full complex potential for the PQ field is given by Eq. (2.4).[3] We consider solutions in the broken phase of PQ symmetry, i.e. with the radial mode $\rho = f_a$ everywhere.

Although ρ is much heavier than the axion, and so naively can be integrated out and set to a constant, strong gravitational effects in Axion stars could destabilize the radial mode. We investigate radial mode stability by simulating the full complex-valued PQ field. We define our initial conditions in this case using

$$\varphi = \frac{f_a}{\sqrt{2}} e^{i\phi/f_a}, \tag{A.31}$$

to map the Axion star initial data, in ϕ, to the equivalent values for the complex PQ field φ.

Simulating the radial mode and the full complex field is computationally challenging due to the hierarchy of masses between ρ and ϕ: steep potential "walls" imply the radial oscillations have much shorter time-scales than the angular ones and therefore require higher temporal resolution. We performed a small number of simulations of the complex field, to demonstrate that stability of the radial mode can be ensured.

---

[3] An additional term must be added in the potential to ensure that we have zero vacuum energy at the minimum, such that V becomes $V' = V + \bar{V}$. Naively, $\bar{V} = \varepsilon f_a$ by expanding the potential. However, due the breaking of the shift symmetry the effective minimum moves slightly and the values must be adapted accordingly.

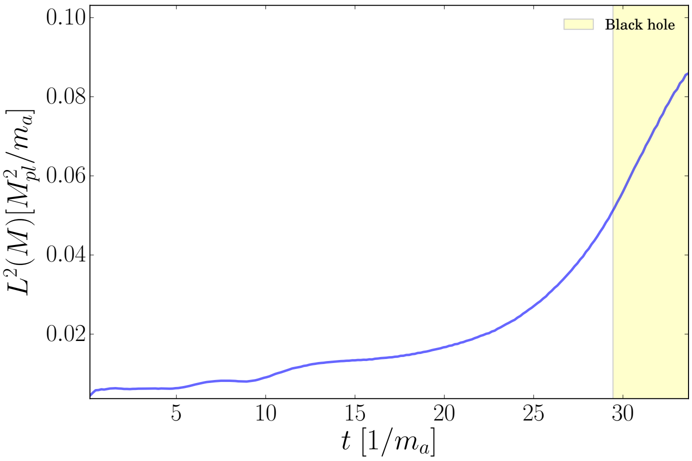

Fig. A.5 **Absolute Momentum constraint violation.** $(M_{\mathrm{ADM}}, f_a) = (0.85, 0.25)$. The L2 norm ($||f||_2 = \sqrt{\frac{1}{V}\int_V f^2 dV}$) of the absolute momentum constraint violation for a case of Black hole formation. Even though the initial data is not time-symmetric ($\Pi \neq 0$), K_{ij} and S^i are zero everywhere, therefore the momentum-constraint is trivially satisfied initially.

The results of these simulations are shown in Fig. A.7. The left panel shows the evolution of the radial mode, while the right panel compares the evolution of the axion field in the complex ($\varepsilon\varphi_1$) and real (cosine) simulations. We notice that the radial mode undergoes small (sub-percent) oscillations at high frequency. The radial frequency is increased, and the amplitude reduced, as we increase λ_φ (which sets the mass of ρ). The axion field evolution in both simulations agrees at the sub-percent level, with agreement also increased as we increase λ_φ.

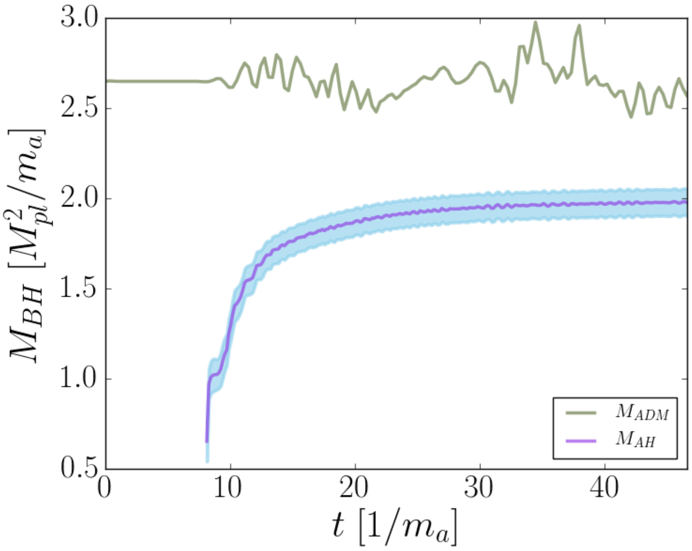

Fig. A.6 **Apparent horizon and ADM mass versus time** Evolution of the $(M_{\rm ADM}, f_a) = (2.63, 0.055)$, R2 star in Fig. 2.1. Evolution of the Black hole apparent horizon mass and ADM mass over time. The blue shaded area indicates the potential error due to resolution when measuring the radius of the AH. The AH mass increases as more matter is accreted, as expected, and stabilises at a relatively constant value, indicating that it is not significantly affected at later times by reflections. The ADM mass remains relatively constant. The later perturbations are caused by scalar fields propagating through the boundary which we use to measure it. These may be in part due to reflections from the boundary, but appear to remain well bounded and do not grow.

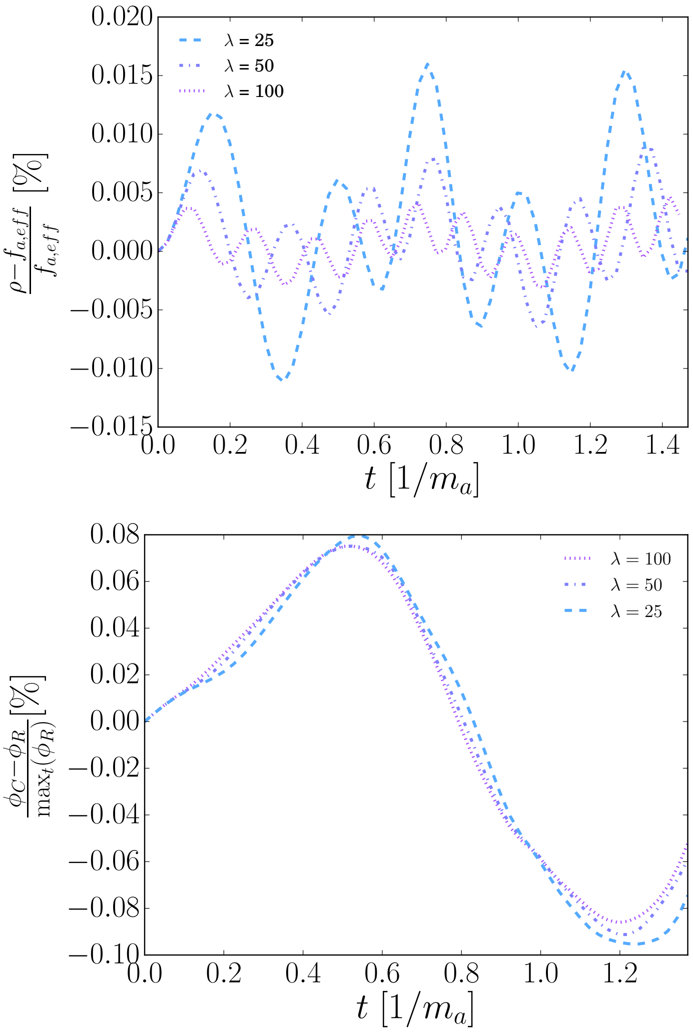

Fig. A.7 **Radial field stability.**Time evolution of the full complex field for different values of λ_φ for $f_a = \sqrt{8\pi}\sqrt{2}$, for which the evolution is oscilloton like. The panel on the left shows the radial modes $|\varphi|$, and the one on the right shows the difference between complex and real field evolution. Values in the left panel of ± 100 % would indicate that the radial mode is unbounded, that is, that it can go “over the top” of the central point. However, it can be seen that its values are extremely well bounded, justifying the use of the real potential as equivalent to that of the full complex one. The plots cover one period of the angular oscillation, which contains multiple periods in the radial amplitude.

Appendix B

Formation of Relativistic Axion Stars

B.1 Two Pass Connected Component Labelling

The connected component labelling (CCL) procedure assigns a unique label to a set of connected target pixels in a binary image [283]. We can construct a binary image from an 2D array, in our case the energy density of the ϕ field generated by our toy power spectrum, by assigning a 0 to all elements in the array that are below a cutoff threshold, and a 1 to all those that are above. A subset of the binary image is called connected if for any two points P and Q of the subset there exists a sequence of points $P = P_0, P_1, P_2 ..., P_{n-1}, P_n = Q$ such that P_i is a neighbour of P_{i-1} [284]. The definition of a connection relies on that of a pixel's neighbourhood, if this includes 4 neighbours it is said to be 4-connected, and if it includes 8 neighbours it is said to be 8-connected [285].

We use a specific group of CCL, known as two-pass algorithms, to label peaks. Two pass complete labelling in two scans: during the first scan they assign provisional labels to pixels and record label equivalencies. Label equivalencies are the resolved during or after the first scan. During the second scan, all equivalent labels are replaced by their representative label [286, 287]. We use a two-pass algorithm that use 4-connected to define a connection. Algorithmically, we did the following:

```
loop p
    if $p > 0$ then
        if p above !=0 and p left =0 then
            pl = pl above
        else if p above =0 and p left !=0 then
            pl = pl left
        else if p above !=0 and p left !=0 then
            pl = min(pl above, pl left)
            record pl dependancy
        else
            pl = new label
        end if
    end if
end loop
```

where p is a pixel, pl is a pixel label, and min is a function that chooses the minimum of two values. The label equivalencies were then processed such that consecutive labels where generated, and then a second pass would the replace all equivalent labels. This algorithm provides a description of how the peaks where labelled. The Numpy [3] CCL algorithm was used for the analysis presented in this work.

B.1.1 Constructing Initial data

We construct our initial data in the same was as in [288], however the key details of the method are reproduced here for convenience. We choose $\alpha = 1$ and $\beta_i = 0$ and hence on the initial hypersurface the initial gradient energy is

$$\rho_{grad} \equiv \frac{1}{2}\gamma^{ij}\partial_i\phi\partial_j\phi \; . \tag{B.1}$$

We also introduce the notation for the kinetic term

$$\eta = \frac{1}{\alpha}\left(\partial_t\phi - \beta^k\right) \; , \tag{B.2}$$

which is zero on our initial hypersurface. Hence initially

$$\rho = \frac{1}{2}\gamma^{ij}\partial_i\phi\partial_j\phi + V \; . \tag{B.3}$$

Our constraint equations become

$$\tilde{D}^2\chi - \frac{5}{4\chi}\tilde{\gamma}^{ij}\tilde{D}_i\chi\tilde{D}_j\chi + \frac{\chi\tilde{R}}{2} + \frac{K^2}{3} - \frac{1}{2}\tilde{A}_{ij}\tilde{A}^{ij} = 8\pi G\rho \, , \tag{B.4}$$

and

$$\tilde{D}_j\tilde{A}^{ij} - \frac{3}{2\chi}\tilde{A}^{ij}\tilde{D}_j\chi - \frac{2}{3}\tilde{\gamma}^{ij}\tilde{D}_jK = 8\pi G\eta\tilde{\gamma}^{ij}\partial_j\phi \, . \tag{B.5}$$

Next we want to specify the initial conditions for the metric γ_{ij} and the extrinsic curvature K_{ij}. We can make the simplifying assumption that the metric is conformally flat and the traceless part of the extrinsic curvature K_{ij} is zero everywhere on the initial hyperslice

$$\tilde{\gamma}_{ij} = \delta_{ij} \,, \tag{B.6}$$

and

$$\tilde{A}_{ij} = 0 \,. \tag{B.7}$$

We now need to specify the values of K and χ on the initial hyperslice. Eq. B.5 is trivially satisfied for $K = const$, however, in order to satisfy Eq. B.4, and the periodic boundary conditions, $K^2/24\pi$ needs to lie close to the average initial energy density for the hypersurface. Therefore for simplicity we choose it equal to the average initial energy density, approximating the metric to be Euclidean

$$K = -\sqrt{24\pi G\langle\rho\rangle} \,, \tag{B.8}$$

with

$$\rho = \frac{1}{2}(\partial_i\phi)^2 + V(\phi) \,, \tag{B.9}$$

where $\langle X\rangle = \mathcal{V}^{-1}\int X \; d\mathcal{V}$ indicates the average over the spatial volume $\mathcal{V}$ of the quantity X. Once K is chosen, the initial field profile and the Hamiltonian constraint then fully determine the conformal factor χ (which we solve for using numerical relaxation).

B.1.2 AMR Condition

All simulations shared a coarsest grid of 64^3. Locally, the scale-factor of our spacetime is roughly

$$a \equiv \frac{1}{\sqrt{\chi}}, \tag{B.10}$$

which is not a true comparison, since the scale-factor a from FRW assumes a homogeneous space-time, however, it is still a useful measure.

Since the timescale of formation of objects varies, this means that the physical length scales of the problem do not necessarily track the grid, and hence requires a rescale regridding threshold. We set our threshold to be triggered by high gradients in K and a scaled version of the gradients of ρ. These conditions track gravitational collapse in our simulations. For

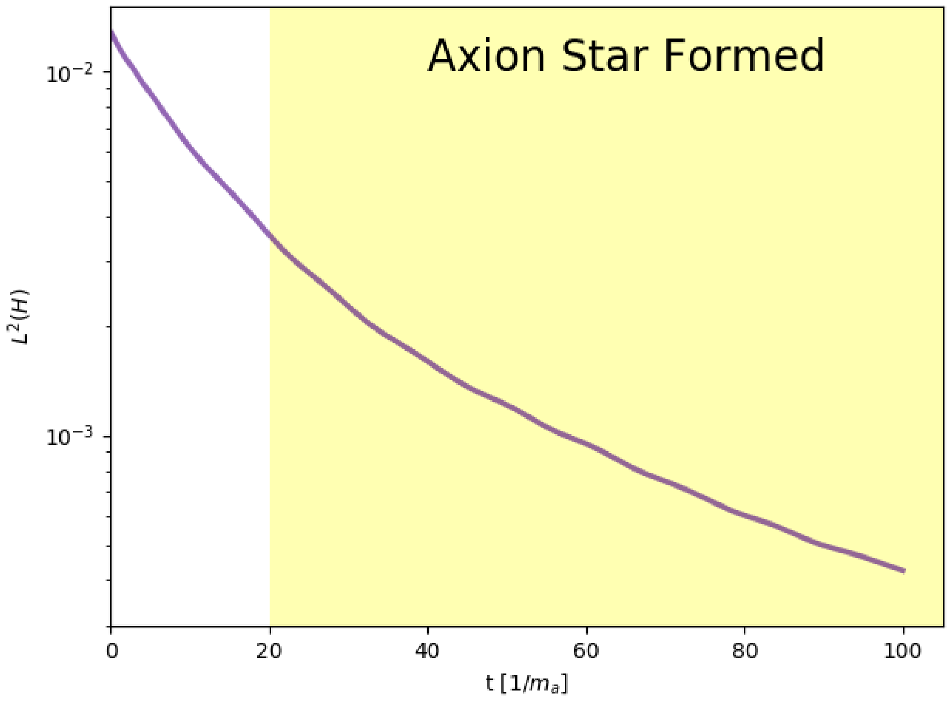

Fig. B.1 The plot shows the L^2 norm Eq. B.11 of the Hamiltonian constraint violation over time for a simulation that forms an Axion star, with an initial total mass of $M = 1.34$ $M_\odot\, 10^{-10}$eV m_a^{-1}, $f_a = 5.0\ M_{pl}$ and $\tilde{L} = 16\ m_a^{-1}$. The spikes in the plot are due to the regridding in the simulation and are rapidly damped.

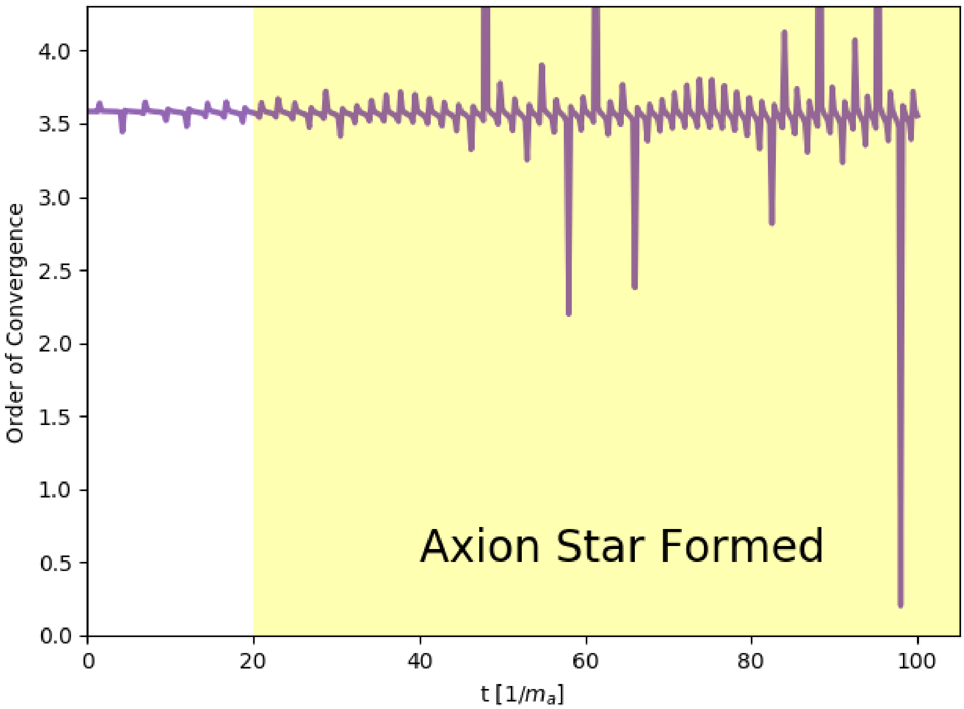

Fig. B.2 Convergence test for ϕ_{center} showing a convergence between 3rd and 4th order. The convergence test is done with a fixed grid with three different resolutions of 0.25 m_a^{-1}, 0.125 m_a^{-1} and 0.0625 m_a^{-1}. Our evolution scheme is 4th order and the variation in the convergence is due to ϕ passing through 0 during the evolution.

$\tilde{L} = 16$ we scaled our regridding of the gradients of ρ as

$$\rho_t \frac{\nabla \rho}{\sqrt{\chi}},$$

where ρ_t is a numerical regridding threshold set at the beginning of the simulation. It was set to a value of $20\rho^{star}_{max}$, where ρ^{star}_{max} is the maximum value of ρ that a star of half total box mass would have. If half the total box mass was greater then the most stable Axion star, then ρ^{star}_{max} was set to be the for the highest stable Axion star. For $\tilde{L} = 64$ and $\tilde{L} = 128$ we found that this condition was not enough for optimum regridding. Below an amount of layers (3 for 64, and 4 for 128), we added an additional regrid condition

$$\rho_a \frac{\nabla \rho}{\chi^{\frac{3}{2}}},$$

where ρ_a is an additional regridding threshold. ρ_a was chosen to be $10\rho^{box}_{max}$, where ρ^{box}_{max} is the maximum value of ρ in the simulation at $t = 0$. Once the correct thresholds where chosen, these regrid conditions would effectively follow the gravitational collapse in the simulations.

B.1.3 Convergence and Stability

We use the following to measure the volume averaged Hamiltonian constraint violation:

$$L^2(H) = \sqrt{\frac{1}{V}\int_V |\mathcal{H}^2| dV}, \tag{B.11}$$

where V is the box volume with the interior of the apparent horizon excised. As can be seen in B.1, we have good control over the constraint violation throughout the simulation.

We test the convergence of our simulations with the formation of an Axion Star with initial total mass of $M = 1.34\ M_{\odot}\ 10^{-10}\text{eV}\ m_a^{-1}$, $f_a = 5.0\ M_{pl}$ and $\tilde{L} = 16\ m_a^{-1}$. We use a fixed grid for the convergence test with resolutions of $0.25\ m_a^{-1}$, $0.125\ m_a^{-1}$ and $0.0625\ m_a^{-1}$. The results are shown in B.2, where we obtain an order of convergence between 3rd and 4th order on average. The variation of the in the convergence test is due to the methodology, where we extract values of ϕ at the centre of the grid. ϕ passes through 0 during the evolution, that causes the spikes present in the convergence test.

B.1.4 Axion Star Location

To confirm the that a resulting object was an Axion star, and to track its subsequent evolution, an “Axion star finder" script was written, and ran in post-processing. The finder would look at the density in the simulation, and locate the value and location of it’s maximum, ρ_{max}. The radius in x-direction for which the value of ρ had dropped to 5% of ρ_{max} was calculated, and then the total mass was defined as the integrated density within a sphere of that radius. The radius of the object was adjusted for expansion.

In Fig. 3.4, there are some points that can be considered to be outliers. When the script looks for the maximum value and location of ρ, if at that point in time there are two maximum points in the central region, it causes the script to not return the true radius of the object, and hence the calculated mass will also not be correct. This was not a frequent occurrence, and the cause of it is easily confirmed.

Appendix C

Gravitational Wave Emission from Collisions of Compact Scalar Solitons

C.1 Numerical Methodology

C.1.1 Constructing Initial Data

We solve for single oscillaton (OS) profile for ϕ, π, γ_{ij} at some initial hyperslice $t = t_0$ as described in Refs. [203, 55, 67, 56] where $\pi = \alpha^{-1}(\partial_t \phi - \beta^i \partial_i \phi)$ is the initial kinetic term of the scalar, and γ_{ij} is the 3-metric defined as usual in the ADM line element

$$ds^2 = -\alpha^2 dt^2 + \gamma_{ij}(dx^i + \beta^i dt)(dx^j + \beta^j dt). \tag{C.1}$$

The determinant of the spatial metric γ will be denoted by $\det\gamma$. We also set the extrinsic curvature $K_{ij} = 0$.

Given this single oscillaton profile, we generate static OS-OS initial data by superposing two single OS solutions:

$$\begin{aligned} \phi_{\text{tot}} &= \phi|_{x-x_0} + \phi|_{x+x_0} \\ \pi_{\text{tot}} &= \pi|_{x+x_0} + \pi|_{x-x_0} \\ \gamma_{ij,\text{tot}} &= \gamma_{ij}|_{x+x_0} + \gamma_{ij}|_{x-x_0} - h_{ij} \end{aligned} \quad , \tag{C.2}$$

where $\pm x_0$ are the locations of the centers of the two oscillatons, and h_{ij} is a constant metric. The choice of h_{ij} turns out to be important in setting up the initial conditions. Naively, one would use $h_{ij} = \delta_{ij}$, which would make the asymptotic values the same as for a single OS.

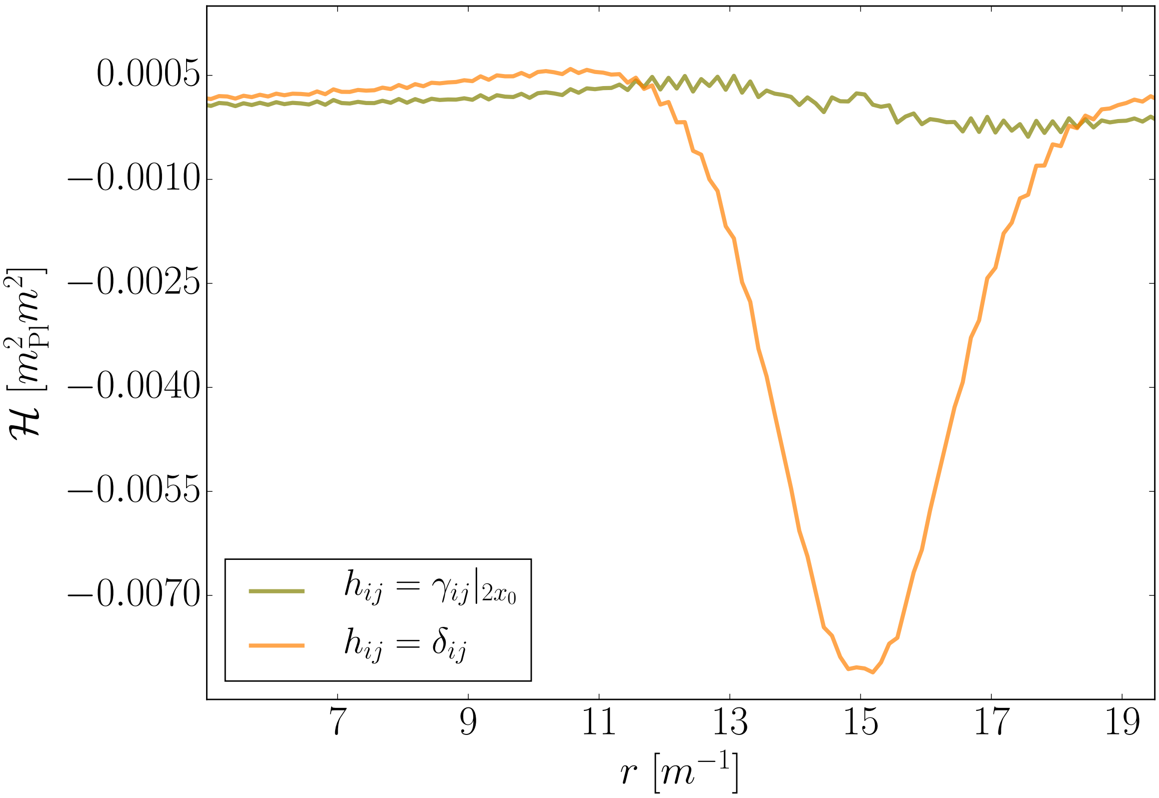

Fig. C.1 The Hamiltonian constraint violation of the OS-OS initial data before relaxation for $\mathcal{C} = 0.13$ along the axis of the two OS. By choosing $h_{ij} = \gamma_{ij}|_{2x_0}$ the relative Hamiltonian constraint violation (Eq. C.1.1) is reduced by a order of magnitude from 2.6 % to 0.3 %. An additional relaxation routine in χ is implemented after this improvement is applied.

However, this choice induces large radial modes in both oscillatons. These modes are caused by the change in the volume element near the center of each OS due to the influence of the companion (as compared to the case of an isolated OS). This difference is clearly seen in Fig. C.2, where the black curve is the volume element related to an isolated OS, whereas the orange curve is the volume element obtained by using $h_{ij} = \delta_{ij}$.

An estimate for the change in the volume element can be obtained as follows. Consider OS_1 at x_0, with its companion OS_2 located at $-x_0$. Assuming a Schwarzchild metric far from the surface of OS_1, the volume element at $-x_0$ due to OS_1 is $\sqrt{\det\gamma} = \sqrt{(1-2GM/d)^{-1}} \approx \mathcal{O}(1.01)$. We assumed a distance $d = 2x_0 = 60m^{-1}$ and $M \approx 0.5M_{\rm Pl}^2/m$. By subtracting off $h_{ij} = \delta_{ij}$, we are still left with $\sim 1\%$ extra volume at $x = -x_0$ compared to the case where OS_2 was isolated (and vice-versa for OS_1). That is, the oscillatons are “puffed up” initially. These radially excited OS are *not* the initial conditions we seek as they add additional energy and induce instabilities into the initial conditions for single oscillatons. In particular, the

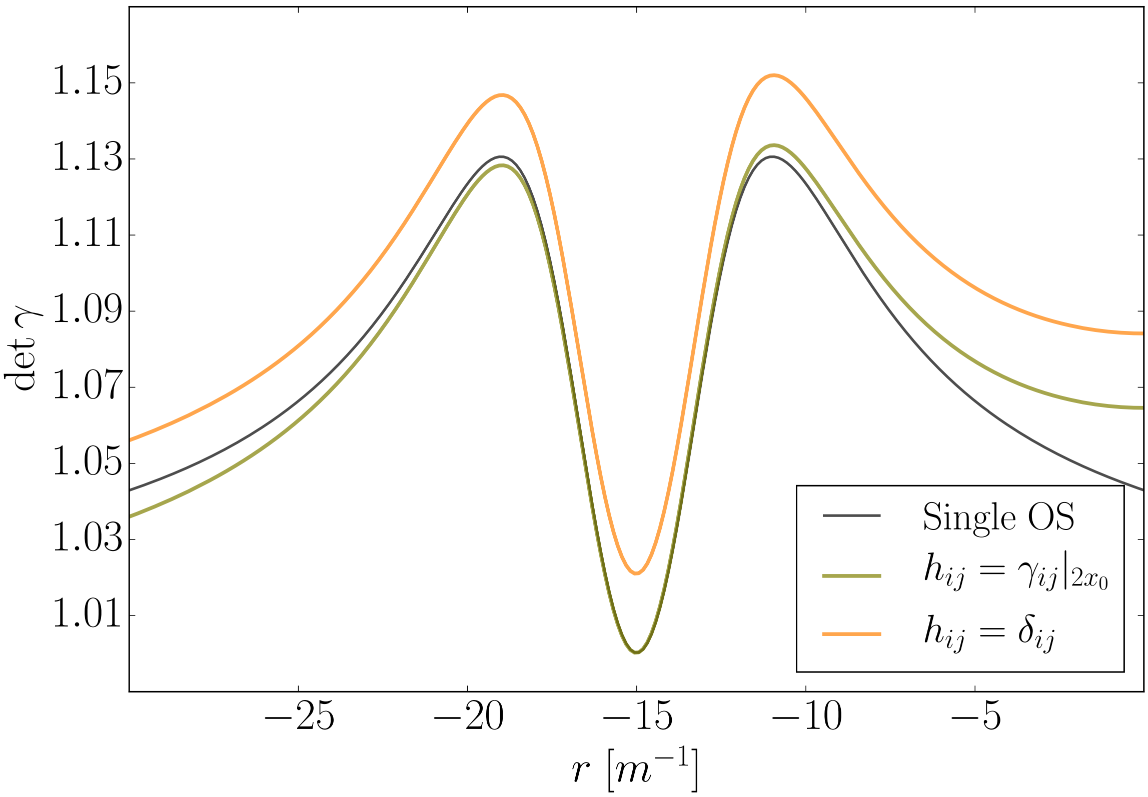

Fig. C.2 The volume element $\det\gamma$ of the OS-OS initial data before relaxation for $\phi_{m,0}(0) = 0.44$, $\mathcal{C} = 0.13$ on a line in the x direction which goes through the center of both OS. In this example, we have positioned the stars at distance $\pm 15\ m^{-1}$ as opposed to $\pm 30\ m^{-1}$ to illustrate our point. Note that the values are closer to the single OS solution when the metric values are conserved in the center of the OS.

central densities and radii of these excited OS can deviate from their unexcited counterparts by $\mathcal{O}(100\%)$ and $\mathcal{O}(10\%)$ respectively as they evolve, potentially rendering any results that we obtain unreliable.[1]

As quantitative test, we set up a single OS with compactness $\mathcal{C} = 0.10$, and then imposing a 0.1% perturbation in its radius achieved simply by remapping the field values with $r \to 0.999r$. This small change results in a large oscillating radial mode with a $\gtrsim 10\%$ fluctuation in maximum amplitude of the central density.[2] Not surprisingly, the radiated GW energy becomes strongly dependent on the choice of the initial separation causing varying results

---

[1] This is reminiscent of the old “self-crushing” problem in the set up of binary neutron stars initial conditions [289].

[2] An animation showing the evolution in time of the central density is available [290]

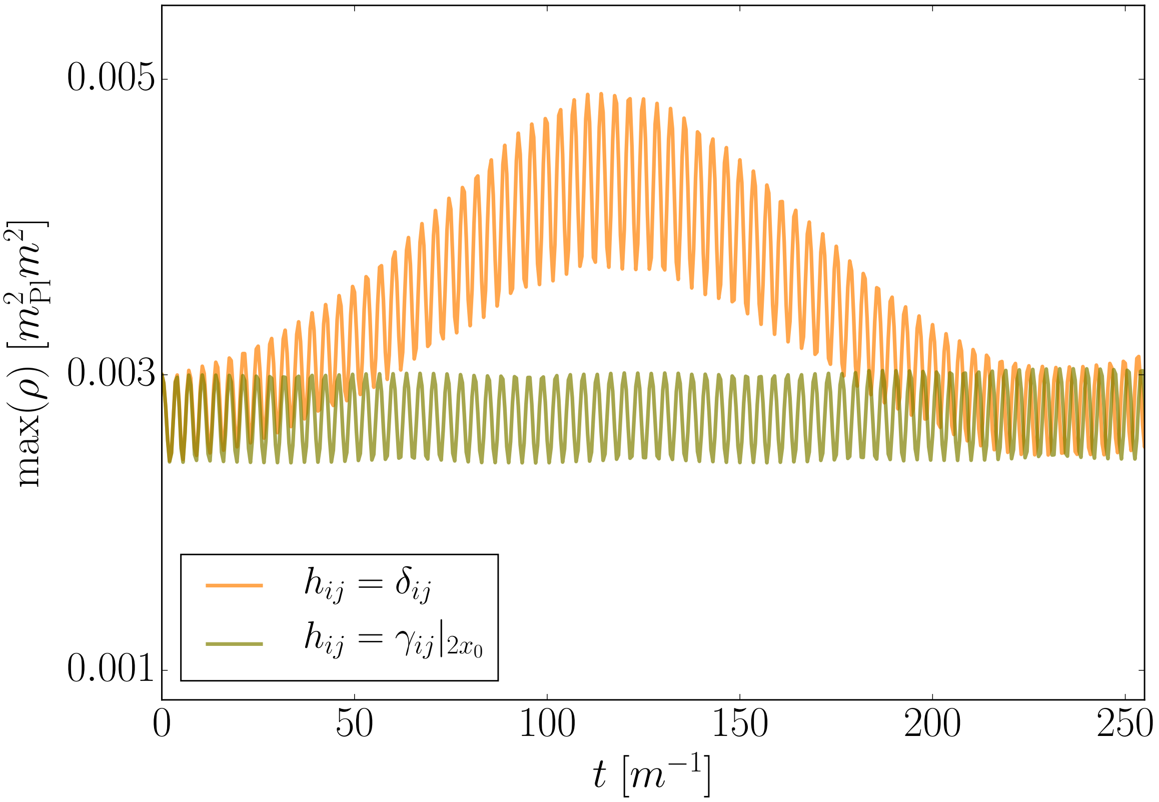

Fig. C.3 The plot shows the central density of OS with $\mathcal{C} = 0.10$ at a distance $60m^{-1}$ from its counterpart. The high frequency oscillation with wavelength $\lambda \approx 2\pi m^{-1}$ is the natural breathing of the oscillaton while the low frequency mode is caused by the radial mode. Applying the choice $h_{ij} = \gamma_{ij}|_{2x_0}$ removes this radial mode. Animations depicting the evolution of the central density with and without radial modes are available [25, 26] .

for different initial distances, thus making it a bad approximation for an unexcited OS falling in from infinity.

Our solution to this problem is to choose $h_{ij} = \gamma_{ij}|_{2x_0}$, which leaves the metric values at the center of each OS unchanged from the isolated case and thus also its volume element. From the close match between the green curve ($h_{ij} = \gamma_{ij}|_{2x_0}$) and the black curve (isolated OS) in Fig. C.2, one can see how this choice is a significant improvement over the orange curve ($h_{ij} = \delta_{ij}$).

Furthermore, defining the relative Hamiltonian violation as

$$\left(\frac{\mathcal{H}}{16\pi\rho}\right)\Big|_{x=\underbrace{argmax}_{x}(\rho)},$$

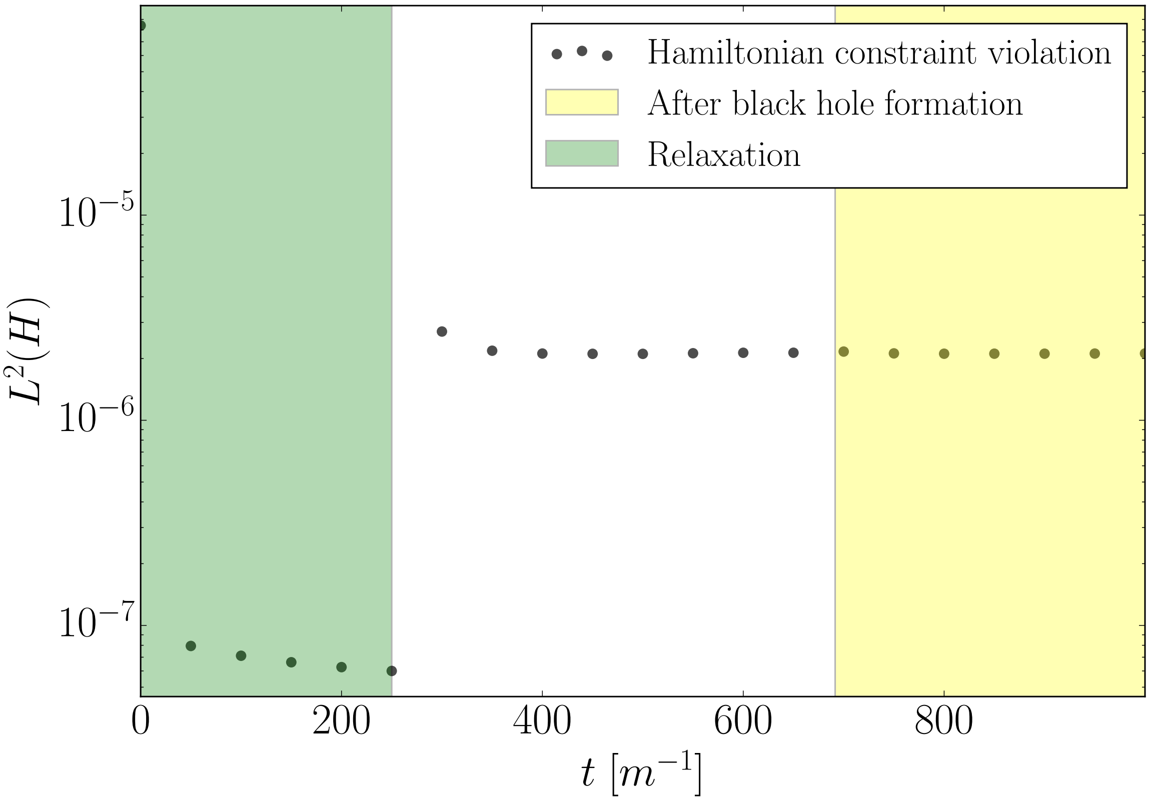

Fig. C.4 The plot shows the L^2 norm (Eq. B.11) of the Hamiltonian constraint violation over time, with excision of the black-hole interior (which forms around $t = 700$). The green region shows the relaxation time[3], with data points extracted every 100th coarsest time-step. There is a jump after the relaxation, likely caused by regridding during transition from relaxation to evolution, but still extremely good overall.

we see a significant improvement in relative violation from 2.6% to 0.3% (see Fig. C.1). Finally, we apply a relaxation routine to reduce this Hamiltonian constraint violation further. The result of our method is shown in Fig. C.3 where it is clear that we have eliminated the large low frequency radial modes (orange curve) to leave only the physical high frequency central density fluctuation present in the original single OS solution (green curve).

C.1.2 Numerical Methodology and Convergence Tests

All grids for extraction of gravitational waves have a side length of $512m^{-1}$, with the coarsest resolution being $\Delta x = 2m^{-1}$. We extract $r\Psi_4$ at a radius of $60m^{-1}$ and we set a fixed resolution over the region containing the extraction sphere. Depending on the scenario, we use from five to six levels of refinement, which corresponds to a smallest resolution of

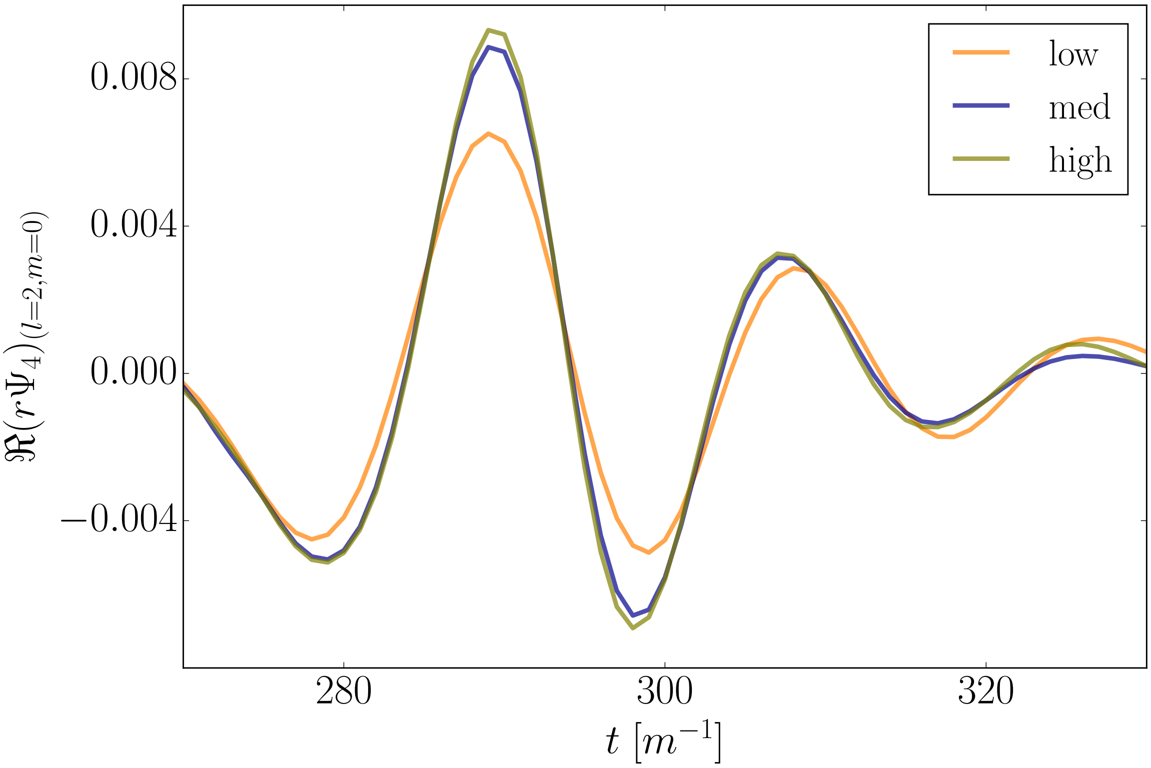

Fig. C.5 Convergence test for the $l = 2$, $m = 0$ mode of $r\Psi_4$, showing convergence between 2nd and 3rd order. The convergence test is done with three different coarsest resolutions of $4m^{-1}$, $2m^{-2}$ and $1m^{-1}$, 6 levels of $2:1$ refinement, with corresponding finest resolutions of $0.0625m^{-1}$, $(0.0625/2)m^{-1}$ and $(0.0625/4)m^{-1}$. Our evolution scheme is 4th order, and the lowered accuracy is due to the large amount of re-gridding required to track the motion of the oscillaton through to final state.

$0.0625m^{-1}$ and $0.03125m^{-1}$, respectively. Since for all simulations the boxsize is $500m^{-1}$ and our extraction sphere is positioned at radius $60m^{-1}$ from the center, we choose the maximum run-time at around $380m^{-1}$ in order to prevent spurious reflections at the boundary from contributing to the final results.

We use the following to measure the volume averaged Hamiltonian constraint violation as in Eq. B.11. As can be seen in Fig. D.2, we have good control over the constraint violation throughout the simulation. As can be seen in Fig. C.4, we have good control over the constraint violation throughout the simulation.

We test the convergence of our simulations with the collision of two oscillatons with $\phi_{m,0}(0) = 0.33$ ($\mathcal{C}= 0.20$). We use a box of sidelength $256m^{-1}$, and initial separation of the oscillatons of $40m^{-1}$. As we have turned on adaptive refinement, we use three different coarse resolutions of $1m^{-1}$, $2m^{-1}$ and $4m^{-1}$. This allows for 6 levels of $2:1$ refinement each with corresponding finest possible resolutions of $0.015625m^{-1}$, $0.03125m^{-1}$ and $0.0625m^{-1}$. We extract the $l = 2$, $m = 0$ mode of $r\Psi_4$ at distance $60m^{-1}$ from the center. The results are shown in Fig. C.5, where we obtain between 2nd and 3rd order convergence on average. While we have used a 4th order scheme, the large amount of re-gridding required to track the collision results in some loss of accuracy which is not surprising.[4] Lastly, we note that an estimate for the error bars in the energy extraction (Fig. 4.1) is obtained by doubling the resolution of the simulations described in the main text, and computing the energy for this higher resolution case. The difference of the results at two different resolutions gives us an estimate for the error.

C.2 Self-Interactions

In our study we have ignored possible self-interactions of the scalar field ϕ. Here we discuss the domain of validity of our results.

Let us first consider the case where our compact scalar solitons are made of axionic dark matter. In this case, the potential $V(\phi) = m^2 f^2[1 - \cos\phi/f] = m^2\phi^2/2 - \lambda\phi^4/4! + \ldots$, where $\lambda = m^2/f^2$. By comparing the self-interaction and the gravitational interaction, the gravitational interaction dominates our solitons for $\phi/f \lesssim \mathcal{C}^{1/2}$ (where the dimensionless compactness $\mathcal{C} = GM/R$ is of the order of the typical gravitational potential associated with each soliton).[5] For our merger simulations, the maximum value of the field is typically $\phi_{\max} \lesssim 0.24 M_{\text{Pl}}$ (estimated as twice the maximum field value at the center of individual oscillatons). Hence, for $f \gtrsim M_{\text{Pl}}$, we expect our results will remain unchanged.

Although it is not impossible to envision a mechanism through which such a large value of the decay constant would be set in the effective theory [291, 292], $f \gtrsim M_{\text{Pl}}$ is phenomenologically problematic if ϕ constitutes the totality of dark matter. Assuming we have a scenario similar to [192], for $f \gtrsim M_{\text{Pl}}$, the total dark matter abundance bound requires the axion to be unacceptably light ($m < 10^{-30}$ eV), in conflict with observations [201]. An obvious way around this abundance bound is to assume that the field ϕ corresponds to a sub-dominant dark matter component. Conservatively, the results of our paper are therefore expected to apply for solitons made of a subdominant axionic dark matter component with $f \gtrsim M_{\text{Pl}}$.

---

[4] Using fixed grids, we have demonstrated 4th order convergence of the code consistent with methods used [134, 17].

[5] For non-axionic cases with an attractive self-interaction: $\phi \lesssim (m/\sqrt{\lambda})\mathcal{C}^{1/2}$.

As we have discussed, the upper bound of $f \lesssim M_{\rm Pl}$ is desirable from both a model building perspective and from abundance constraints. In the regime $f \ll M_{\rm Pl}$, we would expect self-interactions to be relevant.

However, for $f \lesssim 10^{-2} M_{\rm Pl}$, the self-gravitating real-scalar lumps cannot reach compactness values that would make them approximate mimickers of BHs [17]. Hence, including self-interactions, a typical f value of interest for gravitational wave emission would be $f \sim 10^{-1} m_{\rm Pl}$. For this value of f, we have found that the compactness of our configuration of mass M can change by *at most* 20% relative to the non-interacting case. How does this affect our results? While the compactness for a given mass changes, *if* the fractional gravitational wave output is a function of compactness only, our curve in Fig. 1 should remain unchanged.

These heuristic arguments deserve a more complete study, which will be taken up in future works. The main difficulty lies in setting up initial conditions. The construction of an unexcited ultra-compact initial configuration with significant self-interactions within full nonlinear GR is still an open problem [17].

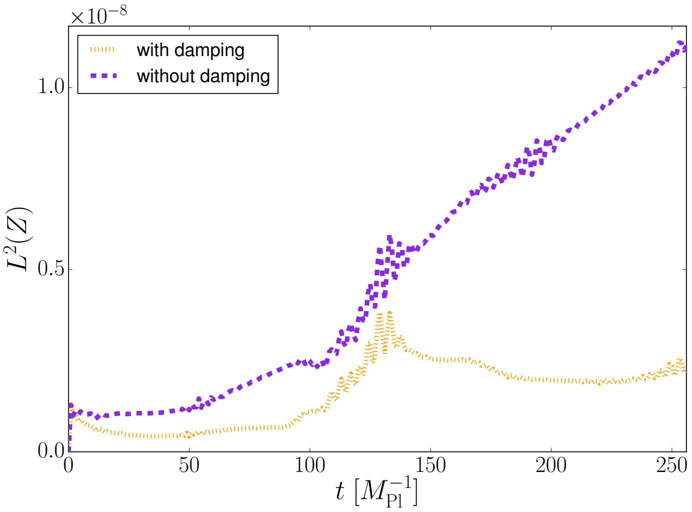

Fig. D.1 **Gauss constraint for static string:** We run the same simulation for am infinite static string with $G\mu = 1.6\times 10^{-2}$ ($\eta = 0.05M_{\rm Pl}$) with and without damping. We find that the damping stabilises the linear growth in violation.

Appendix D

Cosmic String Loop Collapse in Full General Relativity

D.1 Numerical Methodology

D.1.1 Evolution Equations

In this work, we use GRCHOMBO, a multipurpose numerical relavity code [134] which solves the BSSN [135, 280, 136] formulation of the Einstein equation. Meanwhile, the matter part of the Lagrangian is

$$\mathcal{L}_m = -(D_\mu \phi)^*(D^\mu \phi) - \frac{1}{4} F_{\mu\nu} F^{\mu\nu} - V(\phi) \ , \tag{D.1}$$

which gives the evolution equations

$$-D_\mu D^\mu \phi + \frac{\partial V(\phi)}{\partial \bar{\phi}} = 0 \ , \tag{D.2}$$

$$\nabla_\mu F^{\mu\nu} = -eJ^\nu \ , \tag{D.3}$$

with

$$J^\nu = 2Im(\phi^* D^\nu \phi) \ , \ F_{\mu\nu} = \partial_\mu A_\nu - \partial_\nu A_\mu \ . \tag{D.4}$$

We decompose these equations in 3+1 coordinates, following [293]. Furthermore, we impose the Lorenz condition

$$\nabla^\mu A_\mu = 0 \ . \tag{D.5}$$

Using the projector

$$P^\nu_\mu = \delta^\nu_\mu + n_\mu n^\nu \ , \tag{D.6}$$

where n^μ is the normal to the hypersurface, the gauge field and current can further be decomposed into traverse and longitudinal components via

$$\begin{aligned} A_\mu &= \mathcal{A}_\mu + n_\mu \mathcal{A} \ , \\ J_\mu &= \mathcal{J}_\mu + n_\mu \mathcal{J} \ , \end{aligned} \tag{D.7}$$

such that

$$\begin{aligned} \mathcal{A}_\mu &= P^\nu_\mu A_\nu \quad \text{and} \quad \mathcal{A} = -n^\nu A_\nu \ , \\ \mathcal{J}_\mu &= P^\nu_\mu J_\nu \quad \text{and} \quad \mathcal{J} = -n^\nu J_\nu \ . \end{aligned} \tag{D.8}$$

The electric and magnetic fields are defined as

$$E_\mu = P^\nu_\mu n^\rho F_{\nu\rho} \ , \tag{D.9}$$

$$B_\mu = P^\nu_\mu n^\rho (\star F_{\nu\rho}) \ , \tag{D.10}$$

where $(\star F_{\nu\rho})$ is the dual Maxwell tensor. Using the previous decomposition we rewrite the Maxwell tensor as

$$F_{\mu\nu} = n_\mu E_\nu - n_\nu E_\mu + \partial_\mu \mathcal{A}_\nu - \partial_\mu \mathcal{A}_\nu \ . \tag{D.11}$$

In addition, eq. D.3 gives the Gauss constraint

$$\tilde{\nabla}_i E^i = e\mathcal{J} \ , \tag{D.12}$$

where $\tilde{\nabla} = P^\nu_\mu \nabla_\nu$.

To ensure that numerical violation of D.12 is kept to a minimum, we stabilise it by introducing an auxiliary damping variable Z [293–295], resulting in the following modified evolution equations

$$\begin{aligned}
\partial_t E^i &= \alpha(E_i - e\mathcal{J}^i + \tilde{\nabla}_i \mathcal{A}) - \mathcal{A}\tilde{\nabla}_i \alpha + \beta^j \partial_j E^i - E^j \partial_j \beta^i \ , \\
\partial_t \mathcal{A} &= -\mathcal{A}^i \tilde{\nabla}_i \alpha + \alpha(K\mathcal{A} - \tilde{\nabla}_i \mathcal{A}^i - Z) + \beta^j \partial_j \mathcal{A} \ , \\
\partial_t \mathcal{A}_i &= -\alpha(E_i + \tilde{\nabla}_i \mathcal{A}) - \mathcal{A}\tilde{\nabla}_i \alpha + \beta^j \partial_j \mathcal{A}_i + \partial_i \beta^j \mathcal{A}_j \ , \\
\partial_t Z &= \alpha(\tilde{\nabla}_i E^i - e\mathcal{J} - \kappa Z) + \beta^j \partial_j Z \ .
\end{aligned} \tag{D.13}$$

From fig. D.1 we see the scheme is effective at stopping the growth of constraint violations.

Finally, we decompose the complex scalar field

$$\phi = \frac{1}{\sqrt{2}}(\phi_1 + i\phi_2) \ , \tag{D.14}$$

and rewriting the matter equation with BSSN variables,

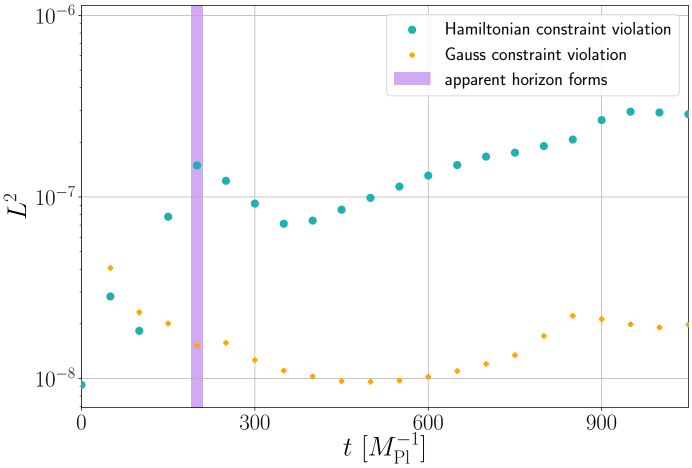

Fig. D.2 L^2 **norm of constraints:** Loop with $G\mu = 1.6\times 10^{-2}$ and $R = 100\ M_{\rm Pl}^{-1}$ remains stable throughout evolution, even after Black hole formation. The initial Hamiltonian constraint is smaller than it can be maintained by the evolution scheme. The momentum constraints violation are negligible throughout.

$$\begin{aligned}
\partial_t\phi_a &= \alpha\Pi_{M,a} + \beta^i\partial_i\phi_a\ , \\
\partial_t\Pi_{M,a} &= \beta^i\partial_i\Pi_{M,a} + \alpha\partial_i\partial^i\phi_a + \partial_i\phi_a\partial^i\alpha \\
&\quad + \alpha\left(K\Pi_{M,a} - \gamma^{ij}\Gamma^k_{ij}\partial_k\phi_a + \frac{dV}{d\phi_a}\right) \\
&\quad + \alpha(-e^2A_\mu A^\mu\phi_a \pm e\phi_{a+1}\nabla_\mu A^\mu \\
&\quad \pm 2eA^\mu\partial_\mu\phi_{a+1})\ , \\
\partial_t E^i &= \alpha K E^i + e\alpha\chi\tilde\gamma^{ij}\mathcal{J}_j + \alpha\chi\tilde\gamma^{ij}\partial_j Z \\
&\quad + \chi^2\tilde\gamma^{ij}\tilde\gamma^{kl}\partial_l\alpha(\partial_j\mathcal{A}_k - \partial_k\mathcal{A}_j) \\
&\quad + \chi^2\tilde\gamma^{ij}\tilde\gamma^{kl}(\tilde D_k\partial_j\mathcal{A}_l - \tilde D_k\partial_l\mathcal{A}_j) \\
&\quad + \frac{\alpha}{2}\chi\tilde\gamma^{ij}\tilde\gamma^{kl}(\partial_j\mathcal{A}_l\partial_k\chi - \partial_k\mathcal{A}_j\partial_l\chi) \\
&\quad + \beta^j\partial_j E^i - E^j\partial_j\beta^i - \alpha e\mathcal{J}^i\ , \\
\partial_t\mathcal{A} &= \alpha K\mathcal{A} - \alpha\chi\tilde\gamma^{ij}\partial_j\mathcal{A}_i + \alpha\chi\mathcal{A}_i\tilde\Gamma^i - \alpha Z \\
&\quad + \frac{\alpha}{2}\mathcal{A}_i\tilde\gamma^{ij}\partial_j\chi - \chi\tilde\gamma^{ij}\mathcal{A}_i\partial_j\alpha + \beta^j\partial_j\mathcal{A}\ , \\
\partial_t\mathcal{A}_i &= -\alpha\chi^{-1}\tilde\gamma_{ij}E^j - \alpha\partial_i\mathcal{A} - \mathcal{A}\partial_i\alpha \\
&\quad + \beta^j\partial_j\mathcal{A}_i + \partial_i\beta^j\mathcal{A}_j\ , \\
\partial_t Z &= \alpha\tilde\nabla_i E^i - \frac{3}{2}\frac{\alpha}{\chi}E^i\partial_i\chi - \alpha e\mathcal{J} - \alpha\kappa Z + \beta^j\partial_j Z\ ,
\end{aligned} \tag{D.15}$$

where $a \in \{1,2\}$ and the second order Klein Gordon equation has been decomposed into two first order equations as usual. The stress energy tensor for Abelian Higgs is

$$T_{\mu\nu} = D_{(\mu}\phi^{*}D_{\nu)}\phi + F_{\mu\alpha}F^{\alpha}_{\nu} + g_{\mu\nu}\mathcal{L}_{m}, \tag{D.16}$$

and its various components are defined as

$$\begin{aligned} &\rho = n_a n_b T^{ab} , \quad S_i = -\gamma_{ia} n_b T^{ab} , \\ &S_{ij} = \gamma_{ia}\gamma_{jb} T^{ab} , \quad S = \gamma^{ij} S_{ij} . \end{aligned} \tag{D.17}$$

The Hamiltonian constraint

$$\mathcal{H} = R + K^2 - K_{ij}K^{ij} - 16\pi\rho \ , \tag{D.18}$$

the momentum constraint

$$\mathcal{M}_i = D^j(\gamma_{ij}K - K_{ij}) - 8\pi S_i \ , \tag{D.19}$$

and the Gauss constraint

$$\mathcal{Z} = \tilde{\nabla}_i E^i + e\mathcal{J}^{\nu} n_{\nu} \ , \tag{D.20}$$

are monitored throughout the evolution to check the quality of our simulations (see fig. D.2). Our boundary conditions are Dirichlet.

D.1.2 Initial Data

We set up the field as mentioned in the main text using toroidal coordinates (see fig. D.4). Time symmetry is assumed for our initial data,

$$K = 0 \ , \qquad A_{ij} = 0 \ , \tag{D.21}$$

which automatically fulfils the momentum contraint (eq. D.19). In addition, we make a conformally flat[1] ansatz $\tilde{\gamma}_{ij}$,

$$\tilde{\gamma}_{ij} = \delta_{ij} \ , \tag{D.22}$$

---

[1] This is not the unique solution to the constraint equations given the initial field configuration. However, it is the most easily implemented, as more general initial conditions require much greater computational resources to find. Conformal flatness is also consistent with the fact that the spacetime is asymptotically Schwarzschild.

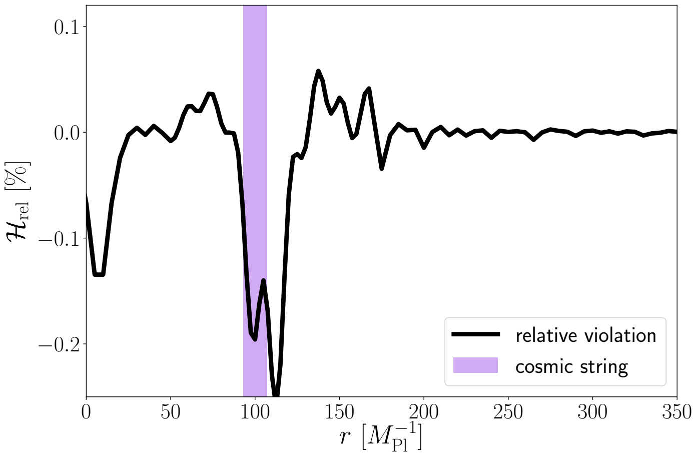

Fig. D.3 **Initial relative violation**: Slice through initial data for loop from center through string with $G\mu = 1.6 \times 10^{-2}$ and initial radius $R = 100\ M_{\rm Pl}^{-1}$. The shaded region indicates where the string is located. We find that there is an error of at most 0.3%.

and impose the metric to be equal to the identity δ_{ij} in the center of the string, similar as the static string (see eq. D.30). We find that doing so reduces possible excitations of the string. For the gravitational wave extraction, we impose the condition

$$\lim_{r\to\infty} \chi = 1 \ , \tag{D.23}$$

by applying a rescaling of the radial coordinates.

We solve for χ using the Hamiltonian constraint eq. D.18. We reduce the spatial dimension of the problem by using its cylindrical symmetry. This solution is then further relaxed to obtain the final solution, which is that of an excited cosmic string loop.

As shown in fig. D.3, the relative Hamiltonian violation from our prescription is

$$\mathcal{H}_{\rm rel} = \frac{\mathcal{H}}{16\pi\rho_{\rm max}} < 1\% \ .$$

D.1.3 Numerical Extraction of Signal

We extract the Penrose scalar Ψ_4 with tetrads proposed by [296]. Similarly as in Black hole binaries, there is some non-physical radiation associated with the initial data, which in our case consists of a toroidal shell of artificial radiation resulting in two GW peaks before the physical signal. While such stray-GW can often be ignored as they quickly radiate away at

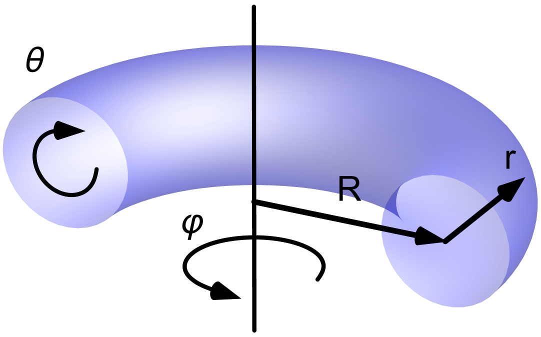

Fig. D.4 **Toroidal coordinates** encode the symmetry of our cosmic string loops. They are used to generate the initial field configuration, where R defines the radius of the loop.

light speed, in our case due to the rapid collapse of our loops at ultrarelativistic speeds, they cannot be ignored.

The first peak at $t_{\mathrm{ret}} < 0$ is due to this initial radiation travelling opposite to the collapse and could be separated by increasing the loop radius so that the real signal takes longer. However, the second peak (first peak in fig. 5.1) results from the radiation which travels together with the collapsing loop at similar velocity, which always mixes with the real signal. In any case, increasing the loop radius would result in a cleaner signal but this is computationally very expensive.

To estimate the GW energy we use the equation

$$\frac{dE_{\mathrm{GW}}}{dt} = \frac{r^2}{16\pi} \int_{\mathcal{S}_r} \left| \int_{t_0}^{t} \Psi_4 dt' \right|^2 d\Omega \,, \tag{D.24}$$

where $\mathcal{S}_r$ is a sphere of radius r.

In the cases for which the cosmic string loop does not form a Black hole, most of the matter will escape, typically at velocities close to the speed of light. This scalar and vector radiation overlaps the gravitational wave signal and due to its large mass might leave an imprint on $r\Psi_4$, making the signal extraction problematic[2].

---

[2] This could be prevented by setting the extraction zone further out, but this is numerically too expensive.

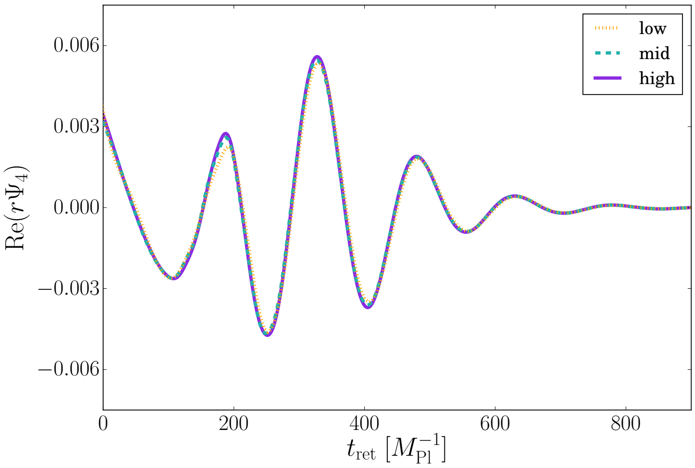

Fig. D.5 **Convergence in** $r\Psi_4$ between low, mid and high resolutions giving an overall 2nd-3rd order convergence. The x-axis $t_{\rm ret} = t - r_{\rm ext}$ is the retarded time where $r_{\rm ext}$ is the extraction radius.

D.1.4 Numerics and Convergence Tests

In fig. D.2, we show that the volume-averaged Hamiltonian constraint violation

$$L^2(H) = \sqrt{\frac{1}{V}\int_V |\mathcal{H}^2| dV} \ , \tag{D.25}$$

where V is the box volume with the interior of the apparent horizon excised, is under control throughout the simulation.

We use the gradient conditions on ϕ and χ to tag cells for regridding. The precise criteria is chosen depending on the symmetry breaking scale η and the total mass of the system. The major distinction for the amount of resolution needed is whether GW are being extracted or not. To obtain a clean GW large boxes are needed to avoid the detection of reflections of the non-physical signal with the boundaries, which increases the cost of the simulation. We double checked that our signal in fig. 5.1 was consistent with a $l = 2$ $m = 0$ QNM [297] within numerical error.

We tested the convergence of our simulations with a cosmic string loop of $\eta = 0.05$ ($G\mu = 1.6 \times 10^{-2}$) and $R = 100\ M_{\rm Pl}^{-1}$ by using a box of size $L = 2048\ M_{\rm Pl}^{-1}$ in which we improved by a factor of 1.5 between all three resolutions. The convergence of $r\Psi_4$ for low ($\Delta x_{\rm min} = 1.33\ M_{\rm Pl}^{-1}$), medium ($\Delta x_{\rm min} = 1.00\ M_{\rm Pl}^{-1}$) and high ($\Delta x_{\rm min} = 0.66\ M_{\rm Pl}^{-1}$) resolutions is shown in fig. D.5.

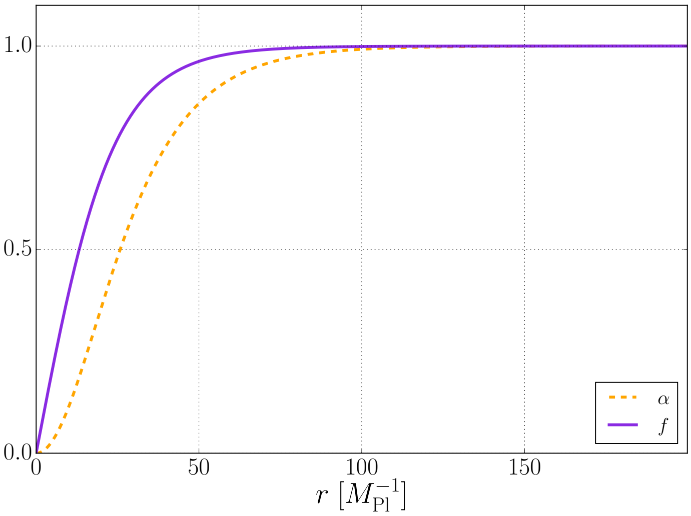

Fig. D.6 **Radial profile of α and f** for an infinite static string with gravity in the critical coupling limit ($e=1,\ \lambda=2$) and $\eta=0.05\ M_{\rm Pl}$ ($G\mu=1.6\times10^{-2}$).

D.2 Abelian Higgs Code Test

To test the code, we compare the evolution of a simulation with a known semi-analytic case of the infinite static string [247]. Given the symmetry of the problem we use polar coordinates

$$\begin{aligned} x &= r\cos(\theta)\ , \\ y &= r\sin(\theta)\ , \\ z &= z\ . \end{aligned} \tag{D.26}$$

and choose cylindrically symmetric ansatz for the scalar and gauge fields ϕ and A_μ

$$\begin{aligned} \phi &= f(r)e^{in\theta}\ , \\ A_\theta &= \frac{n\alpha(r)}{e}\ , \end{aligned} \tag{D.27}$$

and all other components are set to zero. We impose the boundary conditions

$$\begin{aligned} f(0) &= 0\ , \qquad & f(\infty) &= 1\ , \\ \alpha(0) &= 0\ , \qquad & \alpha(\infty) &= 1\ . \end{aligned} \tag{D.28}$$

For the metric, the following ansatz is chosen

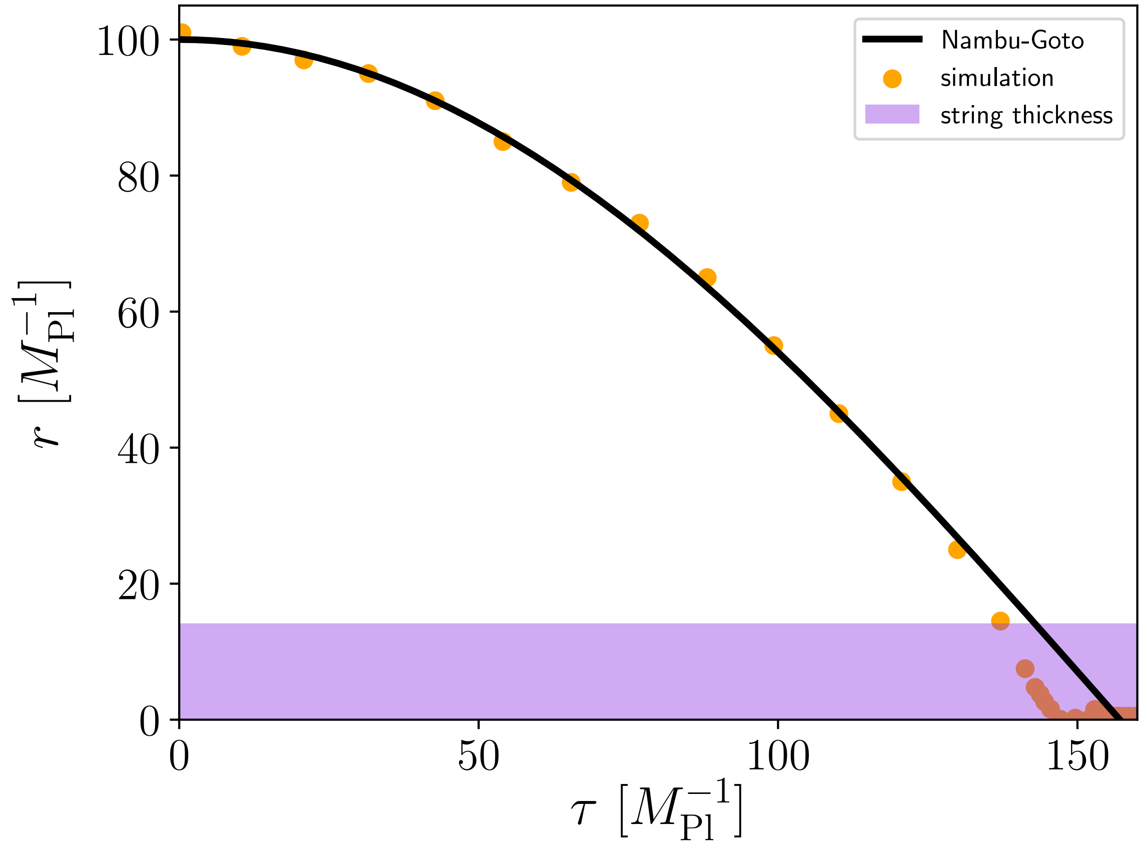

Fig. D.7 **Comparison with Nambu-Goto** for loop with $G\mu = 1.6 \times 10^{-2}$ and initial radius $R = 100\ M_{\rm Pl}^{-1}$ shows agreement.

$$ds^2 = -e^{A(r)}dt^2 + e^{B(r)}(dr^2 + r^2 d\theta^2) + e^{A(r)}dz^2 \ , \tag{D.29}$$

where $A(r)$ and $B(r)$ are radial functions numerically determined. We impose the metric and its derivatives to be locally flat

$$\begin{aligned} A(0) &= 0\ , \qquad & A'(0) &= 0\ , \\ B(0) &= 0\ , \qquad & B'(0) &= 0\ . \end{aligned} \tag{D.30}$$

We solve Einstein's and the corresponding matter evolution equations

$$G_{\mu\nu} = 8\pi T_{\mu\nu}\ , \tag{D.31}$$

$$D_\mu D^\mu \phi = \frac{dV}{d\bar{\phi}}\ , \tag{D.32}$$

iteratively as follows. We solve the Klein-Gordon equation (eq. D.32) for fixed flat background, then use this solution to calculate the stress-energy tensor and retrieve the values of $A(r)$ and $B(r)$ via (D.31) to build a new metric. Plugging this back into the Klein-Gordon equation we find new profiles for the fields using the new metric as background. The solution converges quickly (within ~ 5 iterations), see fig. D.6 for the obtained profiles of f and α.

D.3 Comparison with Nambu-Goto

Previous work showed that without gravity [298] the Nambu-Goto (NG) action is still valid at relativistic speeds. However, a comparison between the two approaches, leads to consistent results with NG up to roughly the point when the string radius is close to the string thickness (see fig. D.7). To reduce gauge effects we use the time of static observer at the position of the string,

$$\tau = \int \alpha|_{\rho=\max(\rho)}\, dt \; . \tag{D.33}$$

Having shown that NG is a good approximation, we use it to estimate the velocity before unwinding, which we define as the point where the radius of the ring R is equal to the thickness of the string δ. We find

$$v_\delta = \sqrt{1 - \left(\frac{\delta}{R}\right)^2} \; , \tag{D.34}$$

which, for our simulations, gives results ranging from 0.97 c to 0.99 c. In the case for which we extract the gravitational wave signal ($G\mu = 1.6 \times 10^{-2}$, $R = 100\ M_{\rm Pl}^{-1}$) we estimate a velocity of 0.99 c before collision.